FACULDADE DE ENGENHARIA DA UNIVERSIDADE DO PORTO





Implementation of a Shared Control Strategy for Myoeletrically Controlled Transradial Prostheses

Joana Francisca Barros Matos

Mestrado Integrado em Bioengenharia

Supervisors: Prof. Dr. Cristina Piazza
Theophil Spiegeler Castañeda
Dr. Patricia Capsi-Morales
Prof. Dr. António Pedro Aguiar

October 13, 2023

Implementation of a Shared Control Strategy for Myoeletrically Controlled Transradial Prostheses

Joana Francisca Barros Matos

Mestrado Integrado em Bioengenharia

October 13, 2023

Resumo

A mão é uma estrutura altamente complexa e fundamental para a vida humana. Apesar de intensa investigação, as próteses de membro superior continuam longe de atingir o nível de funcionalidade dos membros naturais. Desenvolvimentos no projeto mecânico de mãos artificiais permitiram a criação de mãos complexas e com elevada dexteridade. Contudo, o seu controlo continua limitado pelas condições inerentes aos utilizadores de próteses, tais como o número limitado de sinais de entrada e a ausência de *feedback* sensorial. Para contrariar isto, diversas estratégias de controlo baseado em diferentes modalidades de sensorização têm sido desenvolvidas para complementar o tradicional controlo mioelétrico.

Esta dissertação apresenta uma nova estratégia de controlo em paralelo, inspirada na fisiologia humana. Ao dividir o controlo da preensão entre um controlador de alto nível e um controlador de baixo nível, parte da autonomia é transferida do utilizador para a prótese, resultando numa interação mais simples. Deste modo, o utilizador é responsável por iniciar a preensão do objeto enquanto o controlador de baixo nível em malha fechada assegura a estabilidade durante a manipulação. Isto foi alcançado através da incorporação de sensores de força 3D distribuídos por toda a mão, e através dos quais é possível detetar o escorregamento do objeto.

Este controlador foi experimentalmente comparado com as abordagens de estado da arte. Os resultados indicam que a estratégia aqui proposta é capaz de evitar escorregamento dos objetos, aplicando uma menor força de preensão. Experiências adicionais foram realizadas para comparar a resposta do controlador à resposta fisiológica.

Abstract

The hand is a highly complex structure instrumental to human life. Despite being an intensely researched topic, upper-limb prostheses still struggle to come close to the natural limb's functionality. Advances in the mechanical design of artificial hands have enabled the creation of complex and dexterous hands. However, their control remains restrained by the limitations inherent to prosthesis users, such as a restricted number of control inputs and a lack of sensory feedback. Numerous shared control strategies have been proposed in research to counteract this, employing different sensing modalities to complement traditional myoelectric control.

This dissertation presents a novel shared control strategy based on the physiology of human grasping. By dividing the control of the grasp into a high and a low-level controller, part of the autonomy is transferred from the user to the prostheses, allowing for a more effortless interaction. The user is responsible for initially grasping the object, while a low-level closed-loop controller ensures stability throughout the task. This is achieved by including 3D force sensors throughout the hand, through which slip is detected.

Experiments were carried out to compare the novel controller with common state-of-the-art approaches. Results indicate that this approach successfully avoids slippage while resulting in a smaller grasping force. Further experiments were performed to compare its response with the human response.

Acknowledgement

I am incredibly grateful for the opportunity Prof. Cristina Piazza and Patri gave me by welcoming me into their group and trusting me with constant opportunities to grow. Truly, when I said yes to the internship, I could never have envisioned how much I would learn in one year. I can't thank Theo enough for all the hours I stole from him. The guidance, both in and out of the lab, is deeply appreciated. Finally, I need to thank Prof. António Pedro Aguiar for his support in the final stages of the work.

I'm grateful to everyone who passed by the lab during the year for all the aimless conversations and personal and professional problem-solving sessions. However, I need to give a special thank you to Thomas for helping me get started in Munich and to Ali, Mohamad and Johanna for their constant companionship - a special shoutout to Oscar for all the help in the final stages of the thesis. Finally, Julia's energy and unwavering presence were instrumental to my life in Munich.

To all my friends from home, thank you for the unending empathy, listening to me ramble and keeping me somewhat sane. A special thank you to Baltazar for going on this journey with me from beginning to end. I am sorry for all the times I stole your clothes.

Finally, I need to thank my family. To my parents for giving me the support needed to embark on this journey. To my siblings for always being there, but above all, for continuing to be children with me. To Becas, Chica, Telmo and Óscar for helping me through everything.

Joana Matos

Contents

1 Introduction **1**
- 1.1 Motivation . . . 1
- 1.2 Goals . . . 2
- 1.3 Outline . . . 2
- 1.4 Publications . . . 3

2 Background and Theory **5**
- 2.1 Upper Limb Anatomy and Amputation . . . 5
- 2.2 Commercial Upper Limb Prostheses . . . 7
- 2.3 Electromyography . . . 8
- 2.4 Soft Robotics . . . 9
- 2.5 Human Tactile Feedback . . . 11
- 2.6 Friction Cone . . . 15
- 2.7 Digital Filtering . . . 16
- 2.8 Closed-loop Control . . . 19

3 State of the Art **23**
- 3.1 Myoelectric Control . . . 23
- 3.2 Shared Control Strategies . . . 25
  - 3.2.1 Tactile Slip Control . . . 25
  - 3.2.2 Vibration Detection . . . 27
  - 3.2.3 Friction Cone . . . 28
  - 3.2.4 Machine Learning . . . 29
  - 3.2.5 Method Comparison . . . 29

4 Methodology **31**
- 4.1 Materials . . . 31
  - 4.1.1 Force Sensors . . . 31
  - 4.1.2 Robotic Hand . . . 35
  - 4.1.3 Robotic Arm . . . 37
  - 4.1.4 Electromyography Armband . . . 37
  - 4.1.5 Inertial Measurement Unit . . . 37
  - 4.1.6 Interfacing Overview . . . 38
- 4.2 Combined Shared Control . . . 40
  - 4.2.1 Force Module . . . 40
  - 4.2.2 Bandpass Filtering . . . 41
  - 4.2.3 Friction Cone . . . 44
- 4.3 Protocol . . . 45

4.3.1 Controller Validation 45
4.3.2 Slip Detection 47
4.3.3 Human Comparison 48

5 Results **51**
5.1 Slip Detection 51
5.2 Controller Response 53
5.3 Human Response 66

6 Discussion **67**
6.1 Slip Detection 67
6.2 Controller Comparison 69
6.3 Comparison with Human Grasping 70

7 Conclusion **73**
7.1 Future Work 74

References **75**

List of Figures

1.1 Components of a Transradial Prosthesis . . . 1
1.2 Closed-loop Architecture for a Prosthesis. . . . 2

2.1 Levels of Amputation . . . 5
2.2 Bones of the Human Hand and Wrist . . . 6
2.3 Terminology of Hand Movements. . . . 7
2.4 Types of Upper Limb Prostheses . . . 8
2.5 Action Potential . . . 9
2.6 EMG Acquisition System . . . 10
2.7 Robotic Joint Types . . . 11
2.8 Haptic Sensing of Object Properties . . . 12
2.9 Types of Sensory Endings in the Hand . . . 13
2.10 Tactile Afferents' Response to the Different Phases of Grasping . . . 14
2.11 Friction Angle and Friction Cone . . . 15
2.12 Bode Plot of Euler and Bilinear Discretisation . . . 18
2.13 Block Diagram of a Closed Loop Controller . . . 19

3.1 Myoelectric Control Types . . . 24
3.2 Hierarchical Shared Control Strategy . . . 26
3.3 Center of Pressure Force Control . . . 27
3.4 FFT of Slip Events. . . . 28
3.5 BioTac Biomimetic Sensor . . . 29

4.1 Hall Effect . . . 31
4.2 Force Sensors . . . 32
4.3 Force Sensor Calibration Data . . . 33
4.4 Force Module Schematics . . . 34
4.5 Placement of the Force Sensors . . . 35
4.6 QB SoftHand . . . 36
4.7 SoftHand Joints and Tendon . . . 36
4.8 Myo Armband . . . 37
4.9 Overview of the System Interfacing . . . 38
4.10 Controller Workflow . . . 39
4.11 Frequency Response of the Analog and Digital Filters . . . 42
4.12 Objects Used in the Validation . . . 45
4.13 Validation Setup . . . 46
4.14 Experimental End-Effector Trajectory . . . 47
4.15 Human Comparison Protocol. . . . 48

5.1 Bandpass Filtering Example 52
5.2 No Control Response Example 54
5.3 Bandpass Control Response Example 55
5.4 Friction Cone Control Response Example 57
5.5 Combined Control Response Example 58
5.6 Force and Acceleration for the Controllers 59
5.7 Force and Acceleration for each Object 60
5.8 Force and Acceleration for the Controllers for each Object 61
5.9 Force and Acceleration for the Controllers for the Small Cylinder 62
5.10 Force and Acceleration for each Closure 63
5.11 Force and Acceleration for the Controllers for each Closure 64
5.12 Shear Force for the Lifting Task for each Controller 65

6.1 Contact Between the Objects and the Sensors 68
6.2 Shear Force in Human Grasping 70

List of Tables

4.1 Validation Object's Properties 46

5.1 Accuracy, Precision, Recall and F1 score of the Slip Detection. 53
5.2 Force and Acceleration for the Controllers 55
5.3 Friedman Test Results 56
5.4 Wilcoxon Pairwise Comparison 56

Abbreviations

ADC	Analog-to-Digital Converter	**IC**	Integrated Circuit
ANOVA	Analysis of Variance	**IDE**	Integrated Development Environment
BLE	Bluetooth Low Energy	**IMU**	Inertial Measurement Unit
BP	Bandpass Controller	**IP**	Interphalangeal
CC	Combined Controller	**LTI**	Linear Time-Invariant
CMC	Carpometacarpal	**MCP**	Metacarpophalangeal
CoP	Center of Pressure	**MUAP**	Motor Unit Action Potential
CPU	Central Processing Unit	**NC**	No Controller
DoA	Degree of Actuation	**PCB**	Printed Circuit Board
DoF	Degree of Freedom	**PD**	Proportional-Derivative
EMG	Electromyography	**PI**	Proportional-Integral
$\mathbf{F_N}$	Normal Force	**PID**	Proportional-Integral-Derivative
$\mathbf{F_S}$	Shear Force	**PLA**	Polylactic Acid
FA-I	Fast Adapting type I afferent	**Q**	Quality factor
FA-II	Fast Adapting type II afferent	**RFS**	Resistive Flex Sensors
FC	Friction Cone Controller	**SA-I**	Slowly Adapting type I afferent
FCI	Franka Control Interface	**SA-II**	Slowly Adapting type II afferent
FDM	Fused Deposition Modeling	**SAMS**	Southampton Adaptive Manipulation Scheme
FFT	Fast Fourier Transform	**sEMG**	Surface EMG
FN	False Negative	**SNR**	Signal-to-Noise Ratio
FP	False Positive	**SP**	Set Point
FSM	Finite State Machine	**TN**	True Negative
FSR	Force Sensitive Resistor	**TP**	True Positive
GPIO	General Purpose Input/Output	**UDP**	User Datagram Protocol
HP	Horsepower	μ**C**	Microcontroller
I2C	Inter-Integrated Circuit	μ_s	Static friction coefficient

Chapter 1

Introduction

1.1 Motivation

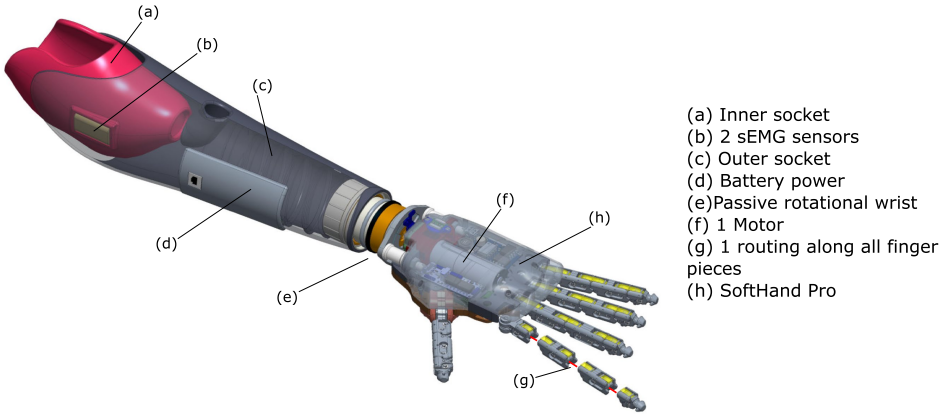


Figure 1.1: Components of a myoelectric transradial prosthesis (SoftHand Pro). Taken from [1].

Upper limb amputation is a life-altering event that happens yearly to over twenty thousand people in the USA and EU [3]. Due to the amputation, patients often lose autonomy due to the increased difficulty performing social, work, and daily tasks. Upper limb prostheses are currently used to try to overcome these limitations. However, even the most advanced ones are still severely lacking in functionality when compared to biological hands [4].

While the technological development of the last few decades allows prostheses to have some of the dexterity associated with the human hand, the most limiting factor stems from the human-prosthesis interface. On one side, commercial prostheses are typically controlled by one or two electromyography (EMG) electrodes positioned on the surface of the forearm, as shown in Figure 1.1. This restricted number of inputs means that unintuitive and complex control methods, such as muscle co-contraction and contraction speed, must be explored in order to use the multiple available grasping patterns [5]. Additionally, current EMG systems are associated with a long list of limitations that impact the easiness of controlling numerous degrees-of-freedom (DoFs).

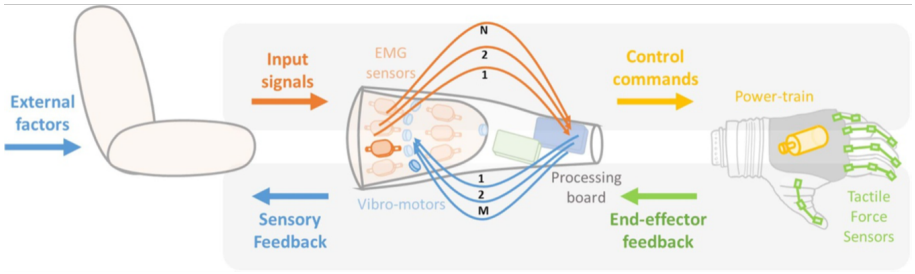


Figure 1.2: Closed-loop architecture for a prosthesis. Taken from [2].

One of the main difficulties in restoring functionality in amputees is associated with the interruption of the biological pathways responsible for the closed loop between motor control and sensory feedback. This could be achieved through an architecture similar to the one presented in Figure 1.2 where tactile information is used in a closed-loop controller and also given to the user as vibrational feedback. While some recent commercial prostheses, for example, the VINCENTevolution4 hand (Vincent Systems, Germany), can now provide tactile feedback, this is still an uncommon feature that prostheses' users frequently report as desired [4]. To overcome the lack of feedback, users often have to rely on visual and auditory feedback to estimate gripping force [6].

Taking all these aspects into consideration, it is apparent that conventional EMG control is not enough for current prosthesis users. Due to this fact, different strategies need to be developed to further approximate the control of existing devices to their mechanical capability and eventually to biological human hands.

One of the ways this can be achieved is by implementing shared control strategies. By employing multiple sensing modalities, part of the control can be automated, reducing the burden on the amputee. To achieve this, biomimetic low-level controllers could be implemented to resemble human reflexes, resulting in intuitive strategies.

1.2 Goals

The main goal of this dissertation is addressing some of the current limitations of upper limb prostheses, with a focus on grasp stability. In line with research trends, this should be implemented based on bio-inspired control strategies. The solution should involve the exploration of tactile information to autonomously ensure grasp stability while keeping the authority at user level. The approach should have properties similar to the physiological ones, with special emphasis on reaction time and intuitiveness.

1.3 Outline

Besides the introduction, this dissertation is composed of six other chapters. In Chapter 2, the theoretical foundations required for understanding this work and related concepts are introduced. Chapter 3 presents a literature review of the state of the art related to the control of myoelectric

upper-limb prostheses, focusing on tactile shared control. Chapter 4 gives a detailed description of the experimental setup and protocol. In Chapters 5 and 6, the obtained results are, respectively, presented and interpreted. Finally, Chapter 7 gives a recapitulation of the work developed and briefly discusses future improvements.

1.4 Publications

- T. S. Castañeda, **J. Matos**, P. Capsi-Morales, and C. Piazza. Spatial and Temporal Analysis of Normal and Shear Forces during Grasping, Manipulation and Social Activities. In 2023 IEEE International Conference on Rehabilitation Robotics, 2023.
- Based on this dissertation, a manuscript is being prepared for submission to IEEE EMB's 10th International Conference on Biomedical Robotics and Biomechatronics (BioRob 2024).

Chapter 2

Background and Theory

This chapter introduces the most relevant notions for the understanding of the dissertation. It starts by elaborating on some of the main concepts concerning upper limb prostheses, presents the current fundamental knowledge surrounding tactile feedback, and introduces some of the mathematical concepts that were applied during the development of the work.

2.1 Upper Limb Anatomy and Amputation

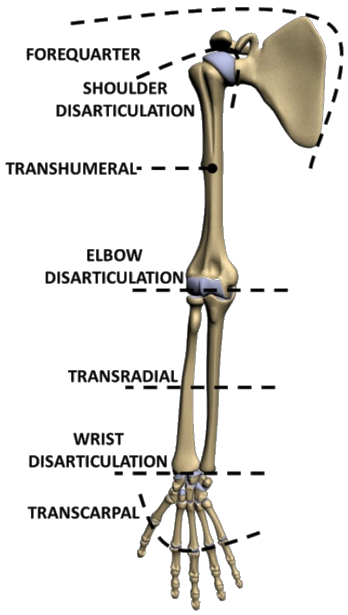


Figure 2.1: Levels of upper limb amputation. Taken from [4].

Congenital or surgical amputation is the loss of a limb, respectively, due to malformation in the womb or due to medical necessity caused by trauma or malignancy. It can occur at different levels, as can be visualised in Figure 2.1, from the most distal at the fingertip to the most proximal, including the shoulder [8]. While the most common type of amputation, transcarpal, happens at

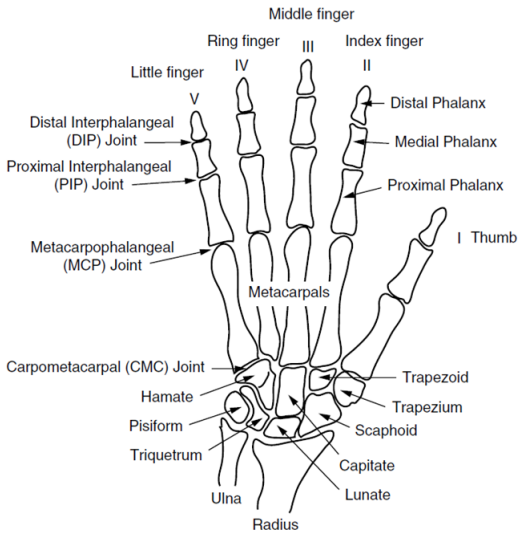


Figure 2.2: Bones of the human hand and wrist. Taken from [7].

the hand level, it is followed in incidence level by transhumeral and transradial amputation. These types of amputation lead to a substantial loss of motor control and sensory feedback, primarily due to the loss of the hand, a complex tool used for manipulating and exploring the environment and social interaction [9].

The high functionality of the human hand stems from its complex control and mechanical design, as shown in Figure 2.2. It can be used for both precision and power tasks due to its high number of DoFs in the hand and wrist [4]. These DoFs correspond to flexion/extension of all interphalangeal (IP) and metacarpophalangeal (MCP) joints as well as abduction/adduction of the MCP joints. The carpometacarpal (CMC) joint of the ring and little finger is also capable of some flexion/extension that helps the hand adapt to the shape of grasped objects. The wrist is capable of flexion/extension, radial/ulnar deviation and rotation [7]. These movements are exemplified in Figure 2.3.

The movement of the fingers is produced by the extrinsic and intrinsic muscles, which originate predominantly in the forearm and in the hand, respectively. The extrinsic muscles are responsible for powerful movements, while the intrinsic muscles are responsible for precise and coordinated finger movement. The extrinsic muscles can be further divided into extensors, located primarily on the posterior forearm, and flexors, located in the anterior forearm. They can additionally be split into superficial and deep muscle groups, depending on their distance to the surface of the arm. The intrinsic muscles can be divided into three groups. The thenar group actuates the thumb, the hypothenar actuates the little finger, and the midpalmar acts on all fingers with the exception of the thumb [7].

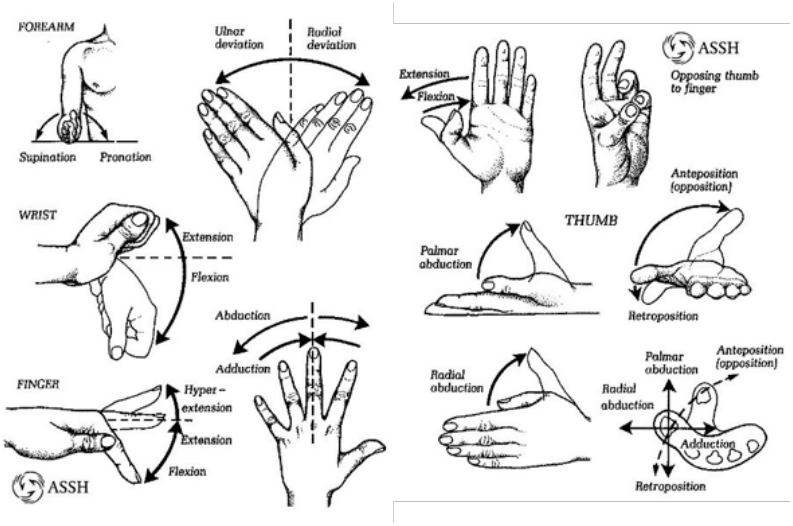


Figure 2.3: Anatomical terminology for hand movements. Taken from [10].

2.2 Commercial Upper Limb Prostheses

Upper limb prostheses are the current solution to mitigate the loss of functionality caused by amputation. Based on their functionality, they can be divided into passive and active prostheses [4].

Passive prostheses are the most basic solution. They can be further divided into cosmetic prostheses, whose only function is to restore aesthetic appearance, and functional prostheses that have a specific functionality in mind and can be used, for example, for work or sport as in Figure 2.4(b) [4].

Active prostheses can be divided into body-powered and externally powered. Body-powered prostheses typically have only one DoF and are controlled through the movement of the upper body. Generally, a harness is worn around the chest or shoulders, whose movement will pull on a cable system that opens or closes the hand. They are robust and inexpensive and naturally have integrated feedback regarding the applied force due to the way they are controlled. However, their functionality is relatively low, and they require large amounts of physical effort [11].

Externally powered prostheses utilise an external power source, usually a battery pack, to power the movement of the hand. They are the most technologically advanced option for amputees and are the current leading research focus [4].

Traditionally, they utilise EMG signals to control the device and thus are also called myoelectric prostheses. The EMG signals are typically acquired by two surface electrodes positioned on antagonistic muscles in the forearm. By contracting the muscles close to the electrodes, the user can control the opening and closing of the hand. Different control strategies have to be implemented in the case of commercial hands with more than one active DoF. These strategies are usually non-intuitive such as co-contraction [11]. A more in-depth review of EMG control will be presented in Chapter 3.1.



(a) (b) (c) (d)

Figure 2.4: Types of upper limb prostheses: (a) Cosmetic (Ottobock, Germany) (b) Functional (Steeper Group, United Kingdom) (c) Body powered (Ottobock, Germany) (d) Myoelectrical (Ottobock, Germany).

2.3 Electromyography

Neurones are cells from the nervous system that, due to an unequal distribution of potassium and sodium ions, have a steady electrical potential of around -60 mV across the plasma membrane. This electrical potential is called the resting potential, as it is present when there is no excitation. Through chemical signals, such as neurotransmitters, or voltage changes, the membrane's conductance to sodium, potassium, calcium, and chloride ions changes, causing a depolarization or hyperpolarization of the membrane. An action potential is a self-propagating reversal of the membrane polarity. It is triggered by an influx of sodium ions that rapidly reverse polarity to +20 mV, which is then followed by an efflux of potassium ions, returning the membrane to a resting potential. This change in polarity travels at a constant speed through the axon, with each segment being triggered by its upstream neighbouring section until it reaches the axonal terminals, as seen in Figure 2.5. Here, the depolarization of the presynaptic membrane causes the release of neurotransmitters that will excite the next neuron or, in the case of motor neurons, the muscle cells [12].

Skeletal muscles are organised structures of muscle fibres enervated by at least one nerve. The combination of repeating protein structures alongside nervous networks comprised of motor and sensory components allows for powerful and precise movement of the human body. The motor components are composed of motor neurons that terminate at a neuromuscular junction. The combination of the motor neuron with the muscle fibres forms a motor unit. The size of a motor unit depends on the muscle it innervates. Large muscles used for powerful movements have more fibres per neuron, allowing for synchronous contraction of fibres within the same muscle. In comparison, muscles involved in tasks requiring precision have fewer fibres per neuron [13].

For a muscle contraction to happen, a motor command produced in the central nervous system is transmitted to the peripheral nervous system, where the excitation of the neuron results in the propagation of an action potential along its axon. This action potential eventually reaches the neu-

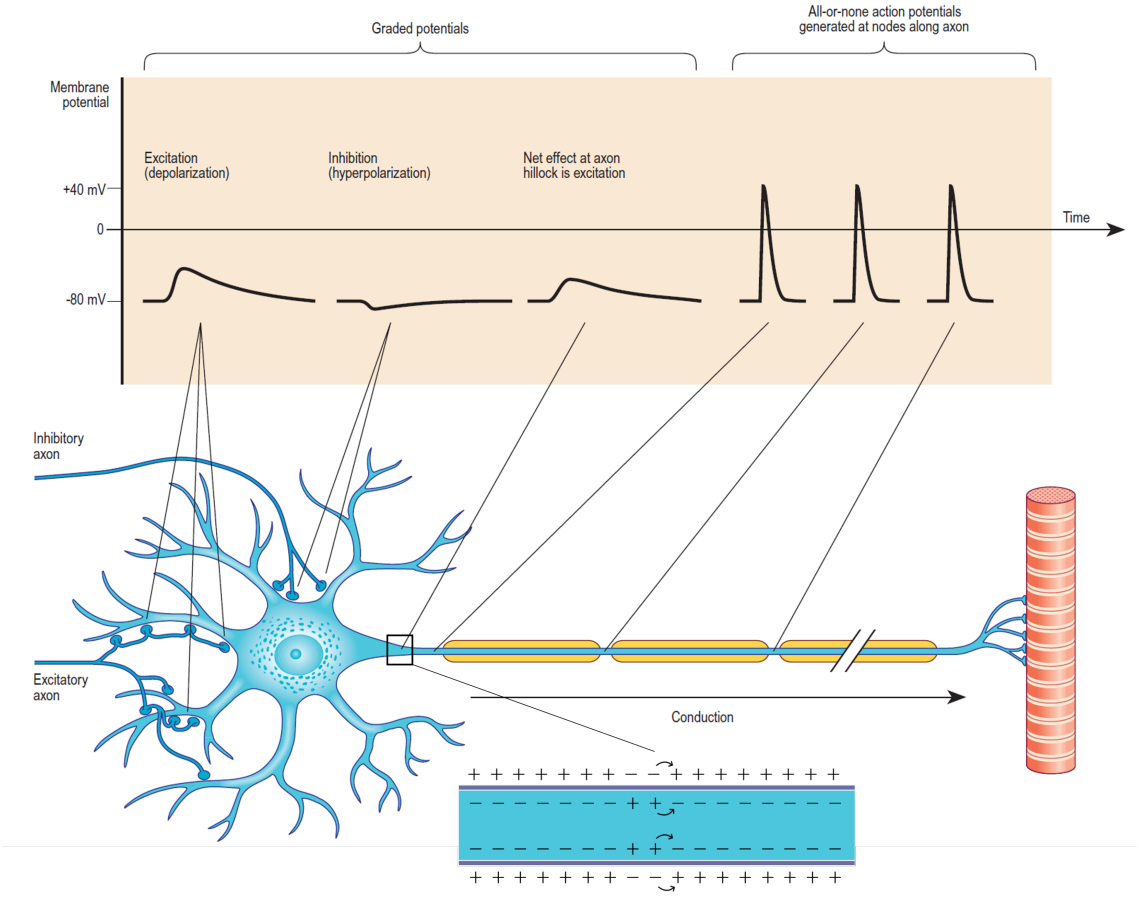


Figure 2.5: Action potential in a motor neuron is conducted through the axon until the muscle effector. Adapted from [12].

romuscular synapse, triggering the motor unit action potential (MUAP) that quickly propagates through the muscle fibres. The action potential then triggers calcium release, activating muscle contraction in under 100 milliseconds. Increasing the frequency of the neuron impulse or recruiting more motor units makes it possible to increase the produced force [13]. An electromyographic signal is the capture of the sum of multiple MUAPs. This can be achieved by invasive methods, positioning electrodes directly in the muscle or non-invasively by surface electrodes. Due to the signal's low amplitude and how it is captured, surface EMG (sEMG) has several limitations. These include being highly sensitive to external noise sources, exemplified in Figure 2.6, position shifts, skin properties and the presence of adipose tissue [14].

2.4 Soft Robotics

Achieving functionality similar to its human counterpart in artificial hands has been an ongoing topic in research. Typically, simplified approaches are capable of outperforming more complex ones. This has led to different strategies to simplify both design and control while keeping some of the anthropomorphic principles associated with the most common functions of natural hands.

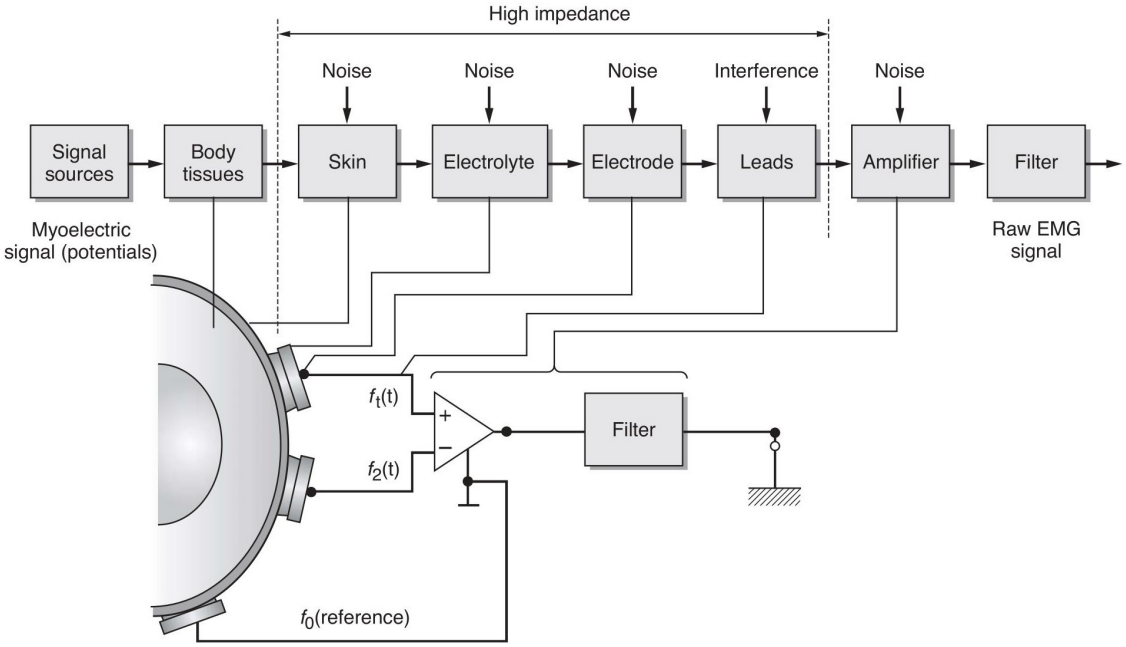


Figure 2.6: Acquisition system for electromyography with the main components that introduce noise to the signal. Taken from [14].

Not limited to prostheses, an emerging solution in artificial hands is the use of soft joints and soft actuators [15].

It is possible to distinguish the joints used in artificial hands into four types, as summarised in Figure 2.7. The concept of soft hands is inspired by nature: human joints can be compared to flexible and dislocatable robotic joints, which are fabricated using a combination of rigid structures articulated using flexible elements; meanwhile, soft continuous hands can be likened to muscular hydrostats like octopus arms and elephant trunks [15, 16]. The RBO Hand 2 is an example of a soft continuous hand which is pneumatically actuated and made of silicone rubber, polyester fibres and a polyamide scaffold [17].

While rigid joints are still dominant, soft approaches offer a more adaptable solution that can reduce the need for complex control algorithms. This stems from its compliant nature, causing the hand to adapt to the shape of the object it is grasping. Due to this, they offer a solution especially needed for hand prostheses where the difficulty of achieving high functionality in unstructured environments is aggravated by the lack of available user inputs [15].

Another advantage of soft joints is that they result in a more robust artificial hand that can better withstand impact. This is particularly important in human-robot interactions and prostheses since rigid joints can result in more unsafe behaviour [15].

Softness can also be present in terms of actuation where compliant solutions are being used to replace the traditional rigid approach. This can be achieved either by impedance or stiffness modulation or by soft and flexible materials [15].

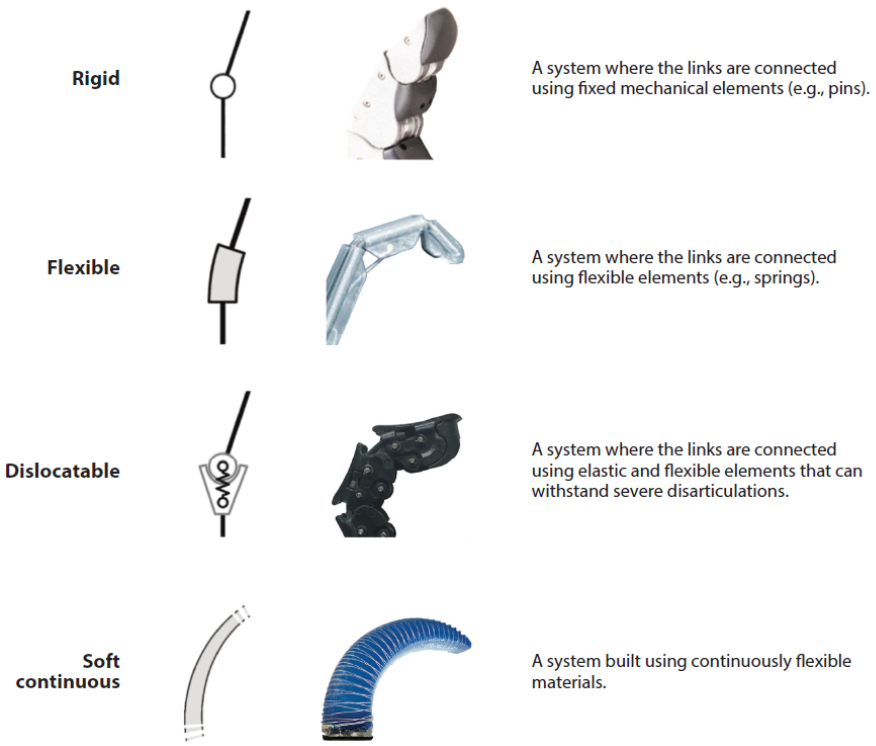


Figure 2.7: Joint types of robotic hands. Taken from [15].

In complex anthropomorphic hands, full actuation of the joints results in the biggest manipulation possibilities. However, the high number of actuators requires controllers that are too complex. Furthermore, it is associated with higher costs and difficulties in hand design. Underactuated rigid hands can result in few contacts between the hand and the grasped object due to the lack of compliance, causing inadequate grasping. While rigid or soft joints and actuators are not directly correlated with the actuation level, compliant behaviour enables underactuated hands to retain their adaptivity [18].

2.5 Human Tactile Feedback

The high mechanical complexity of the human hand is associated with a precise and intricate natural control scheme. In order to successfully complete an object manipulation task, humans rely on diverse sensory information to control the different motor systems. For example, vision can be used to predict the appropriate grasp type while proprioception can be used to control task kinematics. However, vision and proprioception only provide limited information about the contact between the hand and the object and its stability. Because of this, humans rely on tactile sensors for dexterous manipulation [19]. Accordingly, it has been shown that when subjects cannot rely on tactile information, due to trauma, illness or if subjected to local anaesthesia, they become unable to perform the required grip adjustments, resulting in object slip. To counteract this, they have to

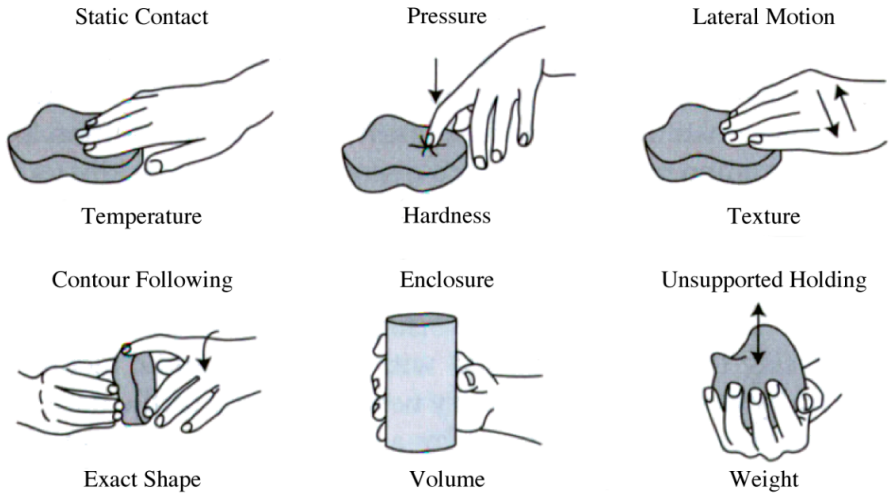


Figure 2.8: Exploratory movements for the haptic exploration of an object. Taken from [23].

adapt by using higher grip forces, exaggerating limb trajectories and simplifying the movements by, for example, reducing the degrees of freedom of the hand [20–22].

Haptic sensing is such an essential source of information that it is possible to determine the main properties of an object, such as texture, hardness and shape, through a number of manual exploratory procedures, as presented in Figure 2.8 [24].

This tactile information is obtained through different types of sensory endings like thermoreceptors, nociceptors and mechanoreceptors, respectively responsive to temperature, damaging stimuli and mechanical deformation [12]. For grasping, the most important are the mechanical afferents on the palmar surface of the hand. The four types of mechanical afferents (FA-I, FA-II, SA-I and SA-II), visible in Figure 2.9, can be separated into fast-adapting and slowly adapting afferents, which respond to, respectively, dynamic or sustained tissue deformation. Type I FA, or Meissner corpuscles, and Type I SA, or Merkel cell endings, are the most superficial of these afferents, terminating beneath the epidermis. They are located in small and specific zones of the palm, with density increasing distally, meaning they are particularly present in the fingertips. While SA-I transmits information about low-frequency deformations, FA-I is sensitive to high-frequency microstimuli caused, for example, by friction or slip. Type II afferents are present at a deeper layer of the dermis and hypodermis and are more uniformly distributed throughout the palm. The FA-II afferents, or Pacinian corpuscles, respond to transient mechanical stimuli from the forming and breaking of contact between the hand and an object. These afferents have high pass filtering properties, responding to events with frequencies between 40 and 400 Hz. SA-II afferents, or Ruffini endings, are sensitive to strain, including the shear forces formed during object manipulation [19].

Most manipulation tasks can be divided into multiple sub-phases with different mechanical behaviour. For example, a simple pick and place task can be divided into five sub-tasks: firstly, the hand reaches for the object and contact between the fingertips and the object is established; this is

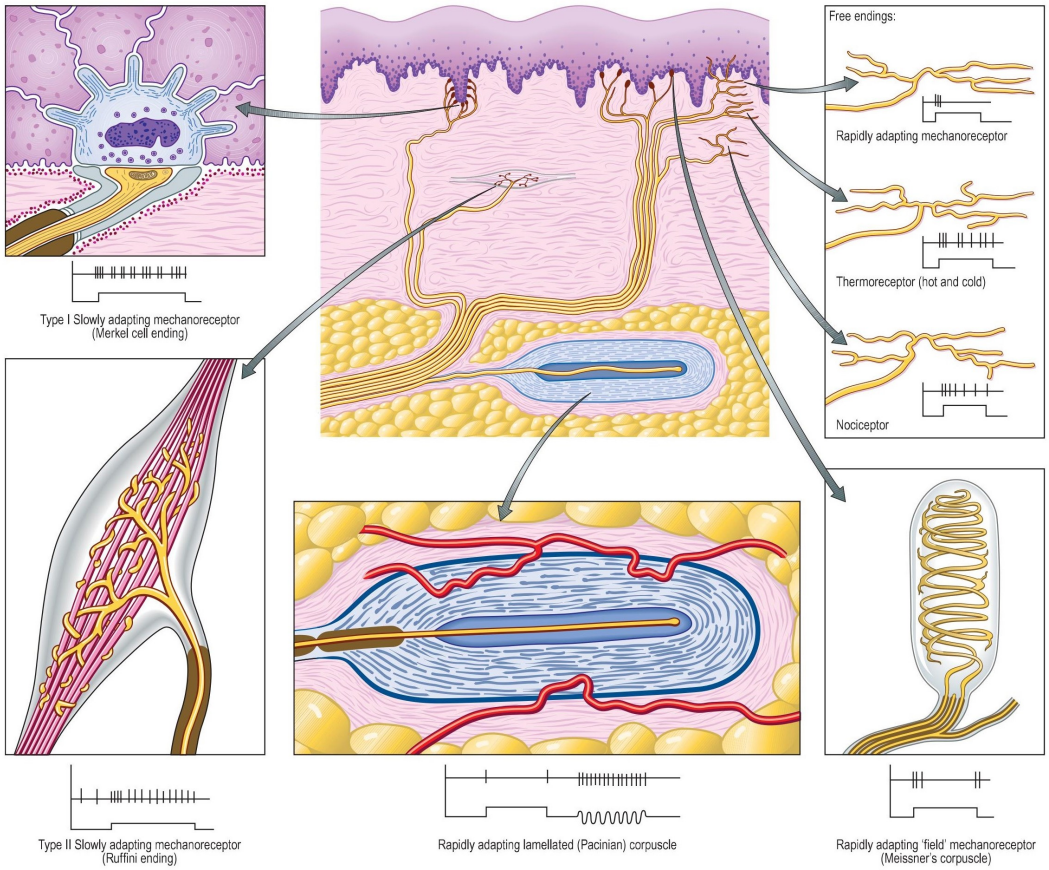


Figure 2.9: Main types of sensory endings in the palm of the hand. Below each type, the response (top) to a specific stimulus (bottom) is exemplified. Taken from [12].

followed by a loading phase where the grip force has to be adjusted while the object is being lifted from the surface; the third phase relates to the stability of the grasp while the object is moved; this is followed by the object coming into contact with the surface again, causing a decrease in the resistive force caused by the object's weight; finally, the object is released as the fingers break contact with it. Each phase results in distinct tactile signals that are compared with the predicted subgoals to enable the necessary corrections [19].

A more in-depth analysis of the response of each type of afferent during the distinct grasping phases showed that the FA afferents are mainly recruited during loading and unloading. Their response reflects the first derivative of the load force and thus is suppressed in the presence of high static finger force. In contrast, SA afferents' response was proportional to grip force and to changes in the load force [25]. The responses of the four types of afferents are presented in Figure 2.10. These findings seem to indicate that FA afferents provide information about critical incidents of instability as well as determine the frictional properties of the grasped object in the beginning stages of contact. In opposition, SA afferents sense the normal and shear forces after these properties have been understood and are instrumental in maintaining stability after the initial moments [23].

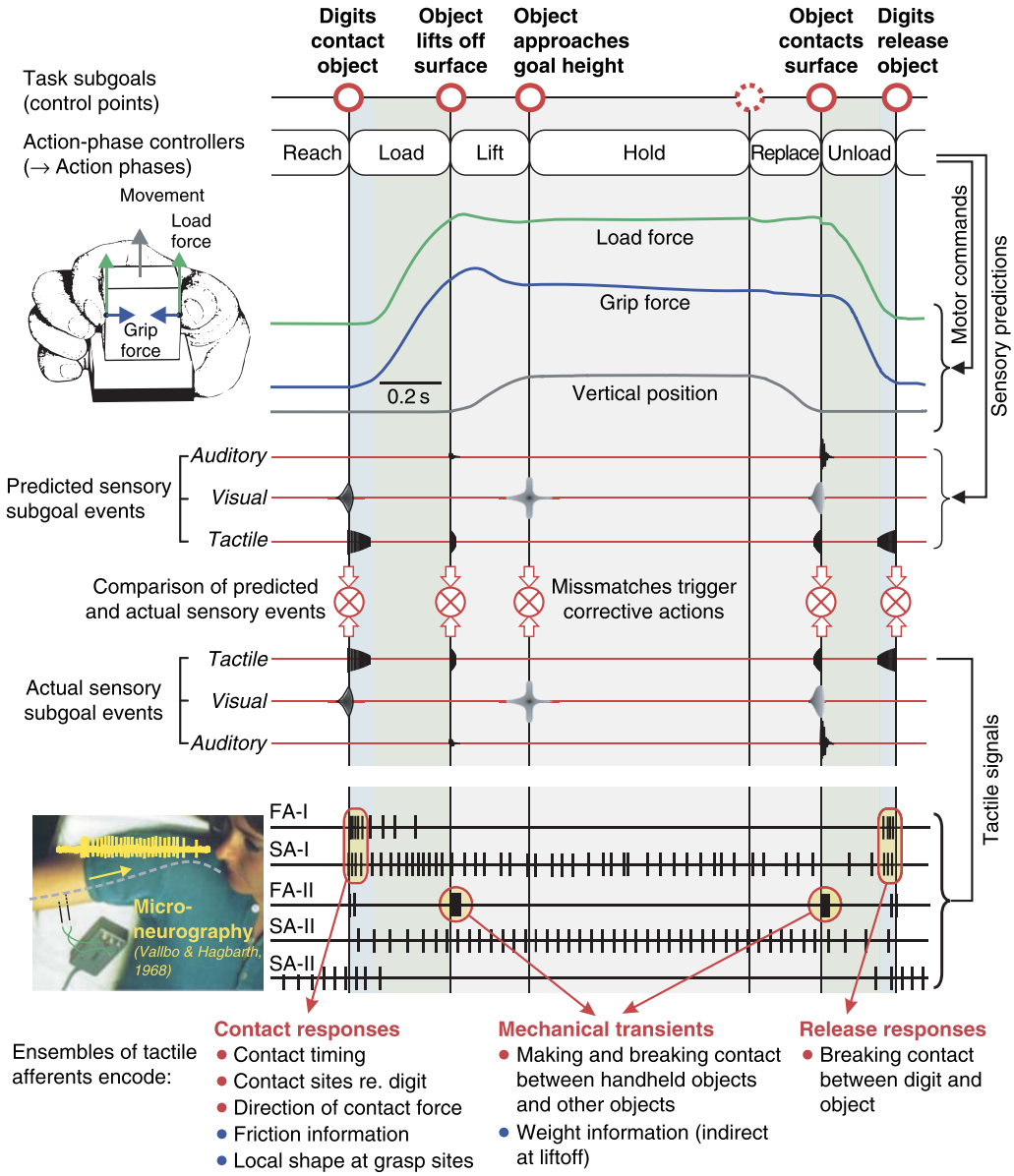
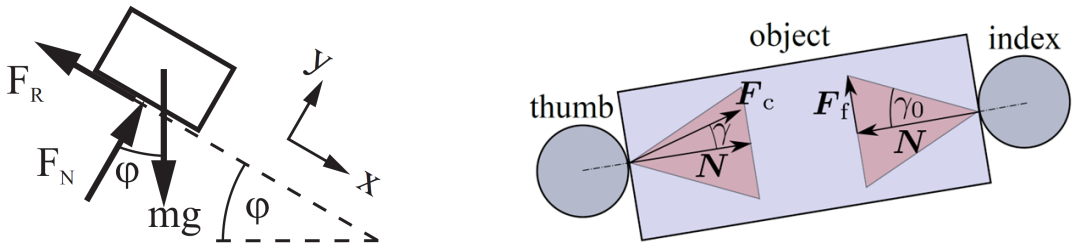


Figure 2.10: Task subgoals of a pick and place task. The afferents respond differently to the distinct grasping events. This information is then used to correct wrong predictions from other sensory inputs. Taken from [19].

Tactile information is encoded through the firing rate and relative spike timing of the afferents. With this information, predictions based on visual and proprioceptive information can be corrected in around 100 milliseconds [19]. This short reaction time indicates that the response is a spinal reflex. It has even been shown that this reflex can counteract attempts to voluntarily let an object slip [26].



(a) (b)

Figure 2.11: (a) Sketch of an experimental setup to determine the static friction coefficient. F_R is the friction force, F_N is the reaction force, and φ is the inclination of the plane. Taken from [28]. (b) Friction cone. Taken from [29].

2.6 Friction Cone

Friction can be described as the force that opposes the relative motion between two or more substances. If both substances are solids, friction can be divided into static friction, which opposes impending motion, or kinetic friction, which opposes motion once movement is already underway. It is dependent on several factors, such as the material, surface conditions, geometry, temperature and humidity [27].

Although it is a complex phenomenon involving surface deformation, interaction with wear particles, micro-fracture, electron and phonon excitation, chemical reactions and particle transfer between contacting bodies, it can be simplified to a first-order approximation frequently used in engineering. This approximation was experimentally achieved by Coulomb and is thus called Coulomb's Law of Friction. It describes the static friction coefficient as the maximum ratio between the shear (or friction) force and normal force before movement occurs and can be defined by equation 2.1, where μ_s is the static friction coefficient and F_S and F_N are the static friction force and normal force, respectively [28].

$$\mu_s = \frac{F_S}{F_N} \tag{2.1}$$

Similarly, the kinetic friction coefficient can be defined as the ratio between the shear and normal force after the static friction force has been overcome and movement is ongoing.

A simple way to determine the static coefficient of friction is to measure the necessary angle of an inclined plane to trigger a sliding motion, as seen in Figure 2.11(a). This angle (φ_0) is called the angle of friction and is related to the static friction coefficient by equation 2.2 [28].

$$\tan(\varphi_0) = \mu_s \tag{2.2}$$

Because it is a measure of relative motion, the friction coefficient is commonly used to analyse grasping in robotics. For this application, the friction cone can be described as a virtual cone defined by a vertex on the contact points between the gripper and the object's surface and the

angle of friction, as seen in Figure 2.11(b). If the contact force is contained inside the limits of the friction cone, then it can be assumed that the grasp is stable, otherwise, slippage is occurring [29].

2.7 Digital Filtering

The following section was based on the work of D. Schlichthärle (2011) [30].

The response of a linear time-invariant (LTI) system to the unit impulse function is called the impulse response, $h(t)$. For causal systems, $h(t)$ only exists for non-negative t. Using the impulse response, it is possible to calculate the response of a system, $y(t)$, to any input, $x(t)$, using:

$$y(t) = \int_{-\infty}^{\infty} x(t-\tau)h(\tau)d\tau = h(t) * x(t) \tag{2.3}$$

This can be transformed into the frequency domain through the one-sided Laplace transform, presented in equation 2.4, where s is the complex frequency:

$$s = \sigma + j\omega$$

$$F(s) = \int_{0}^{\infty} f(\tau)e^{-s\tau}d\tau \tag{2.4}$$

Applying the transformation to equation 2.3 results in equation 2.5, where $H(s)$ is the system's transfer function and represents the relation between the input and the output in the s-plane, respectively $X(s)$ and $Y(s)$.

$$Y(s) = H(s)X(s) \tag{2.5}$$

The amplitude of the frequency response can be obtained by equation 2.6, where $a(\omega)$ is the logarithmic gain in dB:

$$a(\omega) = 20\log|H(j\omega)| \tag{2.6}$$

Because the transfer behaviour can also be described as a linear differential equation with real coefficients, it is possible to express the transfer function as a function of these coefficients, where N corresponds to the order of the filter:

$$H(s) = \frac{\sum_{i=0}^{M} b_i s^i}{\sum_{j=0}^{N} a_j s^j}$$

For a second-order filter, b_0 is commonly factored out of the numerator. This becomes equation 2.7, where G is the gain at $s = 0$.

$$H(s) = G\frac{1 + b_1 s + b_2 s^2}{a_0 + a_1 s + a_2 s^2} \tag{2.7}$$

Considering only the transfer function of a complex pole pair, with unitary gain and normalising so that $a_2 = 1$, this can become:

$$H(s) = \frac{1}{s^2 + a_1 s + a_0}$$

$$H(s) = \frac{1}{s^2 + (\omega_0/Q)s + \omega_0^2}$$

In this case, ω_0 corresponds to the resonant frequency and Q, or quality factor, is the ratio between the gain at $\omega = \omega_0$ and $\omega = 0$. It can also be described as the ratio between the resonance frequency and the 3 dB bandwidth, thus being a measure of how selective the filter is.

$$Q \approx \omega_0 / \Delta\omega_{3dB} \tag{2.8}$$

All the previously mentioned relations are used to describe continuous-time LTI systems. In digital systems, t has been sampled, resulting in the input, $x[n]$, as described by equation 2.9, where T is the sampling period and n is the nth element of the input sequence:

$$x[n] = x(t)|_{t=nT} \tag{2.9}$$

Similarly to equation 2.3, the relation between input and output is now given by a discrete convolution:

$$y[n] = \sum_{k=-\infty}^{+\infty} x[n-k]h[k] = h[n] * x[n] \tag{2.10}$$

Similarly to the Laplace transform, the right-sided Z transform can be defined as:

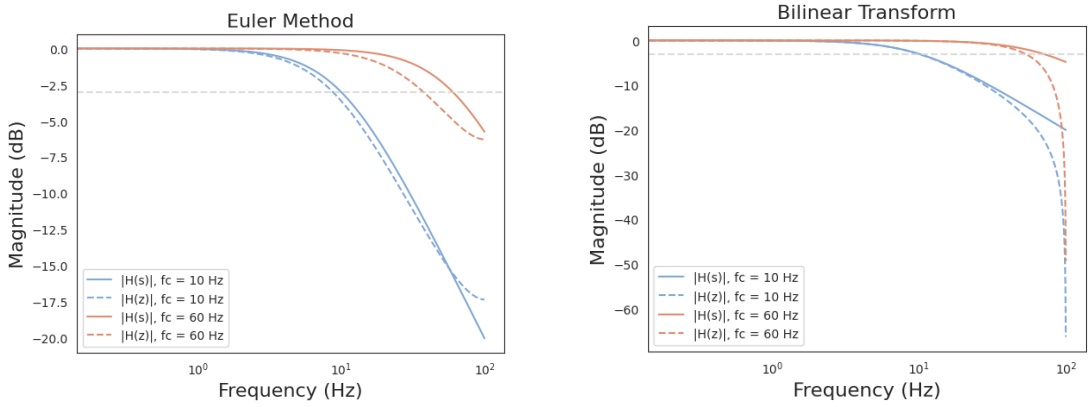
$$F(z) = \sum_{n=0}^{+\infty} f(n) z^{-n}$$

$$z = e^{(\sigma + j\omega)T} \tag{2.11}$$

Applying this to equation 2.10:

$$Y(z) = \sum_{n=0}^{+\infty} \left(\sum_{k=-\infty}^{+\infty} x[n-k]h[k] \right) z^{-n}$$

$$Y(z) = \sum_{k=-\infty}^{+\infty} h[k] \sum_{k=0}^{+\infty} x[n-k] z^{-n}$$



(a) (b)

Figure 2.12: Frequency response of two low-pass first-order analog filters and their respective digital filter. The sampling frequency in both cases is 200 Hz. The -3 dB line is plotted in grey. a) Filter was discretised using the Euler method. b) Filter was discretised using the Bilinear transform.

and considering $m = n - k$ and that the sequences are right-sided, we get:

$$Y(z) = \sum_{k=0}^{+\infty} h[k] z^{-k} \sum_{m=0}^{+\infty} x[m] z^{-m}$$

$$Y(z) = H(z)X(z) \tag{2.12}$$

By adding a delay so that $f_d(n) = f(n - n_0)$, it can be show that:

$$F_d(z) = z^{-n_0} F(z)$$

Analog filters are frequently used as a reference for the design of digital filters. To achieve this, it is necessary to obtain the frequency response of the digital filter from the frequency response of the analog filter. Starting from equation 2.11, it is possible to define:

$$s = \ln z / T$$

This can be expanded into:

$$\ln z = \sum_{n=1}^{\infty} \frac{1}{n} \left(\frac{z-1}{z} \right)^n$$

Using only the first term of this series, we can transform $H(s)$ into $H(z)$ using the Euler or difference method. This results in:

$$s \approx \frac{1 - z^{-1}}{T} \tag{2.13}$$

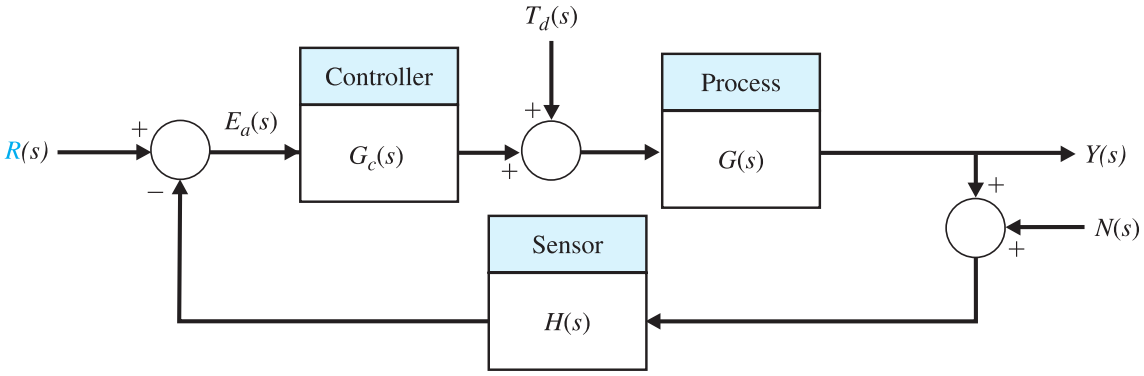


Figure 2.13: Block diagram of a closed loop controller. T_d represents disturbances to the system, N represents the measurement noise, E_a, is the error signal, Y is the output and R is the desired output. Taken from [32].

However, in most cases, this method requires a much higher sampling frequency than other methods to be able to approximate the response to that of the analog filter. This is exemplified in figure 2.12(a) where the frequency response suffers from aliasing as the frequency gets closer to the Nyquist frequency.

The Tustin method, or bilinear transform, is an alternative to the Euler method, which is based on the first element of a different expansion of $\ln z$:

$$\ln z = 2\sum_{n=1}^{\infty} \frac{1}{2n-1}\left(\frac{z-1}{z+1}\right)^{2n-1}$$

$$s \approx \frac{2}{T}\frac{z-1}{z+1} = \frac{2}{T}\frac{1-z^{-1}}{1+z^{-1}} \tag{2.14}$$

The bilinear transform has two important specific properties resulting from the compression of the frequency axis of the analog filter. Firstly, the transition bands are sharper, resulting in the need for lower-order filters to obtain similar behaviour to the analog filter. Secondly, all of the characteristic frequencies of the analog filter are shifted to lower frequencies. Both of these effects are visible in Figure 2.12(b)

2.8 Closed-loop Control

Unless otherwise explicitly stated, the following section was based on the work of D. E. Seborg et al. (2004) [31].

A controller is a system whose goal is to obtain a desired system response. Since the desired response is known, it is possible to calculate an error signal, $e(t)$, as shown in equation 2.15, that the controller uses to adjust the actuator, as exemplified in Figure 2.13. $y_{sp}(t)$ represents the set

point (SP) and $y_m(t)$ is the measured value of the controlled variable.

$$e(t) = y_{sp}(t) - y_m(t) \tag{2.15}$$

While $y_{sp}(t)$ can be time-varying, it is usually kept constant for relatively long periods of time.

One of the simplest ways of driving $e(t)$ to zero is through an on-off controller. It is commonly used, for example, in thermostats and can be described by equation 2.16, where c_{max} and c_{min} represent the on and off values:

$$c(t) = \begin{cases} c_{max} & \text{if } e(t) \geq 0 \\ c_{min} & \text{if } e(t) < 0 \end{cases} \tag{2.16}$$

Typically, a deadband is introduced to reduce the effect of measurement noise. This type of control results in continuous oscillation of the controlled variable around the SP, making it less effective and versatile.

Proportional control is another type of simple feedback control. As the name suggests, in this case, the controller output is proportional to the error signal:

$$c(t) = c_0 + K_p e(t)$$

where c_0 is the steady-state value, corresponding to the controller output when the error is zero, and K_p is the gain. By adjusting the gain, it is possible to change the system's sensitivity. Due to physical limitations, $c(t)$ is bounded between c_{min} and c_{max}. Since constant errors produce constant control reactions, proportional controllers have the disadvantage of resulting in a steady-state error.

The introduction of an integral control action can overcome this problem:

$$c(t) = c_o + K_p e(t) + K_i \int_0^t e(\tau) d\tau$$

With integral control, c changes until the steady-state error is zero or c is saturated. However, it tends to produce oscillatory behaviour that depends on its gain.

To reduce the oscillations caused by the integral control, a derivative control can be introduced, creating a proportional–integral–derivative (PID) controller :

$$c(t) = c_o + K_p e(t) + K_i \int_0^t e(\tau) d\tau + K_d \frac{de}{dt}(t) \tag{2.17}$$

This controller responds based on the rate of change of the error, acting as a predictor of future behaviour. It can improve the system's response by decreasing the time necessary to achieve the steady state. However, it can also amplify measurement noise, resulting in high-frequency oscillations. Due to this, it typically is not employed in systems with fast response and noisy measurements.

For the digital application of PID control, equation 2.17 needs to be transformed into its digital version. A straightforward version of achieving this is by approximating the integral and derivative

terms to their finite difference approximations:

$$\int_0^t e(\tau)d\tau = \sum_{n=1}^{k} e_n T$$

$$\frac{de}{dt}(t) = \frac{e_k - e_{k-1}}{T} \tag{2.18}$$

where T is the sampling period. This leads to the position form of PID control:

$$c[k] = c_0 + K_p e_k + K_i T \sum_{n=1}^{k} e_n + K_d \frac{e_k - e_{k-1}}{T} \tag{2.19}$$

From this, it is possible to obtain the velocity form:

$$\Delta c[k] = c[k] - c[k-1]$$

$$\Delta c[k] = K_p(e_k - e_{k-1}) + K_i T e_k + K_d \frac{e_k - 2e_{k-1} + e_{k-2}}{T} \tag{2.20}$$

Chapter 3

State of the Art

3.1 Myoelectric Control

As previously introduced in Chapter 2.2, body-powered prostheses are the most robust commercially available option for upper limb amputees. Advances in motor decoding strategies and hardware have improved the functionality of myoelectric prostheses. Nonetheless, this is associated with higher complexity and associated costs [11].

Most commercial myoelectric transradial prostheses are controlled using EMG signals. These signals are traditionally obtained using two or three sEMG electrodes positioned in the forearm. When the user contracts a specific muscle, the amplitude of the electrical signal in one of the electrodes will increase. By setting a threshold, users can intuitively control one DoF, such as opening and closing the hand, as is the case of the Select Myoelectric Hand (Steeper Group, United Kingdom) [5].

To increase the number of available grasps, some prostheses rely on passive movement of the joints such as the thumb or wrist. However, to be able to actively control multiple DoFs, non-intuitive control schemes have to be implemented [5]. Some of the most common non-intuitive control schemes already commercially available include: using multiple sequential muscle impulses, for example, in the i-Limb hand (Össur, Germany); muscle cocontraction, where antagonist muscles are contracted simultaneously, for example, to change the thumb position in the Michelangelo hand (Ottobock, Germany); or using different contraction speeds to control different DoFs, for example using a fast contraction to rotate the wrist while a slow contraction opens and closes the hand, as happens in the Michelangelo hand as well.

In the case of the thresholding and the non-intuitive decoders described above, an on-off controller or a proportional controller, as described in Chapter 2.8, are commonly implemented. An on-off controller executes a movement, for example, wrist rotation, at a constant speed as long as the EMG signal surpasses the threshold. On the other hand, the proportional controller will give the motor an input signal proportional to the EMG signal's intensity. This gives the user more control, allowing, for instance, the control of the speed at which the hand closes [33].

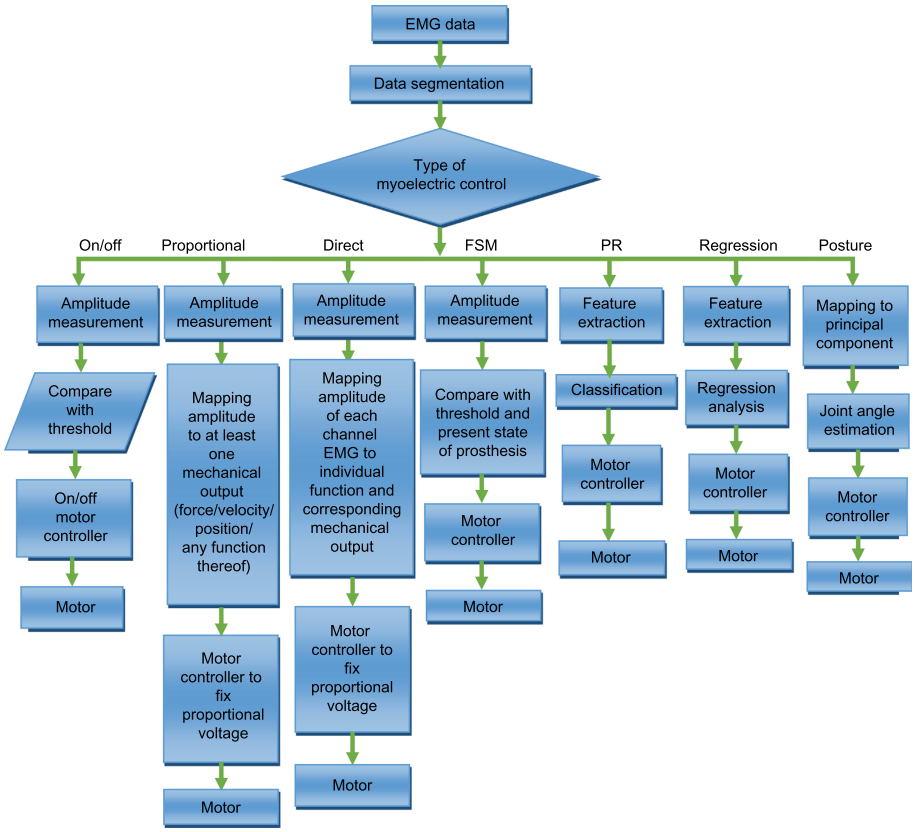


Figure 3.1: Distinct types of myoelectric control. Taken from [33].

More recently, pattern-recognition-based controllers have transitioned from being a research-only option and have started being commercialised, such as Complete Control (Coapt, USA). In this system, sEMG signals are collected using eight electrodes. This information is then translated into one of various possible movements. A wide variety of pattern recognition algorithms have been developed in research, including regressors [34] and classifiers [35]. However, they continue to have multiple limitations, such as poor out-of-laboratory performance, high computational cost and lengthy training protocols [2].

Finite state machines (FSM) are commonly implemented with classifiers. Firstly, multiple features are extracted from the EMG signal. Then, the feature vector, possibly after feature selection, is mapped into a class that corresponds to one of a fixed number of pre-defined hand postures. This mapping can be achieved using classification methods such as neural networks, support vector machines, linear discriminant analysis and k-nearest neighbour. With FSM, proportional control is not usually available [33]. An overview of the distinct types of EMG control is presented in Figure 3.1.

A strategy to improve these control strategies is to improve the input signals. This has been achieved through invasive EMG, which presents vastly better selectivity and accuracy than sEMG. However, this solution is limited to research settings due to requiring surgery, being susceptible to infection and rejection and due to the current technological restrictions of the hardware [2].

Another research solution is the use of high-density sEMG electrodes. These are able to acquire 2D images of muscle fibre activation and thus significantly increase the amount of available information, which more complex decoding algorithms can use. However, they are also limited to research settings due to requiring the use of conductive gel, the presence of artefacts and the computational cost [2].

3.2 Shared Control Strategies

As mentioned in the previous chapter, increasing a prosthesis's DoFs and degrees of actuation (DoAs) would allow for more dexterous movements. However, the limitations of the EMG signals would mean that the robustness of the decoder, which is one of the main concerns of prostheses users, would decrease [11].

Giving haptic feedback to the user has been proven beneficial [36, 37], especially in improving ownership of the artificial limb. However, the cumulative time taken to give the user the feedback signal, the user's EMG reaction, the EMG processing window and the prosthesis' response would create delays of around one second, which is far superior to the reaction time of human hands [38, 39]. This strategy is also associated with higher cognitive load [40].

To address this challenge, one effective approach is to implement shared control strategies, where additional sensing modalities are employed to create embedded low-level controllers [41]. By adopting these strategies, a portion of the control is automated, shifting some of the decision-making and intelligence from the user to the prostheses, enabling higher dexterity and robustness [11].

Shared control has already been implemented in hand prostheses in multiple modalities. For example, in [42], a multi-fingered fully-actuated hand was equipped with tactile sensors. The tactile information was used to maximise contact between the object and the desired contact points, making the hand capable of being actively compliant. In [43], a cognitive vision system composed of a camera, a distance sensor and a laser pointer mounted on the dorsal side of a hand, was used to automatically select the grasp type and aperture size. This meant that the user was only in charge of starting the hand opening and closing.

3.2.1 Tactile Slip Control

One particular shared control strategy employed in hand prostheses is tactile slippage control. With this strategy, the stability of the grasp is ensured by sensors positioned in the prostheses, which helps reduce both the user's cognitive and physical demands.

This strategy is commonly implemented in a manner that draws inspiration from human physiology, previously described in Chapter 2.5. As explained in [44], we can make a correspondence between the phases of grasping in the human nervous system with different control levels for prosthetic devices. In the first stage, the user's intentions are determined by a high-level controller. These intentions will depend on several factors, such as the physical properties of the object and its desired manipulation. Then, a middle-level controller is responsible for enacting the

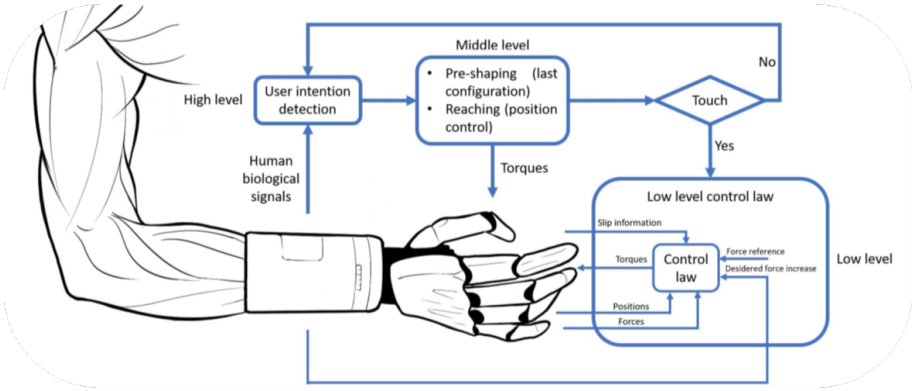


Figure 3.2: Example of a hierarchical shared control strategy inspired by human behaviour. Adapted from [44].

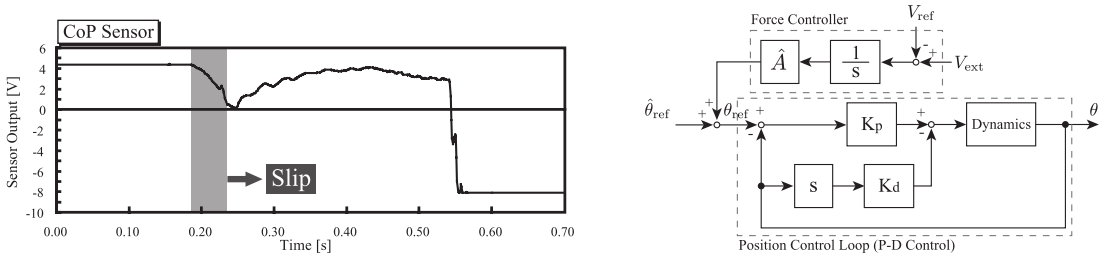
user's intention by pre-shaping the hand and executing the reaching phase. Finally, once the grasp has been established, a low-level controller ensures stability by adapting the gripping force based on the detection of slippage that may be caused, for example, by insufficient initial gripping force, movement, or external disturbances. This is exemplified in Figure 3.2.

The SensorHand Speed (Ottobock, Germany) is one of the few commercially available hands that already has embedded force sensors. The sensors are used to detect slippage and automatically increase the gripping force until the object is secure.

In research settings, slip control is a topic that has been in development for decades. Some of the earliest attempts at solving the chronic limitations of prostheses involve the development of the Southampton Hand along with the Southampton Adaptive Manipulation Scheme (SAMS) [45–49]. These works were developed with the goal of minimising the demand for user input while maintaining multiple actuators so that the user can perform a wide variety of tasks. SAMS is a hierarchical control scheme where the high-level controller is responsible for five different commands chosen based on the intensity of the EMG signal of the flexor and extensor muscles. Then, encoders on the drive motors are used for position feedback, while an electro-optical system is used for force feedback in the low-level controller. This eliminates the need to use the EMG signal for proportional control decreasing the required length of training. This control scheme was also tested in a simplified 1-DoF hand prosthesis by an amputee with myoelectric control experience, reaching performance levels similar to the user's usual prosthesis [50].

Some methods for slip control do not rely directly on a binary detection of slippage and focus instead on controlling the applied force. For example, in [51], a centre of pressure (CoP) sensor was shown to respond to slippage before it occurred, as shown in Figure 3.3(a). Since the force output decreases when slip is imminent, a force control system was implemented, as seen in Figure 3.3(b). The desired joint angle was determined through proportional control of the CoP sensor's voltage. This new desired value was implemented using a PD controller. However, this controller was only validated by grasping objects of different weights. Because of this, its response to disturbances like impact or sudden weight change is unknown.

While this work focuses on force sensors and tactile information to implement slip control,



(a) (b)

Figure 3.3: a) Response of a centre of pressure sensor to a slip event. b) Force controller implemented based on the centre of pressure sensor. Taken from [51].

other types of sensors have achieved similar results. For example, [52] uses inertial measurement units (IMUs) and [53] uses optical sensors to detect slippage. In [54], a more extensive review of the different modalities of robotic tactile sensing is presented.

In the following sections, the three main methods of slip control will be reviewed more in-depth.

3.2.2 Vibration Detection

As discussed in Chapter 2.5, one of the anti-slip strategies that humans reflexively use is based on sensing the high-frequency vibrations caused by friction when slip is imminent. Based on this understanding, multiple strategies have been implemented to assess grasp stability.

In [55, 56], force-sensitive resistors (FSR) were placed at the fingertip of an anthropomorphic hand to simultaneously measure the normal grasp force and detect slippage. Resistive flex sensors (RFS) were placed on the dorsal side of the fingers as proprioceptive sensors. The control algorithm can be divided into four stages. In the pre-shape stage, the user selects one of the possible movements using EMG, and the low-level controllers of the fingers involved in that movement are activated. Then, the fingers close until they establish contact with the object, detected through the derivative of the RFS signals. Then, the controller moves onto the force control stage, where the FSR and RFS signals and the motor current are used as input of a neural network to calculate the necessary motor input to ensure a stable grasp. The neural network was used with the intent of compensating for the affordable sensor's low linearity. The force stage is alternated with the detection stage, where the derivative of the FSR and RFS are used to detect if the object is slipping. When this happens, the force reference at the force stage is increased. While the use of a neural network was a strategy able to surpass the limitations associated with inexpensive sensors, it must be noted that machine learning methods are associated with higher computational costs which restrict their application [39].

In [38, 57], strain gauges were placed in the thumb of a 3-finger hand with 1 DoA. As can be seen in Figure 3.4, high-frequency components in the derivative of the shear force detected through the strain gauges are correlated with slip events, with different slip events having distinct frequency components. Implementing multiple filters resonating at distinct frequencies makes it possible to

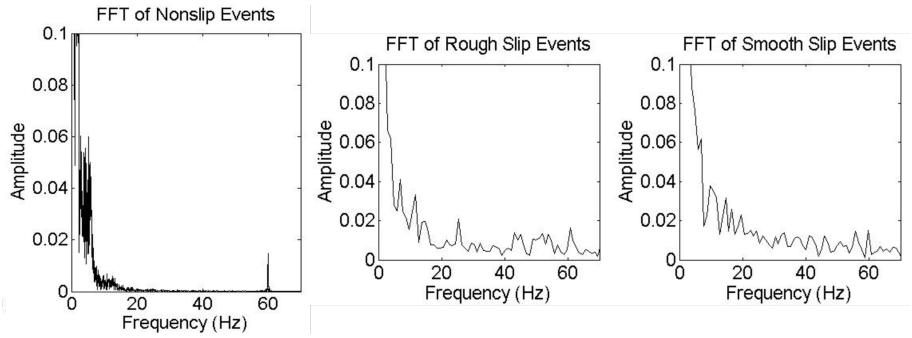


Figure 3.4: FFT of a non-slip event and two slip events. In the case of non-slip events, the signal has almost no components above 20 Hz, with the exception of the 60 Hz electrical noise. In the case of the slip events, higher frequency components are much more present. Taken from [38].

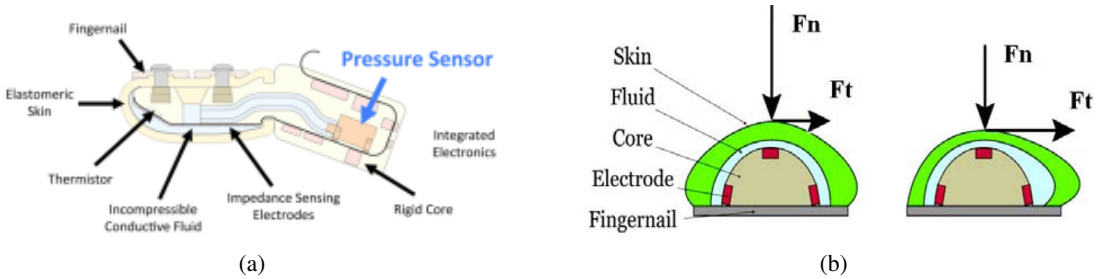
detect slippage using a threshold. This was used to implement two sliding mode controllers that were also compared with a traditional PD shear force controller in terms of success rate and object deformation. The proposed integral sliding mode controller resulted in the most minor object deformation while still ensuring that the object was not dropped.

In [9, 58], FSR sensors were once again placed at the fingertips of the thumb and index finger, in this case of a 5-finger, 11 DoF and 5 DoA anthropomorphic hand. The normal force derivative was thresholded to create a binary slip signal. This signal was integrated over time and included in the error functions of the finger positions that were driven to zero by a PD controller. The desired finger positions were calculated by a PI force controller where the desired force was predetermined. To validate the controller, objects were grasped by the hand and then an impulsive force to the object induced slip. They were able to achieve a 99.4% success rate in detecting slip events and 100% in compensating for slippage.

3.2.3 Friction Cone

While the previously presented works implemented binary slip signals by detecting the associated vibrations, others have chosen to focus on the concept of the friction cone, described in Chapter 2.6.

In [59], the thumb of a commercial anthropomorphic, 2-DoAs hand was replaced with the BioTac biomimetic sensor [60]. This sensor is a variable impedance sensor based on the dislocation of a fluid between an elastomeric skin and electrodes that is capable of measuring normal and shear force, as seen in Figure 3.5. Due to the noisy nature of the sensor, the shear force was calculated using a Kalman Filter. The ratio between shear and normal force was then compared with a fixed estimate of the coefficient of friction. If the shear-to-normal force ratio is inadequate, the hand opens or closes by a preset amount. The hand was controlled using a proportional position controller. To validate the controller, a cup was held while being filled. In 95% of cases, the controller was capable of not dropping the object, with failure happening in the trial with the fastest force perturbation.



(a) (b)

Figure 3.5: a) Cross-sectional schematics of the BioTac sensor. Taken from [23]. b) Normal and shear force applied to the BioTac sensor. Taken from [59].

In [61], hemispherical robotic fingertips were equipped with 6-DoF force/torque sensors. These sensors were used to obtain the critical ratio between shear and normal forces in real-time using the LuGre model in combination with the acceleration and force applied to the object, instead of using the simplification of the static friction coefficient. The friction parameters of the model were obtained based on two strokes over the object's surface with different accelerations. However, this method is limited to homogenous, undeformable and ungrooved surfaces.

3.2.4 Machine Learning

More recently, machine learning methods have started being explored in an attempt to surpass the simplifications needed to implement the previously mentioned analytical approaches.

In [62], a 7x4 grid of pressure sensors was placed in each finger of a 2-finger gripper, along with IMUs to measure joint angles. The pressure images, together with the proprioceptive data of 1000 grasping trials, were used to train and test multiple convolutional neural networks. The best-performing case was able to achieve a failure prediction rate of 92.7%.

In [63], multilayer perceptrons were used to detect slip and deformation based on the uSkin sensor. This sensor is made up of 24 optical sensor points capable of measuring both normal and shear forces. By implementing a position controller with a fixed increment in the desired position when slip is detected, they had a 97.5% rate of successful grasping using a two-fingered gripper.

3.2.5 Method Comparison

As previously mentioned, slip control has been extensively studied in the field of robotics, and distinct successful approaches have been implemented.

In [29], three approaches, each based on one of the concepts explained before, were compared using a two-finger setup with BioTac sensors. The friction cone was implemented based on the contact normal and measured contact force. The vibration detection was implemented through bandpass filtering the raw pressure signal. For the machine learning method, a random forest classifier was trained with 750 samples, each composed of the motor position, tendon force, BioTac impedance, BioTac temperature and filtered and unfiltered BioTac pressure collected over a time window of 80 ms.

The three methods were then compared on three parameters. Detection quality was evaluated by grasping an object that is attached to a motor by a stiff tendon. Sensitivity to impact was assessed by creating a disturbance next to the experimental setup to see the effect of the external vibrations. Sensitivity to movement was analysed by having the fingers grasp the object and then move to see if the noise created by the hardware components affected the detection.

The results from this study found that the friction cone method was capable of detecting slip before and while it occurred, with good robustness to both impact and motion. However, its implementation is more challenging as it requires previous knowledge about the grasp to create a model. While the bandpass filter had a similarly short reaction time, it was very susceptible to both types of disturbances. Finally, the random forest was similar to the friction cone when it came to sensitivity to disturbances. However, it had a much longer reaction time and required an extensive training phase.

Based on this study, this dissertation proposes a combined approach to slip detection. This approach attempts to exploit the robustness of the friction cone model. To achieve this, the vibration detection is employed to obtain the required model. Due to its longer reaction time and higher computational costs, methods relying on machine learning algorithms were not explored further.

Chapter 4

Methodology

This chapter starts by describing the hardware used throughout this work. Particular emphasis is given to the force sensors as they are not commercially available and were custom-developed. This is followed by a subsection that describes how all the different components were interfaced. The following section describes the implemented control algorithms. Finally, a description of the experimental protocols and how they were analysed is given.

4.1 Materials

4.1.1 Force Sensors

4.1.1.1 Design and Settings

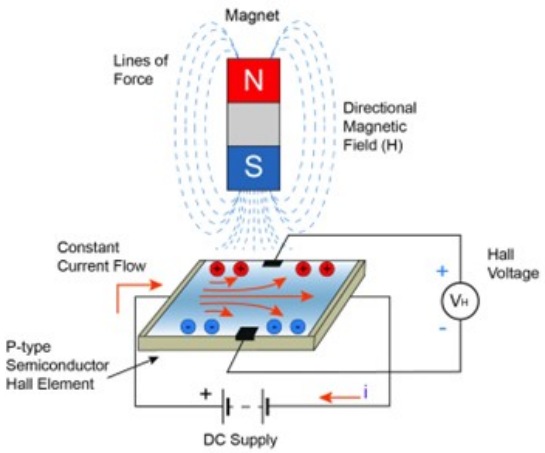
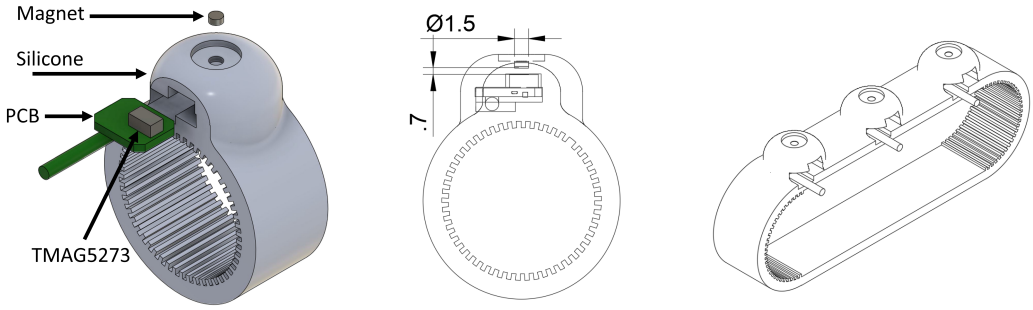


Figure 4.1: Appearance of a Hall Voltage on a semiconductor due to the presence of a current flow and a perpendicular magnetic field. Taken from [64].

The force sensors used in this work are soft-embedded Hall effect sensors. The Hall effect, demonstrated in Figure 4.1, states that if a magnetic field is applied perpendicularly to the current



(a) (b) (c)

Figure 4.2: Hall effect force sensors. (a) Exploded view of the ring sensor. This includes a magnet, silicone cover, PCB and IC (TMAG5273). (b) Placement of the magnet, located 0.7 mm above the IC. (c) Band design used for the palm area. Taken from [67].

flowing in a conductive material, an induced voltage will appear perpendicular to the magnetic field and the current [65].

Each force sensor has a TMAG5273 (Texas Instruments, USA) magnetic sensor, which is composed of three Hall effect sensing elements. This allows for the measurement of magnetic flux in three axes. This Hall effect sensor has an integrated 12-bit ADC, various selectable configurations such as two selectable magnetic ranges, integrated temperature compensation and configurable averaging for noise reduction. Range ± 40 mT was chosen for the x and y axes, and range ± 80 mT was chosen for the z-axis. Temperature compensation was set to 0.12 %/°C, corresponding to the temperature coefficient of neodymium magnets. The update rate selected corresponds to the averaging of every 32 samples, corresponding to the best signal-to-noise ratio (SNR) configuration.

An N45 disc magnet with axial magnetisation, diameter of 1.5 mm and height of 0.5 mm is positioned 0.7 mm directly over the sensing elements in the integrated circuit (IC). By applying a force to the silicone dome, the relative position between the magnet and the IC will change. This will result in a change in magnetic field, which the IC outputs as a digital signal. The magnetic flux density can then be mapped into force after calibration, described in more detail in Chapter 4.1.1.3.

The magnet and IC are positioned inside a silicone shelling with a shore hardness of 35A. This was chosen based on previous experiments and due to its similarity to the usual silicone skins used with prostheses. Two different designs were developed: ring-shaped for placement in the fingers and band-shaped for placement in the palm, as seen in Figure 4.2. The dome shape where the printed circuit board (PCB) and magnet are embedded was inspired by [66]. The surface of the silicone that contacts with the hand was fabricated with ridges to increase friction between the silicone and the hand to avoid the effect of the rotation of the sensors in the force measurements.

4.1.1.2 Fabrication

For the fabrication of the force sensors, two moulds were designed. These included positives of the PCBs and magnets so that they could be inserted later. They were printed in polylactic acid (PLA) using fused deposition modelling (FDM).

Next, the mould was filled with silicone and put in a vacuum chamber to eliminate air pockets in the cured silicone. To create vacuum, a one-stage vacuum pump with 1.8 CFM air displacement and 1/4 HP, the VP 115, was used along with a 6 L vacuum chamber to achieve a vacuum of approximately 27 mmHg. After approximately 5 minutes, the silicone was gradually taken out of vacuum and left to cure for around 3 hours before being extracted from the moulds. Then, the magnet and the PCB were inserted into the moulded holes. These were then covered with degassed silicone and left to cure for at least another 3 hours.

4.1.1.3 Calibration

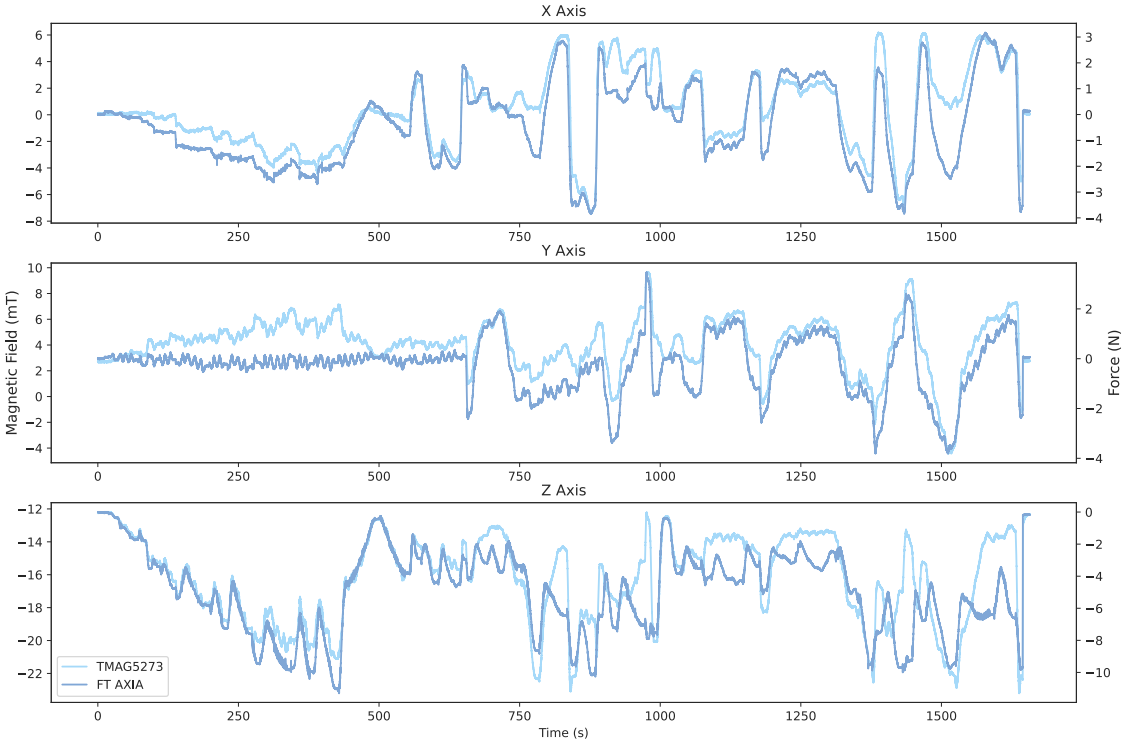


Figure 4.3: Data used to calibrate the force sensors. Ground truth obtained using the FT AXIA was used to map the magnetic flux obtained from the TMAG5273 into force.

Due to the fact that each sensor was manually fabricated, they present slight physical differences that result in specific mappings between the magnet displacement and the applied force. Hence, they were individually calibrated. For this, the calibration setup was made up of a Panda robotic arm (Franka Emika, Germany) and an FT AXIA 80-M20 6 DoF sensor (ATI Industrial Automation, USA).

The calibration was implemented in three phases. Firstly, only normal force was applied, with step increases between 1 N and 14 N. In the second and third phases, forces are applied at 90º and 45º angles with two different normal force values (5 N and 14 N). This is exemplified in Figure 4.3 where the signal obtained from the Hall effect sensors and the ground truth from the FT AXIA are plotted for one of the rings. This data was used with a second-order polynomial transformation and a linear regressor for each ring axis. The regressions for the rings used in this work obtained an R^2 score of 0.94, 0.93 and 0.94 for the x, y and z axes respectively, when tested with 30% of the data.

4.1.1.4 Communication and Setup

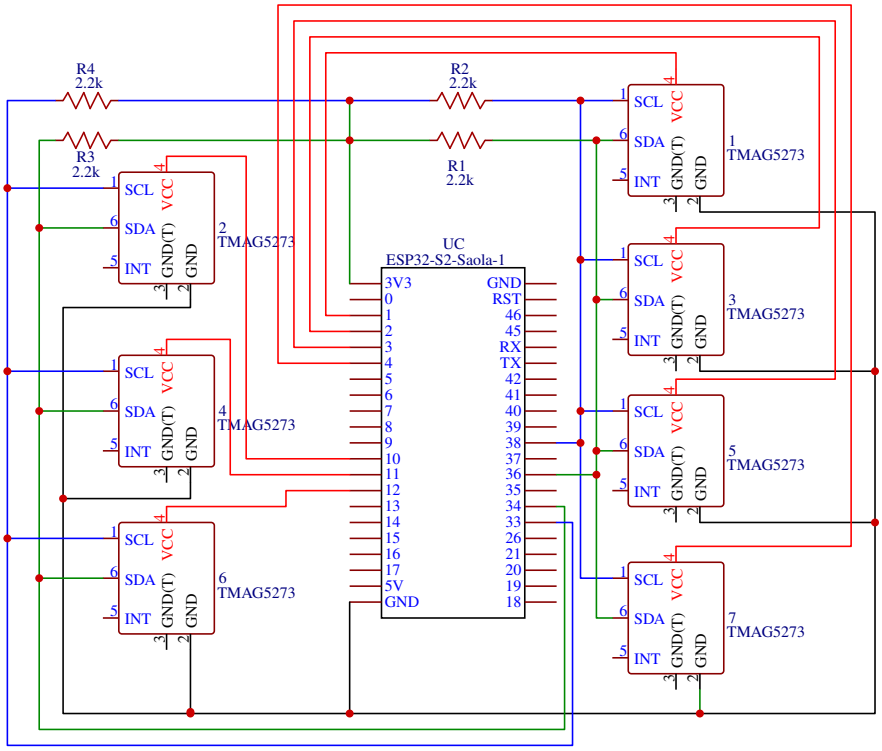


Figure 4.4: Electronic schematics of the force system. The seven sensors are connected to two distinct I2C buses. Each sensor is powered by its own GPIO.

The force sensors and the laptop were connected through a microcontroller using I2C and UDP. The IC used in the force sensors has a configurable I2C address, allowing their direct connection to the μC. In this case, they were connected to an ESP32-S2-Saola-1 (Espressif Systems, China) programmed in C through the Arduino IDE. This μC has a 240 MHz CPU, 2.4 GHz WiFi, two I2C buses and 43 programmable GPIOs. To achieve a higher sampling frequency, the seven ICs were divided into two groups to connect with each I2C bus at 1 MHz clock speed, as seen in Figure 4.4. Each sensor was powered individually through a GPIO to allow for a sequential change of the I2C address.

The data from the sensors was then streamed through UDP to the computer, where it was processed in Python. For this, the μC connected to a WiFi access point that was set up from the laptop. In the Python script, the connection is established using the socket module. With this configuration, a sampling frequency of approximately 200 Hz was achieved.

4.1.1.5 Placement

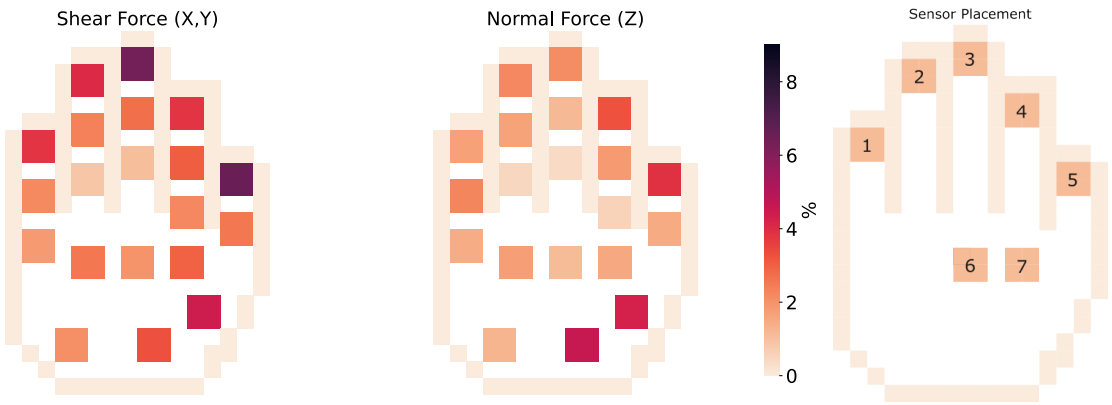


Figure 4.5: (a) Contribution of the hand regions to shear and normal force in activities of daily living. Taken from [67]. (b) Placement of the sensors in the robotic hand.

The placement of the sensors in the hand was chosen based on previous work [67]. In this work, the spatial and temporal distribution of force in the hand while performing daily living activities was studied, with emphasis on the analysis of shear forces. Results, summarised in Figure 4.5(a), showed the high contribution of the fingertips and thenar eminence to the grasping force, in both the shear and normal directions.

Based on this, five sensors were placed on the fingertips of the robotic hand and two were placed in the palm. In the human hand, the thenar eminence had a higher contribution than the rest of the palm. However, in the robotic hand, presented in the next section, the palm is non-compliant and does not conform to the grasped object. Due to this, the sensors in the palm were instead placed in the upper palm, as shown in Figure 4.5(b).

4.1.2 Robotic Hand

Initially, this work was developed with the intent of using the qb SoftHand Research (qbrobotics, Italy) in the experimental setup. However, before the experiments were set to begin, there was a hardware malfunction, and the hand became unusable. For this reason, the hand was replaced by the qb SoftHand Research 2. While the concept behind the two hands is similar, the main difference between them is the number of actuators. While the SoftHand Research 2 has two motors, which allow for pinch and power grasping as well as in-hand manipulation, these features were not explored as they are not available in the SoftHand Research (qbrobotics, Italy), which

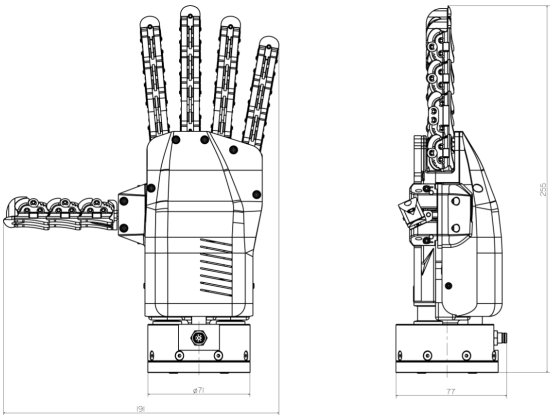
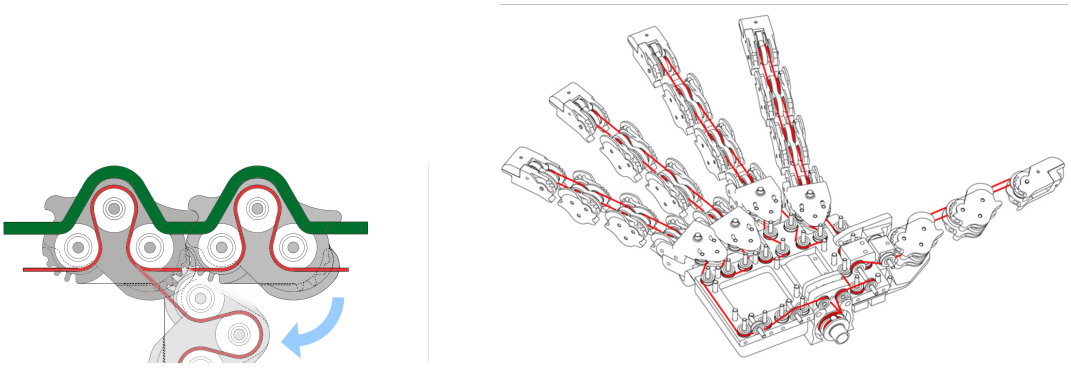


Figure 4.6: Schematics of the SoftHand. Taken from [68].

has only one actuator. To decrease the impact of the hand change, the input was adapted to have a similar closing response as in the SoftHand Research. For simplicity, the hand will, from now on, be referred to as the SoftHand.

The SoftHand, visible in Figure 4.6 is an anthropomorphic, highly underactuated hand with 19 DoFs distributed in four fingers and one opposable thumb, and two actuators. The hand weighs 0.94 kg and can achieve a payload of 3 kg [68]. This hand was developed following the soft robotics principles described in Chapter 2.4.

The hand utilises compliant rolling-contact joints in the IP joints, represented in Figure 4.7(a) and conventional revolute joints in the MCP joint. To achieve a rest configuration with stretched fingers, the hand has elastic ligaments made of polyurethane rubber with distinct levels of pre-tensioning, depending on the joint. This allows the hand to move similarly to the human hand. Its actuation is accomplished using a single tendon routed through all the joints using pulleys, as seen in Figure 4.7(b). The tendon opposes the ligaments' resistance, forcing the fingers' flexion. This enables grasp adaptivity without the use of differential gears [18].



(a) (b)

Figure 4.7: SoftHand (a) Rolling-contact articulation with tendon and ligaments. (b) Tendon routing. Taken from [18].

The hand was interfaced with Python using RS-485 serial communication. Utilising its embedded PD control, the hand was controlled by inputting a closure level between 0 and 23000, corresponding respectively to fully open and fully closed. Because they have no proprioceptive sensors, it is impossible to determine each finger's closure level.

4.1.3 Robotic Arm

Besides being used for the calibration of the force sensors, the robotic arm was also used to make sure that the validation protocol of this work was replicable between the multiple trials and control schemes.

The robotic arm used was the Panda robotic arm (Franka Emika, Germany). This arm has 7 DoFs, can achieve velocities up to 2 m/s in the end effector and has a repeatability of +/- 0.1 mm.

The robot was interfaced using the Franka Control Interface (FCI) accessed using the C++ library libfranka [69]. The FCI allows for direct control of the arm using an external PC via Ethernet.

4.1.4 Electromyography Armband



Figure 4.8: Myo Armband (Thalmic Labs, Canada).

The EMG data was acquired using the Myo (Thalmic Labs, Canada), shown in Figure 4.8. The Myo is an armband, meant to be worn around the forearm, with eight bipolar dry electrodes and one 9-axial IMU. There is one operational amplifier for each of the EMG electrodes. The data can then be transmitted to another device through a Bluetooth Low-Energy (BLE) module [70].

The open-source Python library PyoMyo [71] was used to receive the data from the Myo. Although the Myo can stream the raw data at 200 Hz, the signal used for the EMG control was a rectified and filtered signal with a sampling rate of 50 Hz.

4.1.5 Inertial Measurement Unit

An IMU, the MPU-6050 (TDK InvenSense, USA), was used to measure the displacement of the grasped objects. It has a 3-axis gyroscope, 3-axis accelerometer and 16-bit ADCs for the digitisation of the output. The range of the accelerometers was set to ± 8 g, and the range of the gyroscopes was set to ± 500 °/s.

Similarly to the setup of the force sensors, the IMU was connected to a μC, the ESP32C3 (Espressif Systems, China) using I2C. This μC was then connected to the laptop using UDP. The data was sampled at approximately 330 Hz.

The IMU was directly screwed to the objects in order to measure their acceleration.

4.1.6 Interfacing Overview

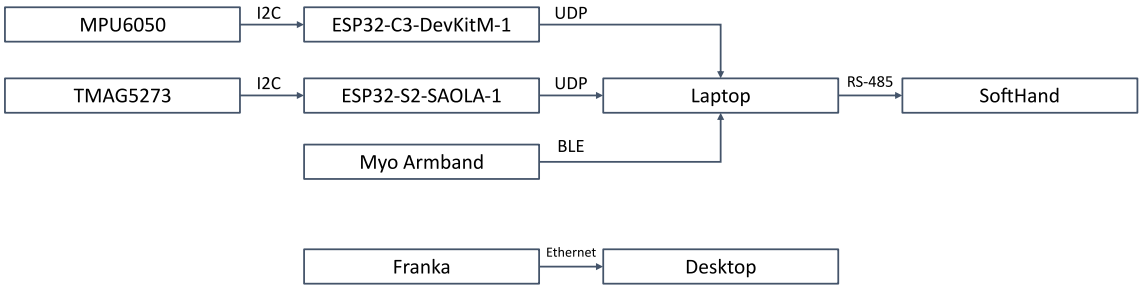


Figure 4.9: Overview of the full hardware system and its interfacing.

With the exception of the robotic arm, all modules were interfaced in Python 3.9 with a laptop running on Windows 11 with a 3.30 GHz 8-core CPU. An overview of the entire system is presented in Figure 4.9.

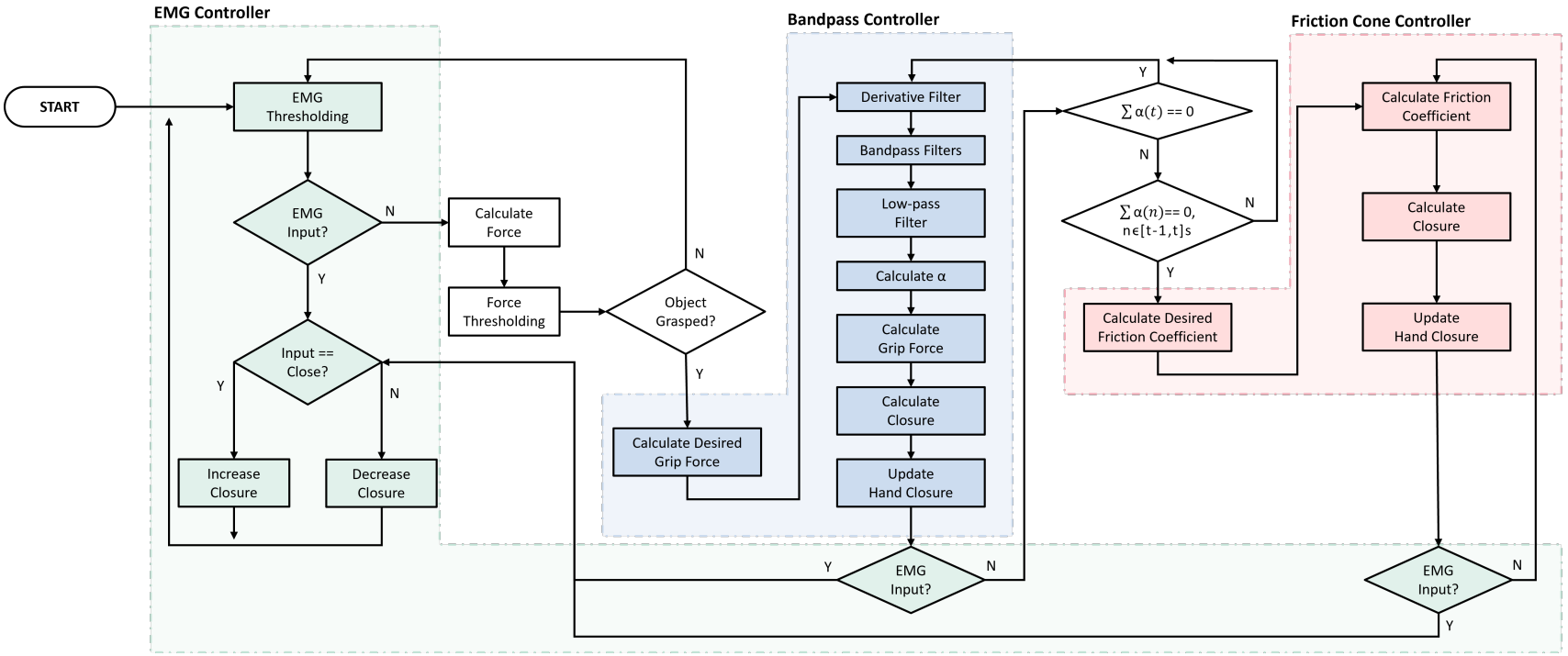


Figure 4.10: Control workflow of the proposed strategy. The three control states are highlighted in distinct colours.

4.2 Combined Shared Control

As presented in Chapter 3.2, there are numerous strategies for detecting instability during grasping. Each of these strategies is associated with distinct advantages and limitations. In [29], it was found that using the concept of the friction cone to detect slippage is more suitable to daily life settings, such as the ones faced by prostheses users due to its short reaction time and robustness to external disturbances. However, this method has the disadvantage of being dependent on various parameters such as surface texture and object weight and shape. It is feasible to obtain a model for the friction cone, for example, in industrial settings where tasks are usually repetitive and occur in controlled environments. In opposition, this method would not be helpful in daily life due to the impracticality of studying every object and environment before interaction. Comparatively, it was found that using the bandpass method was easy to implement, as it does not require prior knowledge of the object. However, this method was much more sensitive to external disturbances caused by movement and environmental vibrations. Considering the limitations of both these methods, this work proposes a combined approach to slip detection. Inspired by the human physiology presented in Chapter 2.5, firstly, slip should be detected based on the presence of high-frequency vibrations in the grasping force. Then, to maintain this stability, the control should focus on keeping the balance between the shear and normal forces.

Three different control states can describe this proposed strategy. The main state is an On/Off EMG control. As mentioned previously, the EMG data was transmitted from the Myo armband to the laptop, where it was filtered and rectified. Then, the electrodes were grouped based on their position in the forearm into an anterior and posterior group that will be activated, respectively, during flexion or extension of the wrist. If the sum of the signals from one of the groups passes a predetermined threshold without the co-activation of the opposite group, the hand will close or open with a fixed velocity. This high-level control state is able to override the two others so that the user input will always take priority over the lower-level controllers. This is essential to allow the user to manipulate objects when desired.

Once there is no EMG input and the grasping of an object has been detected by a force threshold, the controller moves into the shared control states. The initial shared control strategy is based on bandpass filtering of the shear components of the force signal. This method is used to obtain a stable grasp of the object even if the closure level of the hand chosen by the user is not sufficient. After one second of no slippage being detected, the grasp is considered stable, and a model of the friction cone is calculated. Then, the controller moves onto the friction cone state. This was done to exploit the robustness of the friction cone model without the necessity of obtaining this model before the grasp and without assuming a constant model for all different conditions. The control workflow of the proposed strategy is presented in Figure 4.10.

4.2.1 Force Module

While it was possible to calibrate the sensors, this calibration was not implemented in the controller and was only used for the posterior data analysis. This was done for two reasons. In the

first place, to keep the reaction time as short as possible. Secondly, to avoid any possible damping of the signal's higher frequency components due to the calibration.

Considering this, there are only two steps in the pre-processing of the force information. Firstly, the offset inherent to these sensors was removed, taking as reference the first five samples of each trial. The offset data corresponding to the x and y-axes of each of the seven sensors was directly inputted into the bandpass slip detection module, resulting in a filter input signal of size 14. To obtain the value of the total force in each axis, the absolute values of the sensors were summed. These three values were transmitted to both the bandpass and the friction cone controller.

4.2.2 Bandpass Filtering

4.2.2.1 Slip Detection

The bandpass filtering slip detection implemented here was based on [38], where the derivative of the shear force was shown to have higher frequency components when slip is present. Based on this, each input signal is filtered individually with a fifth-order digital filter. This filter is composed of three main stages. The first stage is a high-pass filter that differentiates the signal, discarding the low-frequency components. Then, the signal is filtered twice by a second-order bandpass filter, resonating near ω_n. Finally, the signal is filtered using a low-pass filter to eliminate the higher-frequency noise. This can be described by the transfer function in equation 4.1. The quality factor of the bandpass filter, ζ, was experimentally chosen to obtain a narrow bandwidth.

$$H(s) = s\left[\frac{\omega_n^2}{s^2+2\zeta\omega_n s+\omega_n^2}\right]^2\left[\frac{440}{s+440}\right] \tag{4.1}$$

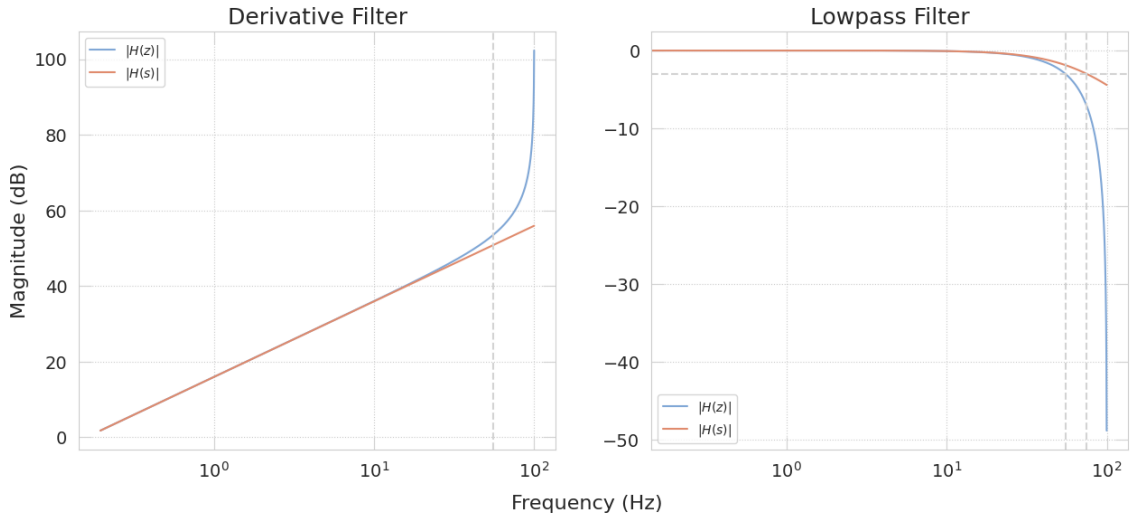
The bilinear transform represented in equation 2.14 was used to transform this transfer function into discrete time. Considering equation 4.2, where T represents the sampling period, the difference equation for the high pass filter can be directly obtained from equation 2.14. This results in equation 4.3, which was used to implement the filter.

$$K = \frac{2}{T} \tag{4.2}$$

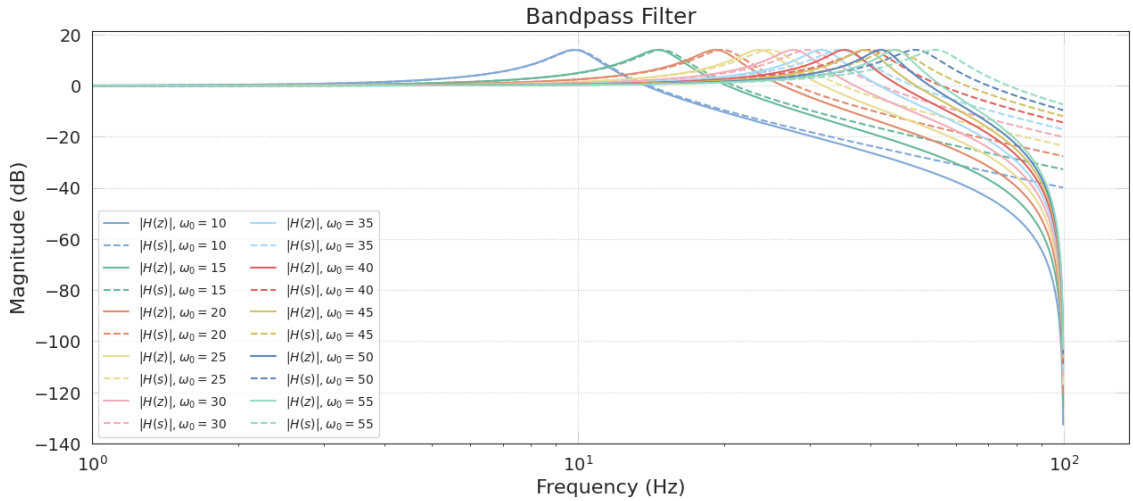
$$y_{hp}[n] = K(x_{hp}[n] - x_{hp}[n-1]) - y_{hp}[n-1] \tag{4.3}$$

Following the same method, the bandpass and low-pass filters' discrete transfer functions can be represented, respectively, by equations 4.4 and 4.5.

$$H_{bp}(z) = \frac{\omega_n^2 + 2\omega_n^2 z^{-1} + \omega_n^2 z^{-2}}{(K^2+2\zeta\omega_n K+\omega_n^2)+(2\omega_n^2-2K^2)z^{-1}+(K^2-2\zeta\omega_n K+\omega_n^2)z^{-2}} \tag{4.4}$$



(a)



(b)

Figure 4.11: Frequency response of the applied digital filters and the analog filters they were based on. a) The light grey dashed lines mark the 55 Hz and the dark grey dashed line marks the 75 Hz. The dotted line marks the -3 dB.

$$H_{lp}(z) = \frac{440(1+z^{-1})}{440+K+(440-K)z^{-1}} \tag{4.5}$$

From this, it is possible to obtain, once again, the difference equation with which to apply the filter recursively, as shown in equation 4.6 for the bandpass filter and equation 4.7 for the low-pass filter.

$$y_{bp}[n] = \frac{\omega_n^2}{K^2+2\zeta\omega_n K+\omega_n^2}x_{bp}[n] + \frac{2\omega_n^2}{K^2+2\zeta\omega_n K+\omega_n^2}x_{bp}[n-1] + \frac{\omega_n^2}{K^2+2\zeta\omega_n K+\omega_n^2}x_{bp}[n-2] - \frac{2\omega_n^2-2K^2}{K^2+2\zeta\omega_n K+\omega_n^2}y_{bp}[n-1] - \frac{K^2-2\zeta\omega_n K+\omega_n^2}{K^2+2\zeta\omega_n K+\omega_n^2}y_{bp}[n-2] \tag{4.6}$$

$$y_{lp}[n] = \frac{440(x_{lp}[n]+x_{lp}[n-1]) - (440-K)y_{lp}[n-1]}{440+K} \tag{4.7}$$

The bandpass filter was implemented in parallel in 10 different frequencies between 10 Hz and 55 Hz, with 5 Hz increments. The frequency response of the analog and digital filters is represented in Figure 4.11. As the filters were discretised using the bilinear transform, their response is influenced by the characteristic axis compression. This was taken into consideration when choosing the resonance and cutoff frequencies. Since the derivative filter starts having a very different frequency response to its analog equivalent for frequencies above 55 Hz, this was used as the cutoff frequency of the digital low-pass filter, corresponding to an analog filter with a 75 Hz cutoff frequency.

The parallel filtering of the input signal with 14 elements results in an output signal with 140 values. If at least one of these values surpasses the pre-determined threshold, the slip state, α is equal to 1. Otherwise, α is equal to 0. For each resonance frequency, a different threshold was applied.

4.2.2.2 Control

To determine what input should be given to the hand, a proportional-integral controller was implemented based on the force measurements and the slip state. This controller can be described by equation 4.8, where x is the desired closure level of the hand, F_d is the desired force, F is the measured force, K_i and K_p are, respectively, the integral and proportional gain and e_s is the slip error.

$$x = K_p(F_d - F) + K_i\int_0^{t_f}(F_d - F)dt + e_s \tag{4.8}$$

F_d is defined as the force when the shared controller is initiated after there is no longer any EMG input. Both F_d and F are calculated as the vector norm of the total gripping force, as described by equation 4.9 where n is the number of sensors, in this case, equal to seven.

$$F = \sqrt{\left(\sum_{i=1}^{n} |F_{x_i}|\right)^2 + \left(\sum_{i=1}^{n} |F_{y_i}|\right)^2 + \left(\sum_{i=1}^{n} |F_{z_i}|\right)^2} \tag{4.9}$$

The slip error corresponds to the number of times slip has occurred and is defined by equation 4.10, where α is the slip state described in Section 4.2.2.1 and K_s is the slip gain. The use of the integral of the slip state results in a stable increment of the closure level of the hand while slippage is occurring. Because the desired force is not altered, once there is no longer an external disturbance and slippage has stopped, the hand starts opening again.

$$e_s = K_s \int_0^{t_f} \alpha dt \tag{4.10}$$

The discrete-time transformation of equation 4.8 was calculated to be able to implement the digital controller. The result is presented in equation 4.11, where T is the sampling period and K_0 is the last received EMG input corresponding to the closure level when F_d is defined.

$$x[t] = K_0 + K_p(F_d - F[t]) + K_i T \sum_{n=0}^{t} (F_d - F[n]) + K_s \sum_{n=0}^{t} \alpha[n] \tag{4.11}$$

This value, x, is directly inputted to the hand where an embedded PD controller drives the closure error to zero.

4.2.3 Friction Cone

Once no slippage has been detected by the bandpass method for at least one second, the grasp is considered momentarily stable and the control state changes to the friction cone. To initialise the friction cone, the desired friction coefficient, μ_d, is calculated. Five force samples were used in this calculation to reduce the effect of the noise intrinsic to the force sensors.

Similarly to the previous method, the friction cone was implemented using a PI controller, described by:

$$x = K_p(\mu_d - \mu) + K_i \int_0^{t_f} (\mu_d - \mu) dt \tag{4.12}$$

When discretised, and considering that K_0 is again defined as the last input from the previous control state, this transforms into:

$$x[t] = K_0 + K_p(\mu_d - \mu[t]) + K_i T \sum_{n=0}^{t} (\mu_d - \mu[n]) \tag{4.13}$$

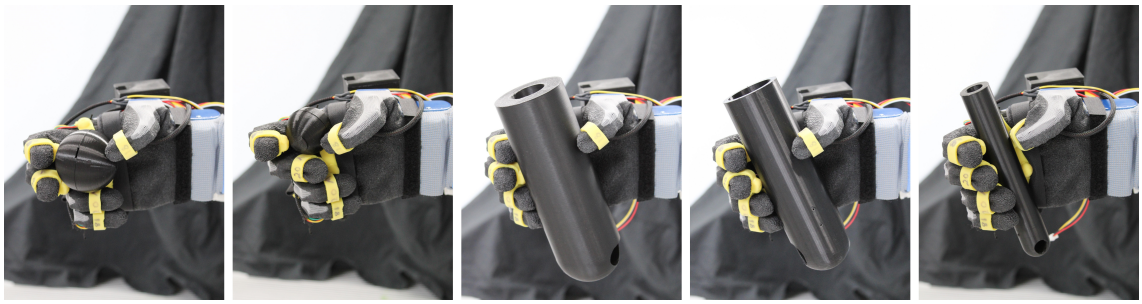


Figure 4.12: Objects used in the validation corresponding to tripod, pinch and cylindrical grasping.

Similarly to μ_d, five samples were used to calculate μ, as seen in equation 4.14, where F_S is the shear force and F_N is the normal force, calculated, respectively, by equation 4.15 and 4.16.

$$\mu[t] = \frac{1}{5}\sum_{n=0}^{4}\frac{F_S[t-n]}{F_N[t-n]} \tag{4.14}$$

$$F_S = \sqrt{\left(\sum_{i=1}^{n}|F_{x_i}|\right)^2 + \left(\sum_{i=1}^{n}|F_{y_i}|\right)^2} \tag{4.15}$$

$$F_N = \sqrt{\left(\sum_{i=1}^{n}|F_{z_i}|\right)^2} \tag{4.16}$$

This controller attempts to keep the ratio between shear and normal force close to the desired ratio. This avoids both over-squeezing when the ratio decreases and slippage when this ratio increases.

4.3 Protocol

4.3.1 Controller Validation

To compare the new approach with the state-of-the-art controllers, the protocol was split into four sections, each with a distinct controller: no controller, bandpass filtering, friction cone and the proposed combined controller. In the case of the no controller, the closure level of the hand was kept constant throughout the trial. In the bandpass controller, only the controller described in Chapter 4.2.2 is active. In the friction cone controller, only the controller described in Chapter 4.2.3 is active. To implement this, the friction model was obtained immediately after the hand had reached its final position instead of waiting until the grasp was considered stable. In the combined controller, the entire proposed architecture, described in Chapter 4.2, was implemented.

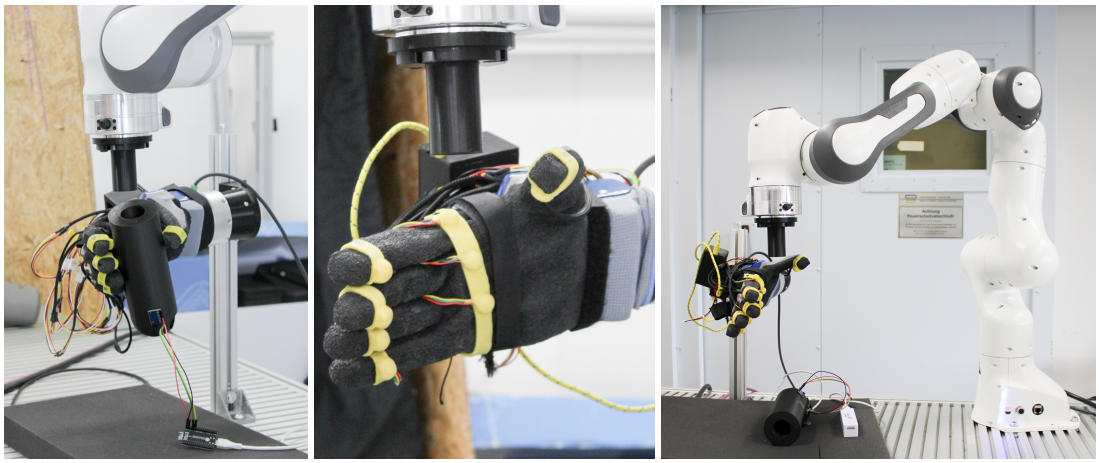


Figure 4.13: Validation Setup.

In all cases, the EMG module was substituted by directly inputting the closure level to the hand to improve repeatability between trials.

Five objects, described in Table 4.1, were 3D printed to test the controllers. As can be seen in Figure 4.12, they correspond to three cylindrical power grasps, a tripod grasp and a pinch. The IMU was screwed directly to the inside of the balls, while in the case of the cylinders, it was screwed to the outside surface on the lower half of the cylinder.

A cylindrical end-effector was printed and attached to the robotic arm so that it could be used to push the objects. The hand was screwed to an adaptor connected to an aluminium profile so that it was fixed at the wrist and suspended at a fixed position above the table. The robotic arm was moved so that its initial position was located immediately above the grasped objects. The hand was sensorised with seven sensors in total: one ring in each fingertip and two sensors in a band in the upper palm. The μC and the battery that powered it were enclosed in a 3D-printed casing strapped to the wrist of the hand. The whole setup is observable in Figure 4.13.

The initial closure level of the hand was set to one of three levels equivalent to 20%, 25% and 30% of total hand closure for all objects, with the exception of the small ball and small cylinder. In those cases, the 20% closure was not recorded as it was not enough to establish contact between the sensors and the object.

Each object was manually handed to the hand before it closed. Once the object is only being held by the robotic hand, the robotic arm moves down 2 cm to strike the object before moving 1 cm back in the opposite direction and waiting for 1 second. This action was repeated two more times so that the object was hit by the end-effector three times in each trial. The trajectory of

Table 4.1: Physical properties of the objects used in the validation.

Object	Large Ball	Small Ball	Large Cylinder	Medium Cylinder	Small Cylinder
Weight (g)	17.3	9.4	89.4	78.1	28.4
Diameter (mm)	55	40	60	50	25

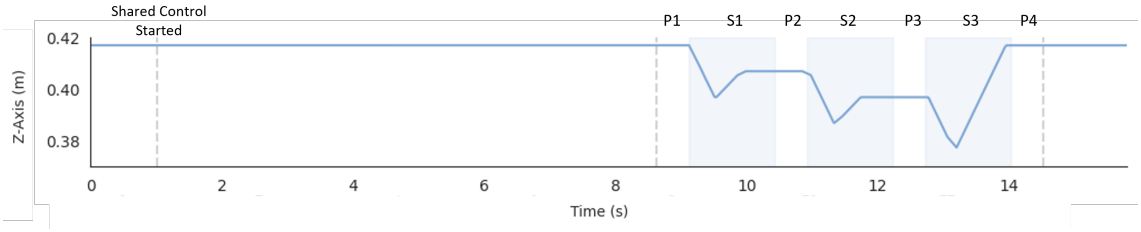


Figure 4.14: Trajectory of the end-effector for the controller validation. The pre/post-impact intervals are marked with the letter P while the intervals where the impacts happen are marked with the letter S.

the end-effector of the robotic arm is plotted in Figure 4.14. As is shown in this figure, each slip event was separated into three time intervals corresponding to pre-, during and post-impact. The post-impact interval is coincident with the pre-impact interval of the following event. Each trial was repeated five times, resulting in a total of 260 trials and 780 slip events.

4.3.1.1 Statistical Analysis

To evaluate the performance of the different controllers, four metrics were selected as the main focus: average and maximum force and average and maximum acceleration. These were calculated for each of the P and S intervals. Then, the distributions of these metrics were first checked for normality using the Shapiro-Wilk test. This normality test was used to select the appropriate statistical test. In the case of normality, repeated measures ANOVA would have been used to determine the statistical significance of the differences between the distributions. For non-parametric distributions, the Friedman test was implemented for the same purposes as the ANOVA. The statistical significance was determined based on right-tailed chi-square critical values. When the tests implied there was significant difference, a post-hoc pairwise analysis was implemented using the Wilcoxon test. The tests were implemented using the Scipy [72] and Pingouin [73] Python libraries.

4.3.2 Slip Detection

To assess the quality of the slip detection, the signal was divided into the S and P intervals presented in Figure 4.14. To create a ground truth, it was considered that in the P intervals no slip is occurring while the S intervals represent slip events. If during the S intervals, slip is detected at least once, the prediction is considered a true positive (TP), while a false negative (FN) corresponds to undetected slip. In contrast, the P intervals were classified as true negatives (TN) if no slip was detected throughout the interval, while false positives (FP) correspond to at least one detection of slip. These values were used to calculate the accuracy, precision, recall and F1 score according to the following definitions:

$$accuracy = \frac{TP + TN}{TP + FN + TN + FP}$$

$$precision = \frac{TP}{TP+FP}$$

$$recall = \frac{TP}{TP+FN}$$

$$F1 = \frac{2 \times precision \times recall}{precision + recall}$$

4.3.3 Human Comparison

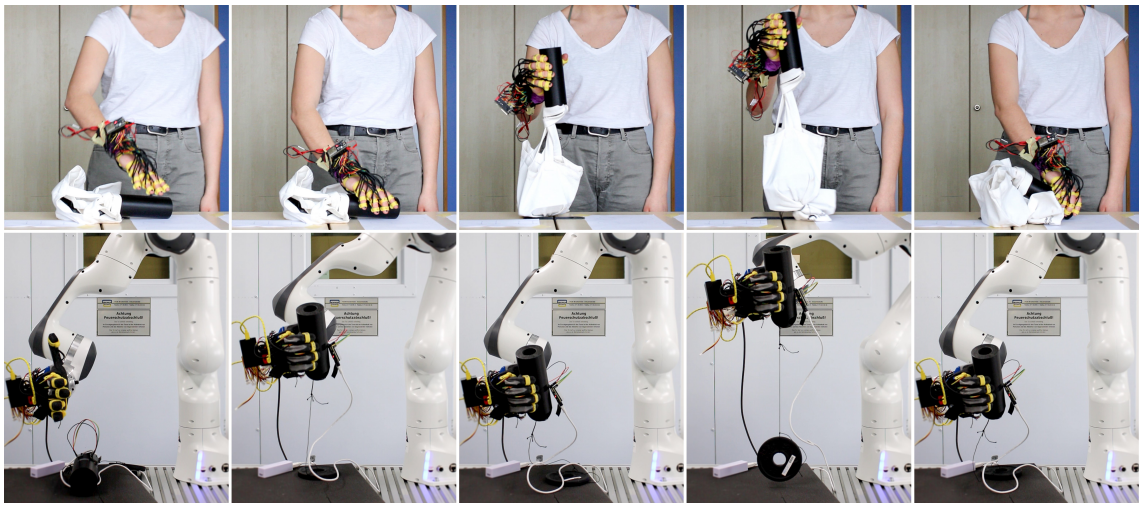


Figure 4.15: Protocol for the human study (top row) and protocol for its comparison with the controllers' response (bottom row).

As the approach here studied is based on human physiology, the evolution of the grasp over time was compared to the natural human grasp. The protocol followed here is an adaptation of previous work where six subjects were asked to grasp, using their dominant hand, the large cylinder. Once grasped, the subjects had to lift the cylinder until the weighted bag attached to it was entirely lifted from the table. The subjects were unaware of the weights inside the bag, making them have to adapt the applied force based only on tactile information. Their hands were sensorised with twenty force sensors similar to the ones used in this work, one in each phalanx and six in the palm. This task was repeated with three weights (0 kg, 1 kg and 3kg). Further details about this study can be found in [67].

To have a similar setup, a 0.5 kg weight was attached to the large cylinder using a non-elastic string. The hand was directly connected to the robotic arm as its end-effector, with the thumb pointing directly up. The cylinder was handed to the hand until it finished closing to 20% closure level. It was then moved 20 cm up so that the weight would be entirely hanging. It was held in that position for 2 seconds before being moved to its original position. This protocol can be visualised, along with the human study protocol, in Figure 4.15. One trial was executed for each of the four

controllers. Following the same processing done in [67], time was normalised between 0 and 1 and the samples were synced based on the trajectory of the robotic arm.

Chapter 5

Results

Two important distinctions should be noted to avoid confusion in the following chapter. In this context, average and mean will be used with distinct meanings. Average will be used to refer to the the average value of force or acceleration across time, extracted from the experimental trials. In contrast, mean will be used to refer to the average value of the distributions of the chosen metrics. The second distinction is related to the use of g to denote the standard acceleration of gravity, while g was previously used in Chapter 4 to refer to grams.

5.1 Slip Detection

An example of the output of the filtering used for slip detection is presented in Figure 5.1, corresponding to a trial using the small cylinder and an initial closure of 30%. For simplicity reasons, only the filtered signal for the y-axis of the force is plotted for the lowest and highest bandpass resonance frequencies, along with the respective threshold. As can be seen, the three slip events have different frequency components. In this case, while the 10 Hz filter is able to detect the three slip events, the 55 Hz filter can only detect the first one. However, it is able to detect the first slip event 0.458 s before the 10 Hz filter. While the slip events were able to be detected by the thresholds, the first instants of the signal are characterised by a much higher amplitude signal and thus are also classified as slip events.

Table 5.1 summarises the results obtained for the slip detection algorithm for the distinct objects, categorised by their size and the initial closure level. The results were obtained from the trials conducted for the controller validation using the bandpass and combined controller.

The performance of the detection algorithm varies depending on the object type. Generally, the performance is superior for the cylinders compared to the balls. This is suggested by the overall higher accuracy (68% vs. 61%), precision (73% vs. 64%), recall (56% vs. 51%) and F1 score (63% vs. 57%).

Within the cylinders, there is a noticeable trend between object size and performance. The algorithm's performance improves with the decrease in diameter based on accuracy, recall and F1 score. The metric most affected by the object's diameter is the recall, ranging from 33% for the

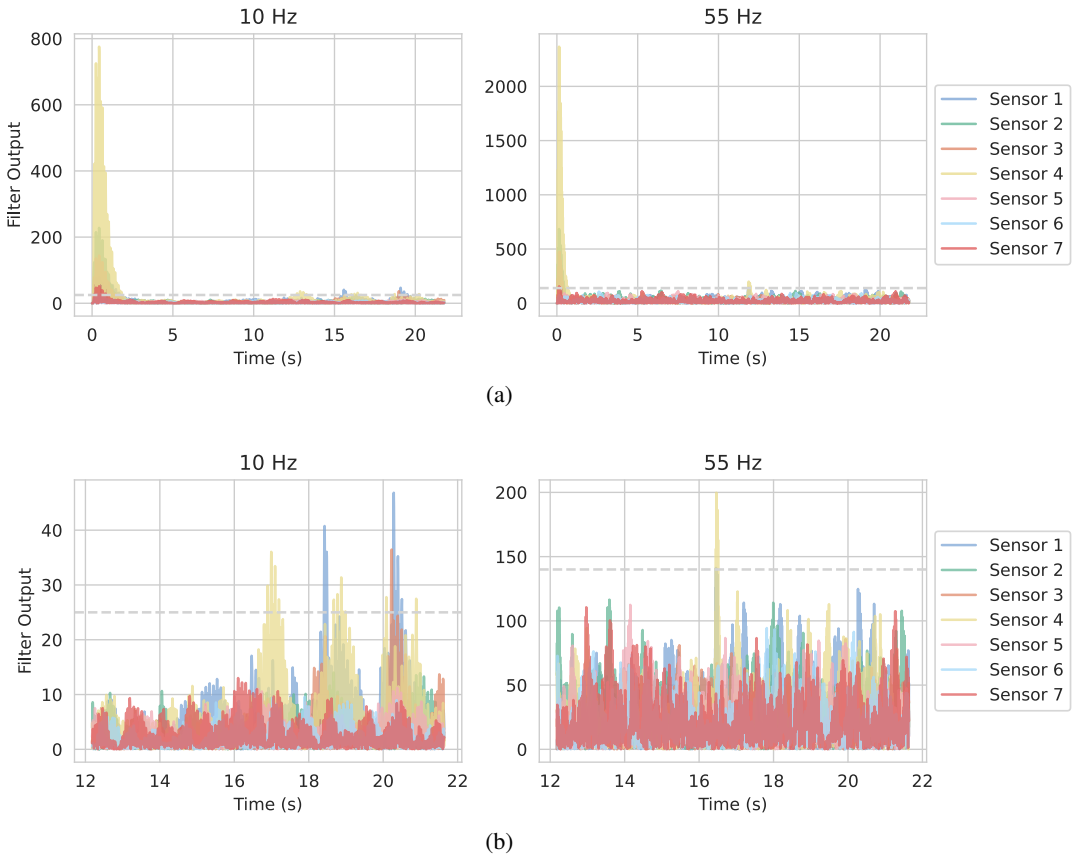


Figure 5.1: Example of the bandpass filtering output for the sensor in the index finger. Each resonance frequency is plotted along with its corresponding threshold (dashed line). (a) the signal for the entirety of the trial. (b) zoomed in to the time interval where slip is induced.

large cylinder to 95% for the small cylinder. The small cylinder consistently corresponds to the best performance for all initial closure values with an overall F1 score of 81%. In contrast to the cylinders, the diameter of the balls has a relatively smaller influence on the performance of the detection algorithm, with the F1 score ranging from 58% for the large ball to 53% for the small ball.

The initial closure level also impacts the performance of the slip detection. For the large cylinder, the detection is considerably worse for the highest closing level, with an F1 score of 23% compared to 45% overall. The lowest initial closure performs the worst for the balls and the medium cylinder.

Across most conditions, precision is higher than recall, with overall scores of 64% and 51%, respectively, which means the ability to avoid false positives was superior to the ability to detect all slip events. The opposite is true for both closure conditions using the small cylinder, where recall was significantly superior to the results obtained with the other objects.

To minimise the effect of the lower recall in the calculation of the response time, only the samples pertaining to the small cylinder were considered. The reaction time was calculated as the difference in time between the highest peak in acceleration and the first subsequent detection of

Table 5.1: Accuracy, precision, recall and F1 score of the slip detection algorithm for each object.

Object	Initial Closure (%)	Accuracy (%)	Precision (%)	Recall (%)	F1 score (%)
Large Cylinder	20	65	71	50	59
	25	65	91	33	49
	30	48	45	17	23
	Overall	**59**	**70**	**33**	**45**
Medium Cylinder	20	60	69	37	48
	25	77	90	60	72
	30	70	75	60	67
	Overall	**69**	**78**	**52**	**63**
Small Cylinder	25	82	76	93	84
	30	73	66	97	78
	Overall	**78**	**70**	**95**	**81**
All Cylinders	**Overall**	**68**	**73**	**56**	**63**
Large Ball	20	55	56	47	51
	25	68	72	60	65
	30	62	65	50	57
	Overall	**62**	**64**	**52**	**58**
Small Ball	25	57	58	47	52
	30	63	68	50	58
	Overall	**60**	**63**	**48**	**55**
All Balls	**Overall**	**61**	**64**	**51**	**57**
Overall		**65**	**69**	**54**	**61**

slip, for each of the slip intervals. The obtained results had a mean value of 0.055 ± 0.074 s and a median of 0.016 s.

5.2 Controller Response

An illustrative example of the system's response in the absence of any low-level controller is presented in Figure 5.2. Similarly to the examples of the system response presented next, the plotted trial corresponds to the small cylinder with an initial closure of 30%. As can be visualised, the disturbances caused by the robotic arm are not compensated for due to the absence of slip control, and the hand closure remains constant throughout the entire trial. The initial peak in acceleration can be attributed to the hand's initial closing. This initial peak has been truncated to facilitate a clearer visualisation of the subsequent signal.

The system's response using the bandpass controller can be visualised in Figure 5.3. Similarly to before, the initial acceleration peak present without any controller is also present in this sample. However, in this case, the initial instability results in a slip signal that leads to an increase in the closure level. This increase continues until a stable grasp without slip is detected. Following this, the closure level slowly decreases as the controller tries to reach the target force initially set when the bandpass controller is activated. Once the robotic arm interacts with the object, creating

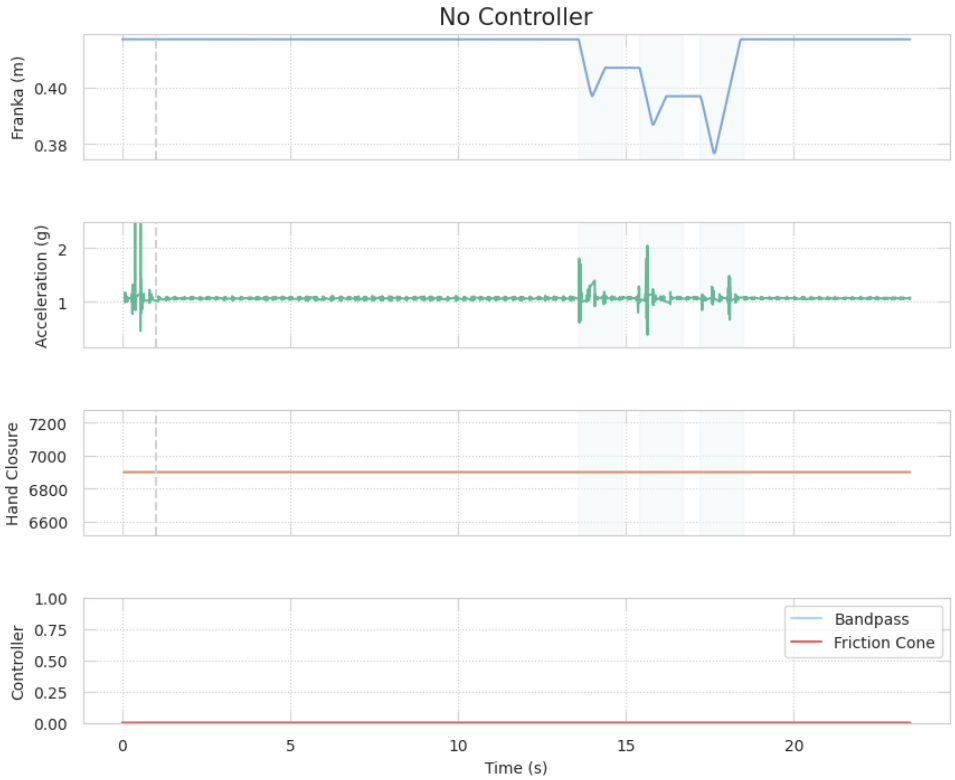


Figure 5.2: System response without any low-level controller. Although there is significant acceleration, the hand aperture remains constant.

disturbances, slip is detected. This results once more in the increase in closure level. Notably, the third slip event results in higher acceleration, which is compensated for by a bigger and steeper increase in hand closure.

The response of the friction cone controller is exemplified in Figure 5.4. The initial closing of the hand results not only in a peak in acceleration, as before, but in the friction coefficient as well. Then, there is a slight decrease in closure level until slip is induced. With this controller, the disturbances created by the robotic arm translate to an increase in the friction coefficient. To try and compensate for the disturbances, the closure level of the hand increases proportionally to the increase in the friction coefficient. Because the value of the friction coefficient after the disturbances have finished is higher than the set value, the hand closure continues to increase.

Finally, the response of the combined controller is shown in Figure 5.5. Here, the initial peaks in acceleration and friction coefficient are present and have also been truncated for visualisation purposes. After the bandpass controller is activated, slip is immediately detected, resulting in a fast increase in closure level. Although at this stage, the friction cone controller is not active and thus the system response does not depend on this parameter, it can be seen that the friction coefficient decreases. After the initial increase and once slip was not detected for 1 s, the bandpass controller is deactivated and the friction cone is activated. Once the robotic arm starts moving, the friction coefficient increases and the hand closure increases further in response.

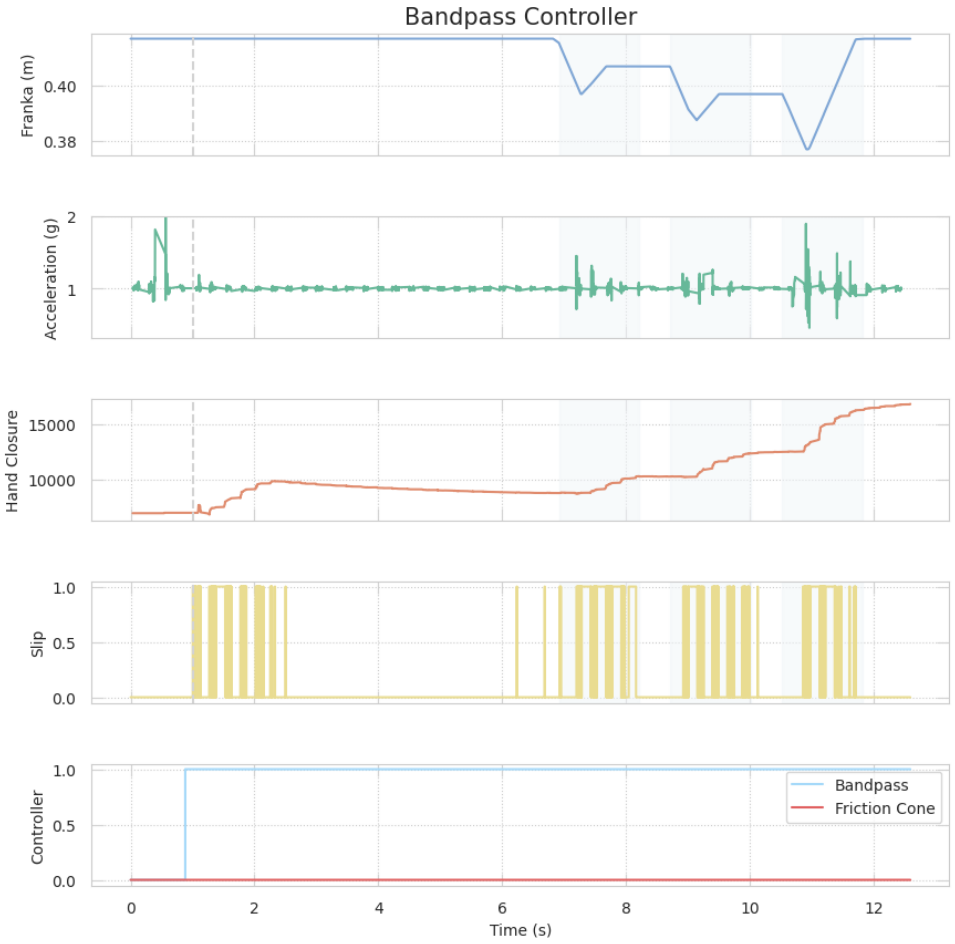


Figure 5.3: System response with the bandpass controller. The disturbance is detected by the algorithm resulting in an increase in closure level while slip occurs.

To evaluate the performance of the different controllers, the four selected metrics were calculated. The overall results, grouping the objects and initial closure levels together, are presented in Figure 5.6 and Table 5.2.

Table 5.2: Mean and standard deviation (Std) of the acceleration and force for each controller.

	Average Acceleration (g)		Maximum Acceleration (g)		Average Force (N)		Maximum Force (N)	
	Mean	Std	Mean	Std	Mean	Std	Mean	Std
No Control	1.042	0.060	2.004	1.708	2.8	4.0	3.2	4.2
Friction Cone	1.016	0.054	1.797	1.215	3.3	6.0	3.8	6.5
Combined	1.036	0.081	1.777	1.307	5.9	9.3	6.4	9.8
Bandpass	1.014	0.037	1.490	0.876	7.9	13.2	8.5	13.8

The sample populations do not have normal distributions and thus do not adhere to the assumptions to implement the ANOVA test. Due to this, the Friedman test was implemented. For the controllers, significant differences were assumed based on the right-tail chi-square critical values (p-value < 0.025 and $Q > 9.348$). If there was a significant difference, the Wilcoxon test was implemented. The Friedman test results are summarised in Table 5.3.

Table 5.3: Results of the Friedman test using the controllers, the objects and the initial closure level as the within-subject factor. Q is the Friedman chi-square statistic.

	Average Force		Maximum Force		Average Acceleration		Maximum Acceleration	
	Q	p-value	Q	p-value	Q	p-value	Q	p-value
Controllers	20.815	<0.001	18.692	<0.001	9.831	0.020	11.215	0.011
Objects	23.400	<0.001	25.700	<0.001	1.000	0.910	11.700	0.020
Closure	14.000	0.001	14.000	0.001	3.167	0.205	0.500	0.779

Table 5.4: Results of the pairwise comparison using the Wilcoxon test for each metric between controllers and between objects. S., M. and L. respectively represent small, medium and large, while Cyl. is an abbreviation for cylinder. NC, CC, FC and BP are the respective abbreviations of no controller, combined controller, friction cone and bandpass.

Controllers					**Objects**						**Initial Closure**			
Average Force														
	BP	**CC**	**FC**	**NC**		**L. Ball**	**L. Cyl.**	**M. Cyl.**	**S. Ball**	**S. Cyl.**		**20%**	**25%**	**30%**
BP	1.000	0.376	0.002	0.008	**L. Ball**	1.000	0.016	0.312	0.641	0.008	**20%**	1	0.043	0.009
CC		1.000	< 0.001	0.005	**L. Cyl.**		1.000	0.008	0.008	0.008	**25%**		1	0.002
FC			1.000	0.839	**M. Cyl.**			1.000	0.055	0.016	**30%**			1
NC				1.000	**S. Ball**				1.000	0.008				
					S. Cyl.					1.000				
Maximum Force														
BP	1.000	0.34	0.003	0.008	**L. Ball**	1.000	0.016	0.312	0.461	0.008	**20%**	1	0.052	0.009
CC		1.000	< 0.001	0.008	**L. Cyl.**		1.000	0.008	0.008	0.008	**25%**		1	0.003
FC			1.000	0.787	**M. Cyl.**			1.000	0.016	0.008	**30%**			1
NC				1.000	**S. Ball**				1.000	0.008				
					S. Cyl.					1.000				
Average Acceleration														
BP	1.000	0.013	0.892	0.057										
CC		1.000	0.057	0.635										
FC			1.000	0.013										
NC				1.000										
Maximum Acceleration														
BP	1.000	0.146	0.010	0.001	**L. Ball**	1.000	0.008	0.008	0.195	0.148				
CC		1.000	0.946	0.080	**L. Cyl.**		1.000	0.742	0.312	0.250				
FC			1.000	0.057	**M. Cyl.**			1.000	0.055	0.250				
NC				1.000	**S. Ball**				1.000	0.844				
					S. Cyl.					1.000				

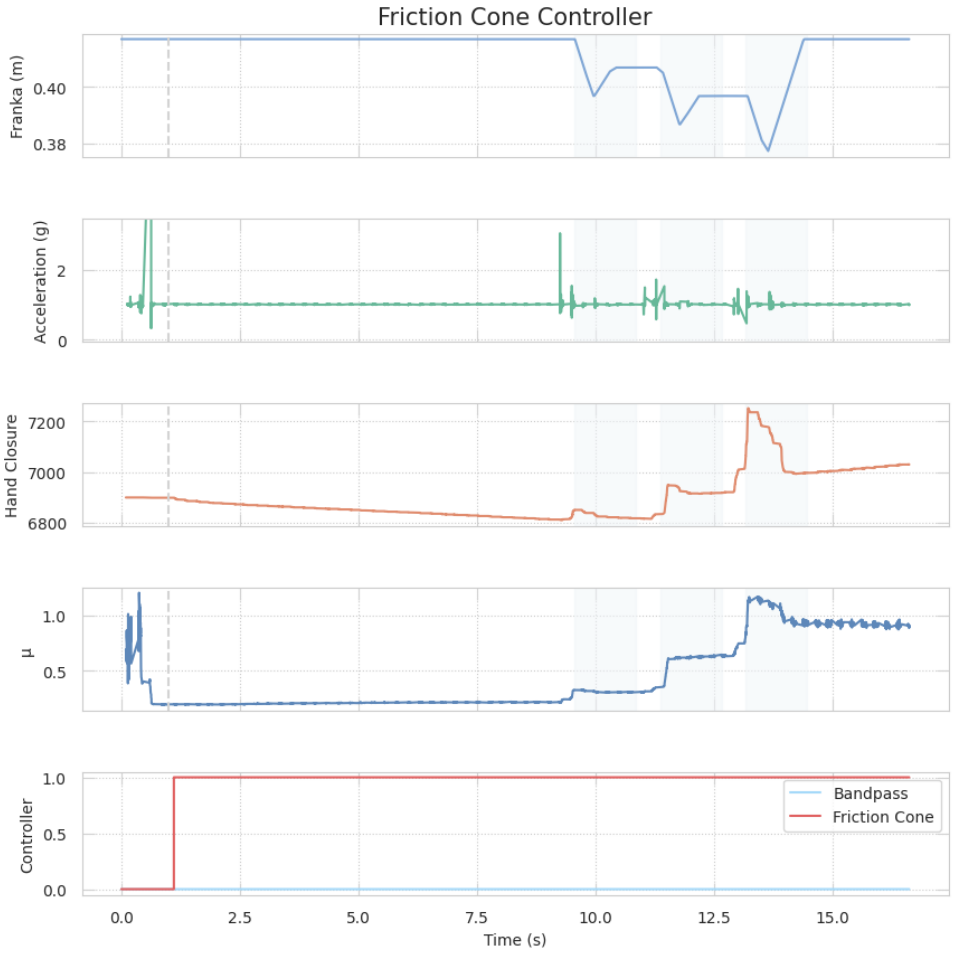


Figure 5.4: System response with the friction cone controller. The disturbances result in an increase in the friction coefficient (μ) resulting in an increase in the closure level.

The Friedman test implies that there is a significant difference between the distributions for the four metrics. The pairwise analysis, presented in Table 5.4, shows that, for both force metrics, the differences are significant between all controllers with the exception of the bandpass-combined controller and the no control-friction cone pairings. For the average acceleration, results imply that there is only significant difference between the bandpass-combined controller and the no control-friction cone pairings. For the maximum acceleration, only the bandpass-friction cone and bandpass-no control pairings showed statistical differences.

Considering the median average force, the no controller and the friction cone obtained similar results, both with a value of 1.5 N. However, by looking at Table 5.2 it is possible to distinguish between the two controllers, with the friction cone resulting in 18% more average grip force than the no controller. The combined controller, with a median value of 2.6 N, resulted in higher grip force than the previous two controllers. The bandpass controller applied the highest average force, with a median value of 3.0 N. The maximum force obtained very similar results to the average force, with median values of 1.8 N for the no controller and friction cone, 2.8 N for the combined controller and 3.3 N for the bandpass. The mean values were 3.2 N, 3.8 N, 6.4 N and 8.5 N,

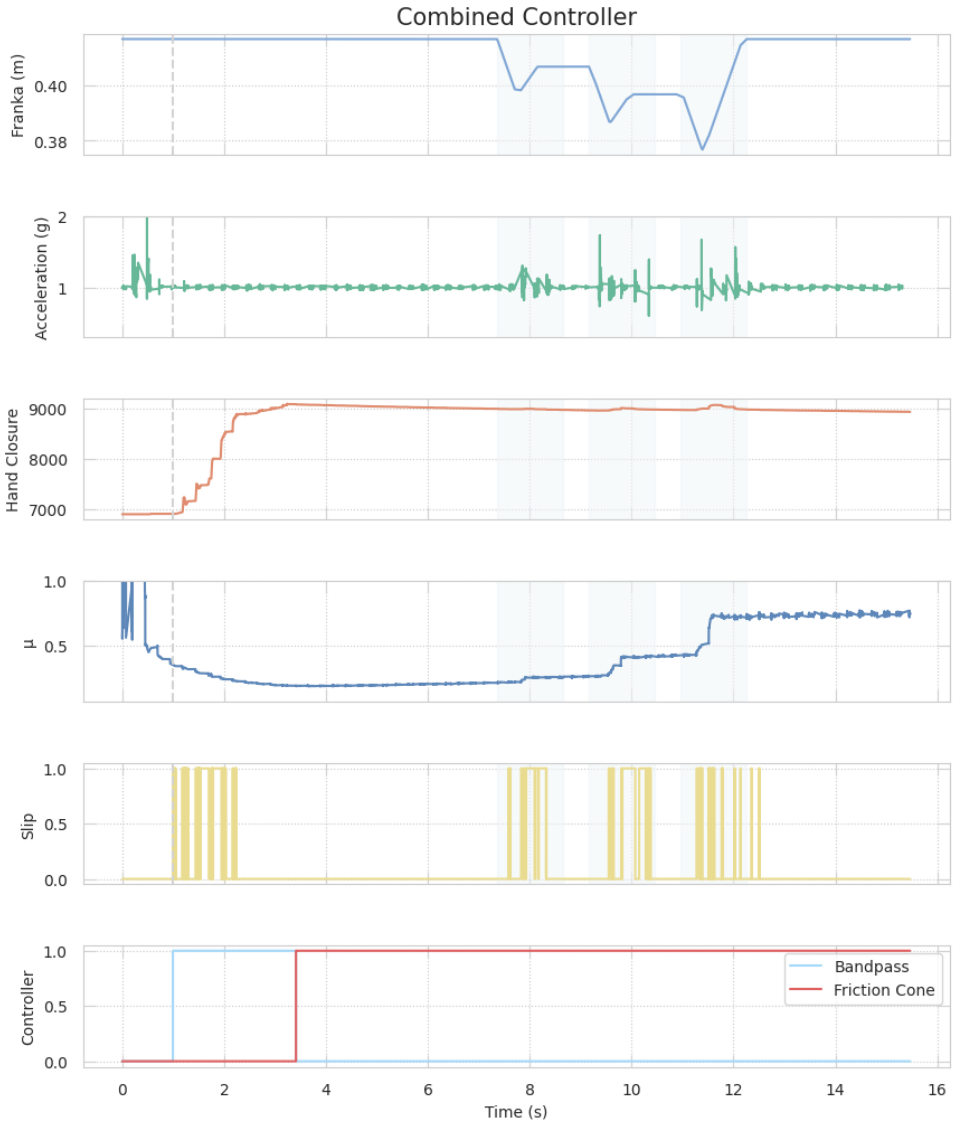


Figure 5.5: System response with the combined controller. Slip is initially detected using bandpass filtering, resulting in a fast increase in hand closure. The controller then switches to the friction cone where the increase in the friction coefficient (μ) results in a further increase of the closure level.

respectively.

The overall median values of the average acceleration were 1.033 g for the no controller, 1.010 g for the friction cone, 1.028 g for the combined controller and 1.018 g for the bandpass controller. The differences in the maximum acceleration are more significant, with the bandpass resulting in the smallest value (mean of 1.490 g), while the acceleration was higher for the no controller (mean of 2.004 g). The combined controller and the friction cone performed similarly in terms of maximum acceleration, with means of 1.777 g and 1.797 g respectively. Likewise, the highest maximum acceleration was reported with the no controller (13.856 g), which is followed by the friction cone (11.607 g), the combined controller (11.323 g) and the bandpass (10.992 g).

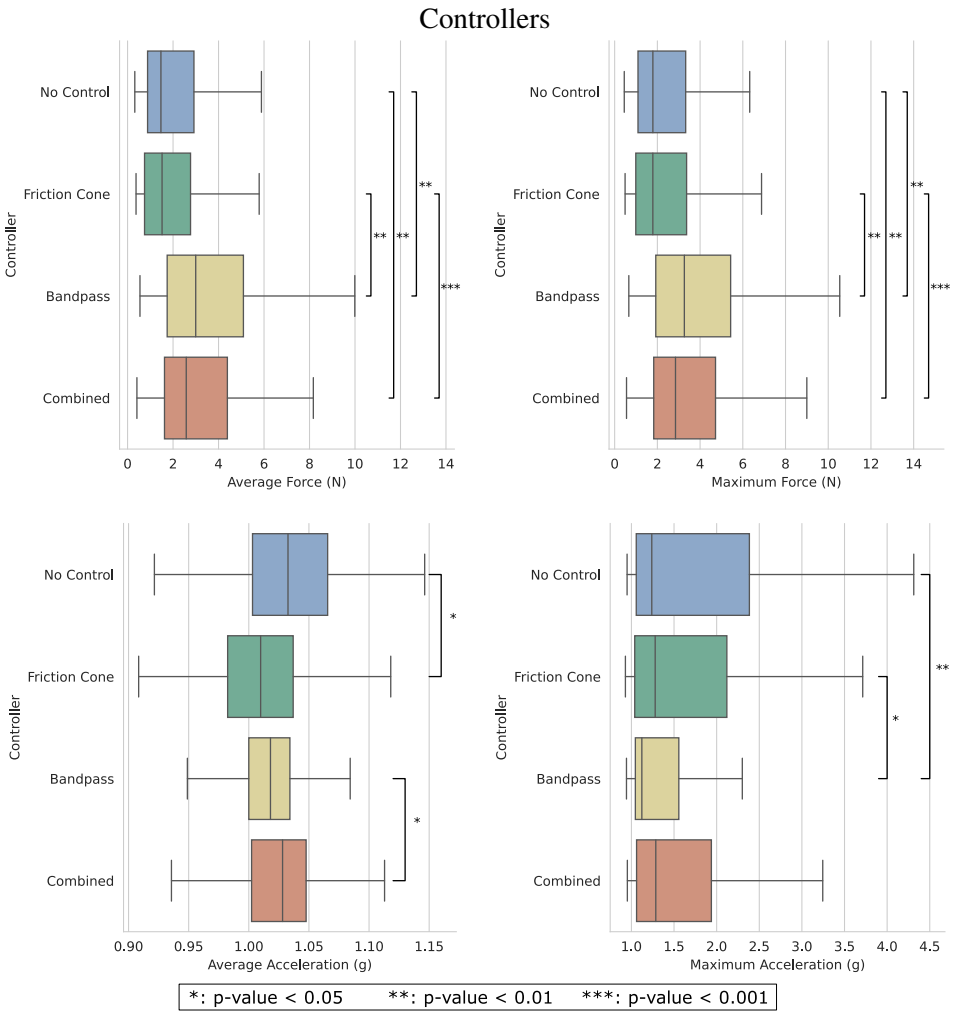


Figure 5.6: Force and acceleration for each controller across all objects and initial closure levels. Outliers were removed for visualisation purposes.

Although some trends can be extracted from the overall results, the grouping of the distinct objects does not allow for an analysis of how the object's properties affect the controllers' performance, shown in Figure 5.7. As with the controllers, it is possible to extract the object-dependency of the metrics from the Friedman test based on the right-tail chi-square critical values (p-value < 0.025 and $Q > 11.143$). Results imply that the metrics, with the exception of the average acceleration, present distinct distributions based on the object. The post-hoc analysis in Table 5.4 suggests that, for both force metrics there are significant differences between the objects, with the small cylinder being distinct from all others. For the maximum acceleration, the Wilcoxon test suggests there are significant differences between the large ball and large cylinder, and the large ball and medium cylinder.

The distinct response between the objects can be seen in Figures 5.8 and 5.9. In the case of the large cylinder, large ball and small cylinder, the average and maximum force follow the previously mentioned trend with increasing force for the no controller, friction cone, combined controller and bandpass. Similar results were obtained with the medium cylinder, with the exception of the

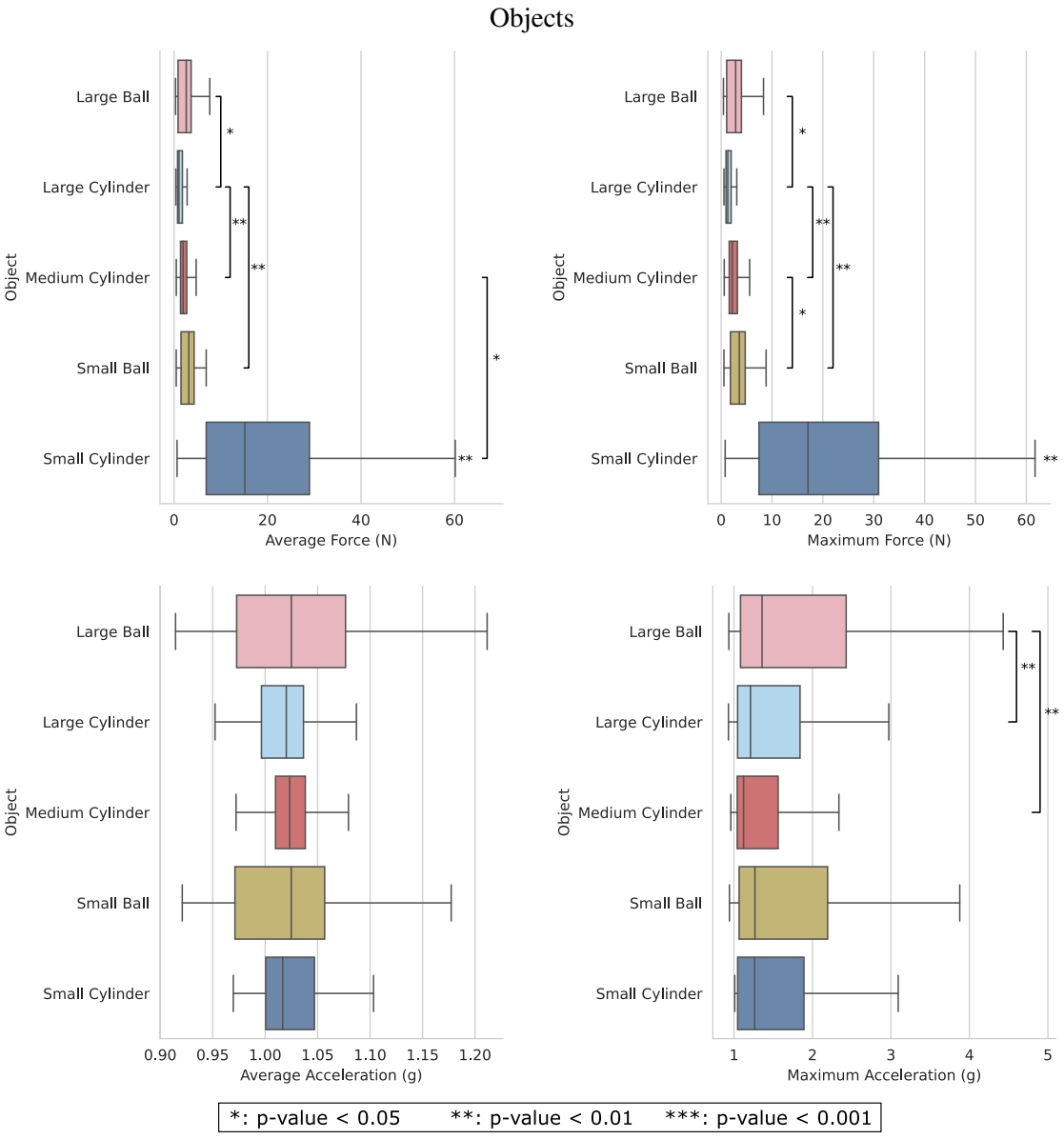


Figure 5.7: Force and acceleration for each object across all initial closure levels and controllers are displayed. Outliers as well as the results for the small cylinder are omitted for visualisation purposes.

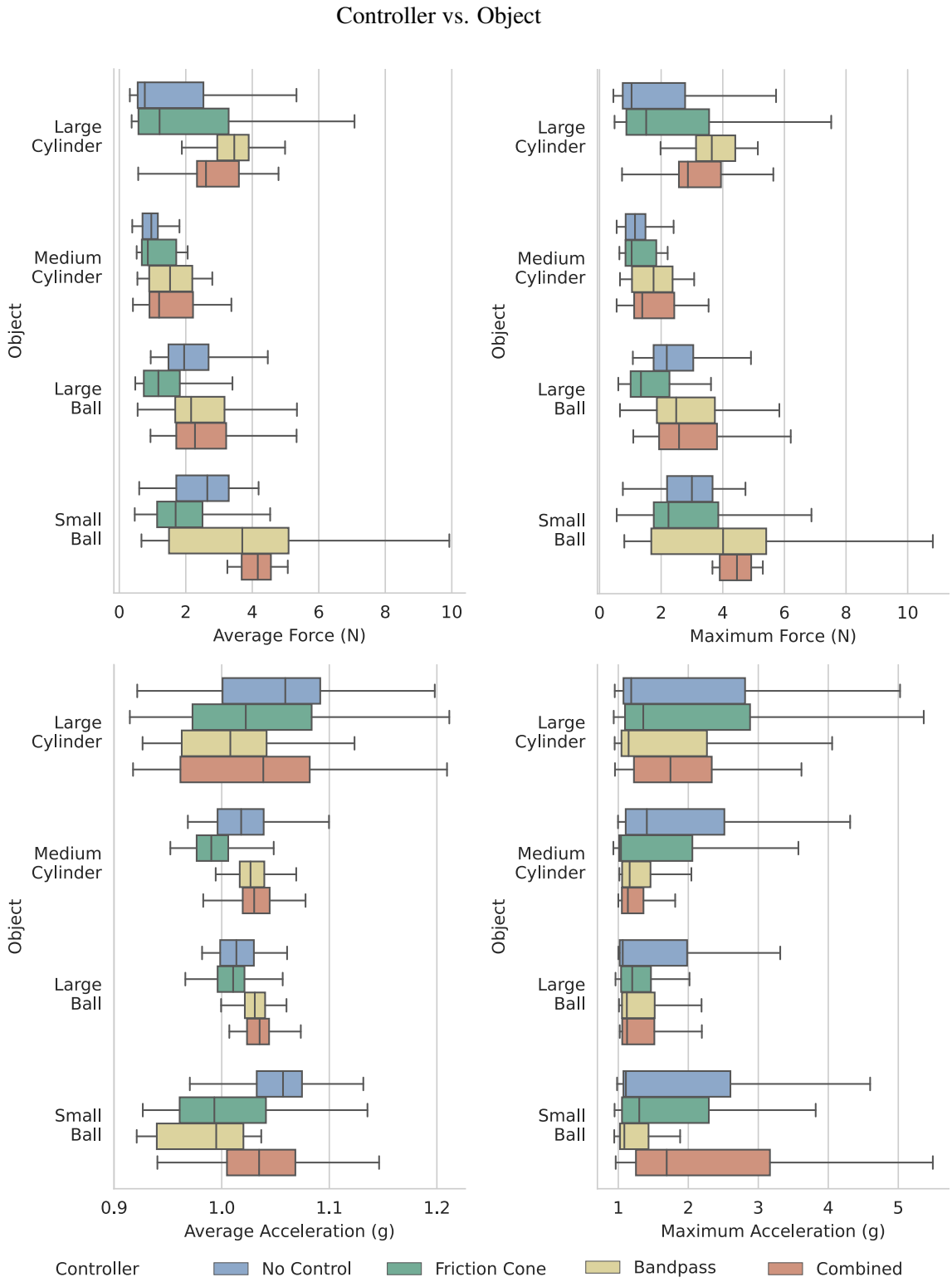


Figure 5.8: Force and acceleration for each controller across all initial closure levels are displayed for each object. Outliers as well as the results for the small cylinder are omitted for visualisation purposes.

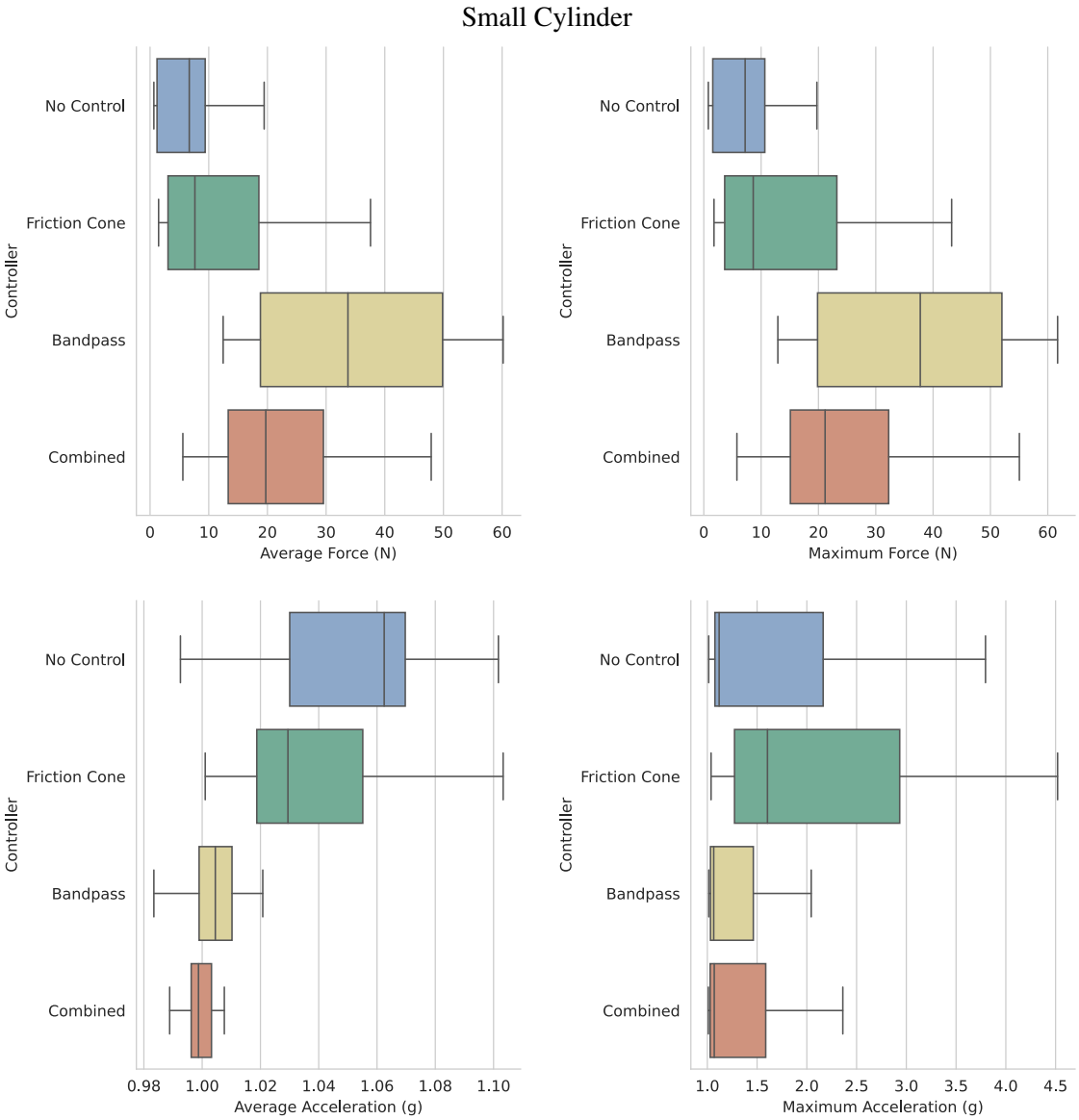


Figure 5.9: Force and acceleration for each controller across all initial closure levels for the small cylinder. Outliers are omitted for visualisation purposes.

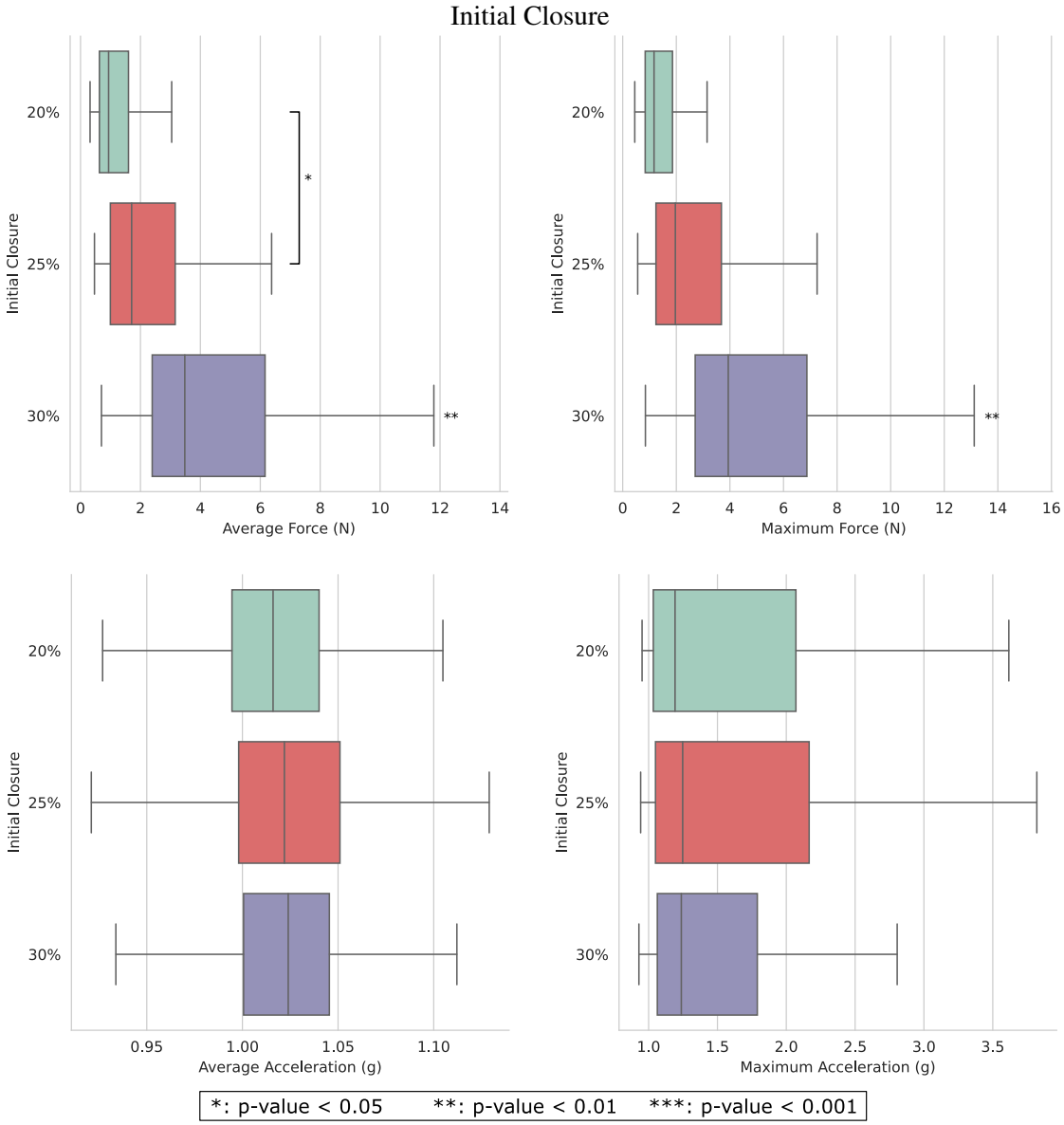


Figure 5.10: Force and acceleration for each initial closure across all objects and controllers are displayed. Outliers are omitted for visualisation purposes.

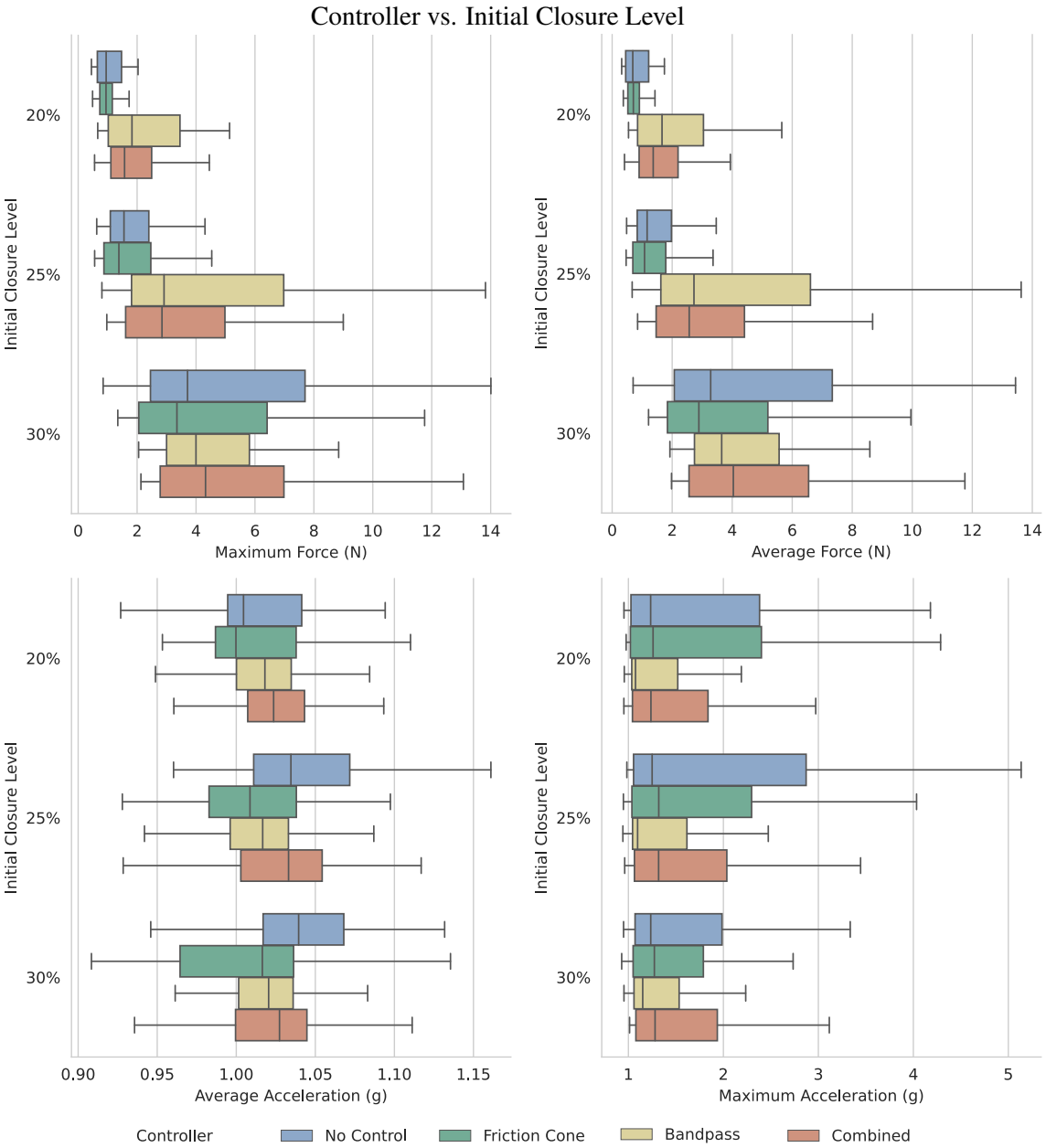


Figure 5.11: Force and acceleration for each controller across all objects are displayed for each initial closure level. Outliers are omitted for visualisation purposes.

friction cone, which resulted in lower applied force than all the other controllers. With the small ball, results also diverged from the overall trend. The friction cone once again resulted in the lowest force, followed by the no controller, the bandpass and the combined controller.

As previously mentioned, the average acceleration does not present significant differences between objects and, consequently, it is harder to discern any notable trends. In contrast, the maximum acceleration presents more distinguishable results. Using the large cylinder, the combined controller had the best performance (mean of 1.382 g), followed by the bandpass (1.509 g), the friction cone (1.715 g) and the no controller (2.021 g). The mean value of the no controller was the highest for all objects except the small ball, where the combined controller had the worst performance. For the large and small balls, the mean of the maximum acceleration was the lowest for the bandpass. For the medium cylinder, similarly to the large cylinder, the mean of the maximum acceleration was lowest for the combined controller. Using the small cylinder, the bandpass achieved the lowest mean of the maximum acceleration.

Another independent variable that must be considered is the influence of the initial closing level of the hand, shown in Figure 5.10. The Friedman test suggest this variable does not result in significant differences in the average and maximum acceleration. The pairwise comparison implies there are significant differences between all pairs for both force metrics with the exception of the maximum force between the 20% and 25% initial closure level.

As can be seen from Figure 5.11, the average and maximum acceleration have similar distributions for each object across the three initial closure levels with no significant statistical difference. The distributions of both force metrics for the three closure levels have significant differences. For the two smaller initial closure levels, a similar trend is visible, with increasing average and maximum force for the friction cone, no controller, combined controller and the highest mean values for the bandpass. For the 30% closure level, the average and maximum force are lowest for the no controller (respective means of 5.2 N and 5.8 N), followed by the friction cone (6.4 N and 7.1 N), the combined controller (9.6 N and 10.3 N) and the bandpass (12.5 N and 13.2 N).

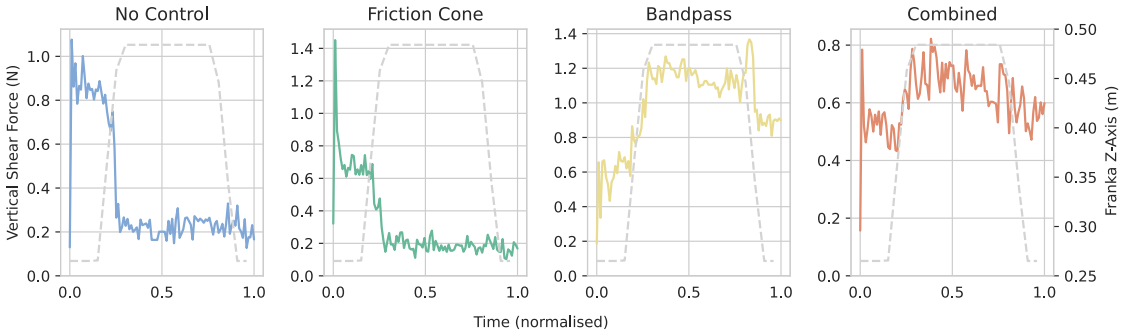


Figure 5.12: Shear force (vertical) of a lifting trial for each of the controllers. The trajectory of the hand in the vertical axis is plotted in a dashed line.

5.3 Human Response

The shear force resulting from the human comparison trials is presented in Figure 5.12. Both the no controller and the friction cone controller failed to complete the task, with the object being dropped when the tendon attached to the weight was fully extended. This can be visualised by the sudden drop in shear force in both plots as the hand was lifted. The bandpass and combined controller were both successful at lifting the object by adapting the grip force. This is visible in the increase in shear force as it is lifted.

The combined controller resulted in an average force of 1.0 ± 0.2 N, while the bandpass resulted in an average force of 1.4 ± 0.2 N.

Chapter 6

Discussion

6.1 Slip Detection

Based on the distinct responses of each bandpass filter, the strategy of monitoring the frequencies in parallel proved successful in detecting slip throughout its occurrence. Following a similar reasoning, the low thresholds also allowed for continuous slip detection. This is important as it will allow for grip correction until slip is stopped. In contrast, if the thresholds were higher, while slip could still be detected, the information regarding its duration would be lost.

It should be noted that the amplitude of the signal is much higher in the beginning stages of grasp when compared to the induced slip events. While this phase of grasp is associated with instability, and thus it is possible that slip is occurring, it is also possible that the signal is affected by some residual movement of the setup. During the experimental phase of this work, it became apparent that the configuration of the setup led to the transmission of noticeable vibrations throughout the setup due to both the quick closure of the hand in the initial closing and the motion of the robotic arm. For example, in Figure 5.3, the detection of slip, before the first slip interval, happens while the robotic arm is moving to its initial position. This is in agreement with the results reported in [29], where the bandpass filtering strategy was very sensitive to external disturbances. As the amplitude of the initial and induced slip signals is so distinct, one possible strategy to mitigate this effect would be to introduce an upper threshold as implemented in [74].

However, the choice of frequencies to monitor and their respective threshold should consider that the detection quality is dependent on the object's shape and size. As presented in the results, the detection is not as accurate for the balls as it is for the cylinders. This can be attributed to the fact that only a maximum of three or four of the seven sensors, depending on the diameter of the ball, actually established contact with the object. This leads to the possibility that the sensors in the mid-palm, little and ring finger affected the overall robustness as they were only in contact with each other and other unsensorised parts of the hand instead of the object. A simple solution to this problem would be to use position encoders in the finger joints to identify which fingers are fully closed and consequently not involved in the grasp. This way, information not directly relevant to the grasp could be discarded.



(a) (b) (c)

Figure 6.1: Examples of insufficient contact between the object and sensors for the large ball (a) and medium cylinder (b). The small cylinder's geometry allowed for better contact with the sensors (c).

Within the cylinders, the detection was more accurate for the smaller diameters. This can be associated with the somewhat bulky geometry of the sensors. For this type of sensor with low spatial resolution, the best signal is obtained when the contact with the object happens directly above the centre of the embedded magnet, with a direction perpendicular to the sensor's surface. However, as it is not possible to control precisely how the hand closes, good contact was not always achieved. This is exemplified in Figure 6.1, where it is visible that the sensors in the thumb and middle finger do not establish contact with the large ball. Although there is more contact between the sensors and the medium cylinder, this contact does not happen in the best position or direction.

In contrast, better detection was obtained using the small cylinder whose geometry allowed for better contact points and contact direction with the object. For this object, 95% of slip events were detected. This was the only object for which recall was superior to precision. The balance between these two metrics should be tuned based on the importance given to avoiding slip or avoiding excessive force. However, as can be seen from comparing the recall between the different cylinders, improving the contact with the sensors would significantly improve the overall slip detection. Regardless of the object, contact would be improved when directly applied to prostheses. The sensors would have to be directly embedded in the fingers instead of extruding from the finger's surface, thus allowing for better contact, especially with higher-diameter objects.

The grasped object is not the only variable that affects the slip detection quality. The initial closure level also significantly impacts the algorithm's performance. Both insufficient and excessive closure of the hand seem to worsen the detection quality.

Analysing the results obtained for the reaction time, the high value of the standard deviation in comparison with the mean seems to indicate that the strategy of including only the small cylinders in this calculation was not completely efficient in removing the effect of outliers caused by possible false negative classifications. Due to this, the median is a more representative value of the approximate reaction time of the detection.

6.2 Controller Comparison

It should be noted that, ideally, slip would be quantified based on displacement. However, acceleration was used instead due to the difficulty in directly measuring displacement. While theoretically, acceleration can be used to calculate displacement, the noise associated with IMU measurements makes this unfeasible.

The sensitivity of the detection to the noise directly impacts the response of the bandpass and combined controllers. Because of this, the force applied by these two controllers is superior to the one applied by the friction cone controller. The excess force could be somewhat diminished by further tuning of the controllers' parameters, especially the slip gain. It should be noted that these were determined using the SoftHand Research and, due to time limitations, were not tuned to the SoftHand Research 2 used during the experimental phase and which is capable of a superior payload.

In general, the combined controller performed as expected, resulting in a decrease in force when compared to the bandpass filter. By analysing the maximum acceleration, although the average result for the combined controller and friction cone is very similar, the combined controller was better at avoiding extremely high values.

The results obtained using the small cylinder were more demonstrative of the concept behind the combined controller. For this object, both the average and maximum force applied by the combined controller were much lower than the ones resulting from the bandpass controller. As expected, the friction cone and no controller resulted in even lower forces. However, these two controllers resulted in much higher accelerations than the combined and bandpass controllers, which is correlated to higher displacement caused by slip. The acceleration obtained by the combined controller was similar to the one obtained by the bandpass. Considering both force and acceleration, it can be stated that, using the small cylinder, the combined controller achieved a balance between the applied force and the amount of slip of the object.

The overall better performance of the combined controller when using the small cylinder can be partially attributed to the good performance of the slip detection for this object. The rationale behind the performance of the detection algorithm discussed in Chapter 6.1 can be similarly extended to the separate control states. Establishing proper contact between the sensors and objects is essential to obtain accurate force measurements, which is a fundamental requirement for the PI force and friction controllers.

Although the slip detection's accuracy was dependent on the initial closure level, the overall results seem to indicate that, with the exception of the highest closure level, the combined and bandpass controllers were able to significantly reduce the maximum acceleration when compared to the no controller and friction cone. The difference between the four controllers is not as significant for the highest closure level. This suggests that 30% was a sufficient closure level to establish a secure grip of all objects, and thus, the differences between the controllers' action was not as significant. This is also visible in the distribution of the average and maximum force for this closure condition.

This points to the idea that the combined controller could be applied to a strategy where the user is only responsible for initiating the grasp. Then, the hand would close until a predetermined minimum grasp force is reached. After this, the combined controller would be able to detect if there is a need to increment the force, and then keep the stability in reaction to other disturbances.

An illustration of this was already obtained in the human comparison trials. In this case, using the smallest initial closure level, the combined and bandpass controllers were both able to adapt and lift the object entirely. In contrast, the response of the friction cone was not enough to succeed, with the object being dropped as soon as the weight increased. This can be attributed to an incorrect estimation of the model of friction, demonstrating that assuming stability as soon as the initial closing of the hand stops does not provide a sufficient model. While both the combined and bandpass controllers were successful, the combined controller again resulted in a smaller grip force.

6.3 Comparison with Human Grasping

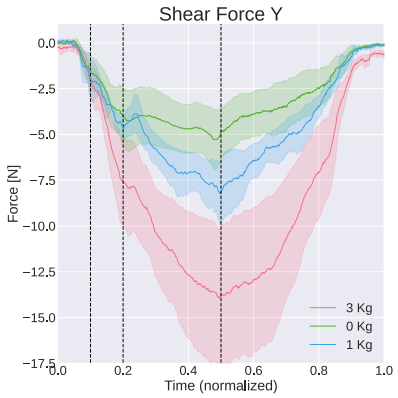


Figure 6.2: Evolution of shear force in human hands when lifting three objects of distinct weight. Taken from [67].

It is possible to compare the evolution of the shear force throughout the lifting of the weighted cylinder with the one obtained in [67], which is presented in Figure 6.2. In the curves obtained for the controller's response, it is possible to see the same steps as in the human response. First, the object is grasped, corresponding to the initial peak in force. Then, as the object is lifted, the shear force increases further. This force is approximately sustained until the object is placed back on the table. The similarity between the curves seems to indicate that both controllers were successful at mimicking the biological strategy.

Based on human physiology, [75] proposes some basic criteria to which biomimetic robotic tactile control should adhere to. Firstly, the control system should work with a maximum latency of 70 ms. It was not possible to determine the exact response time of the system from the creation of the disturbance until the start of its correction. However, the bandpass slip detection was performed in around 16 ms. The only delay purposely introduced in the system is associated with the

use of a window of five samples for the calculation of the friction coefficient, which results in a delay of approximately 25 ms. This suggests that the combined controller fulfils this requirement.

A further requirement concerns the minimising of the automatic force increase to only slightly above the force required to avoid slip. The combined controller proved successful in decreasing the grasping force when compared to the state-of-the-art bandpass controller. However, additional tuning of the slip thresholds and slip gain can further decrease this value.

Although the low-level controller should be able to autonomously correct grasp instability, it is suggested that the user's volition should overpower this. In the implemented controller, EMG input is continuously checked for. In case a closing or opening signal is detected, the low-level controller is stopped, giving the user full autonomy to, for example, squeeze or release the grasped object.

Chapter 7

Conclusion

In this work, a novel approach for a hierarchical controller for hand prostheses was developed. The proposed algorithm took inspiration from the physiology of human hands by combining the traditional EMG high-level controller with two low-level state-of-the-art solutions. This strategy divides the autonomy between the user and the prostheses in an attempt to reduce both the mental and physical effort of the user.

This strategy was applied to a highly underactuated hand, so the high-level controller was implemented similarly to current commercial solutions. The low-level controller was designed to correct instability during grasping. The proposed controller attempts to combine the robustness of the friction cone model with the easiness of implementation of the bandpass detection. The bandpass detection was employed in the initial stages of grasping until the grasp could be considered stable. After this, the friction model is obtained, and the controller moves into the friction cone state. The stability is then kept by keeping the ratio between the shear and normal forces. The strategy was implemented using custom-made 3D force sensors in the fingertips and palm.

To validate the combined controller, a set of experiments were performed to compare its performance with the performance of the two individual approaches, as well as in comparison to a scenario where no low-level controller was employed. Each controller was tested using multiple objects and initial closure levels. For each condition, the object was grasped by the hand while slip was induced three times by a robotic arm. The response was analysed based on the applied grasping force and the object's acceleration. Results show that the new strategy can counteract slip more efficiently than the friction cone controller while applying less force than the bandpass controller.

Additional experiments were performed to assess the controller's similarity to human physiology. Based on previous work, the hand was attached to the robotic arm and ordered to grasp an object. While the object was being lifted, its weight was suddenly increased. Only the novel approach and the bandpass controller were able to successfully complete this trial.

Overall, the proposed approach successfully combined the advantages of the two state-of-the-art strategies. However, further developments described in Chapter 6 would need to be implemented to optimise the controller's performance.

7.1 Future Work

As this work presents a preliminary analysis of a novel approach to slip control of upper-limb prostheses, there are multiple possible future developments. Some of them were already discussed in Chapter 6 and pertain to the limitations of the presented work. These include improvements to the setup, for example, by embedding the sensors in the prosthetic hand and including proprioceptive sensors, and improvements to the algorithm, such as the introduction of a second threshold.

Additionally, there are multiple possibilities for further exploration of the proposed strategy. For example, the combined controller can be studied in a prosthesis with a higher actuation level. This would allow the hand to make local corrections to the grasp based on the force applied by each finger instead of increasing the overall force. Higher actuation would also be relevant in the case of rotational slip, which was not studied here, where there might be more satisfactory strategies than increasing the global grip force.

To further simplify the user's experience controlling the prosthesis, a strategy encompassing the implementation of a minimal initial grip force could be studied. This would minimise the user's effort by exploring the low-level controller's ability to achieve and maintain grasp stability.

Finally, the system presented here could be enhanced by the addition of force and slip feedback to the user. While this should not replace the low-level controller, it would improve the user's overall experience.

References

[1] P. Capsi-Morales, C. Piazza, M. G. Catalano, G. Grioli, L. Schiavon, E. Fiaschi, and A. Bicchi. Comparison between rigid and soft poly-articulated prosthetic hands in non-expert myo-electric users shows advantages of soft robotics. *Sci Rep*, 11(1):23952, 2021. URL: https://www.ncbi.nlm.nih.gov/pubmed/34907228, doi:10.1038/s41598-021-02562-y.

[2] A. Marinelli, N. Boccardo, F. Tessari, D. Di Domenico, G. Caserta, M. Canepa, G. Gini, G. Barresi, M. Laffranchi, L. De Michieli, and M. Semprini. Active upper limb prostheses: a review on current state and upcoming breakthroughs. *Progress in Biomedical Engineering*, 5(1), 2023. doi:10.1088/2516-1091/acac57.

[3] S. Raspopovic, G. Valle, and F. M. Petrini. Sensory feedback for limb prostheses in amputees. *Nat Mater*, 20(7):925–939, 2021. URL: https://www.ncbi.nlm.nih.gov/pubmed/33859381, doi:10.1038/s41563-021-00966-9.

[4] F. Cordella, A. L. Ciancio, R. Sacchetti, A. Davalli, A. G. Cutti, E. Guglielmelli, and L. Zollo. Literature review on needs of upper limb prosthesis users. *Front Neurosci*, 10:209, 2016. URL: https://www.ncbi.nlm.nih.gov/pubmed/27242413, doi:10.3389/fnins.2016.00209.

[5] M. Atzori and H. Muller. Control capabilities of myoelectric robotic prostheses by hand amputees: A scientific research and market overview. *Front Syst Neurosci*, 9:162, 2015. URL: https://www.ncbi.nlm.nih.gov/pubmed/26648850, doi:10.3389/fnsys.2015.00162.

[6] U. Wijk and I. Carlsson. Forearm amputees' views of prosthesis use and sensory feedback. *J Hand Ther*, 28(3):269–77; quiz 278, 2015. URL: https://www.ncbi.nlm.nih.gov/pubmed/25990442, doi:10.1016/j.jht.2015.01.013.

[7] A. Freivalds. *Biomechanics of the upper limbs: mechanics, modeling and musculoskeletal injuries*. CRC press, 2011.

[8] S. A. Ovadia and M. Askari. Upper extremity amputations and prosthetics. *Semin Plast Surg*, 29(1):55–61, 2015. URL: https://www.ncbi.nlm.nih.gov/pubmed/25685104, doi:10.1055/s-0035-1544171.

[9] F. Cordella, C. Gentile, L. Zollo, R. Barone, R. Sacchetti, A. Davalli, B. Siciliano, and E. Guglielmelli. A force-and-slippage control strategy for a poliarticulated prosthetic hand, 2016. doi:10.1109/icra.2016.7487533.

[10] American Society for Surgery of the Hand. *The Hand: Examination and diagnosis*. Churchill Livingstone, London, England, 1990.

[11] V. Mendez, F. Iberite, S. Shokur, and S. Micera. Current solutions and future trends for robotic prosthetic hands. *Annual Review of Control, Robotics, and Autonomous Systems*, 4(1):595–627, 2021. doi:10.1146/annurev-control-071020-104336.

[12] H. Kettenmann. *Nervous System*, In *Gray's Anatomy: The Anatomical Basis of Clinical Practice*, pages 42–68. Elsevier, 41 edition, 2016.

[13] M. A. Adams. *Functional anatomy of the musculoskeletal system*, In *Gray's Anatomy: The Anatomical Basis of Clinical Practice*, pages 81–123. Elsevier, 41 edition, 2016.

[14] E. Criswell. *Cram's introduction to surface electromyography*. Jones & Bartlett Publishers, 2 edition, 2010.

[15] C. Piazza, G. Grioli, M. G. Catalano, and A. Bicchi. A century of robotic hands. *Annual Review of Control, Robotics, and Autonomous Systems*, 2(1):1–32, 2019. doi:10.1146/annurev-control-060117-105003.

[16] D. Trivedi, C. D. Rahn, W. M. Kier, and I. D. Walker. Soft robotics: Biological inspiration, state of the art, and future research. *Applied Bionics and Biomechanics*, 5(3):99–117, 2008. doi:10.1080/11762320802557865.

[17] R. Deimel and O. Brock. A novel type of compliant and underactuated robotic hand for dexterous grasping. *The International Journal of Robotics Research*, 35(1-3):161–185, 2015. doi:10.1177/0278364915592961.

[18] M. G. Catalano, G. Grioli, E. Farnioli, A. Serio, M. Bonilla, M. Garabini, C. Piazza, M. Gabiccini, and A. Bicchi. *From Soft to Adaptive Synergies: The Pisa/IIT SoftHand*, In *Human and Robot Hands*, book section Chapter 8, pages 101–125. Springer Series on Touch and Haptic Systems. Springer, 2016. doi:10.1007/978-3-319-26706-7_8.

[19] R. S. Johansson and J. R. Flanagan. *Tactile Sensory Control of Object Manipulation in Humans*, In *The Senses: A Comprehensive Reference*, volume 6, pages 67–86. Elsevier, 2008.

[20] R. S. Johansson and G. Westling. Roles of glabrous skin receptors and sensorimotor memory in automatic control of precision grip when lifting rougher or more slippery objects. *Exp Brain Res*, 56(3):550–64, 1984. URL: https://www.ncbi.nlm.nih.gov/pubmed/6499981, doi:10.1007/BF00237997.

[21] M. Schenker, M. K. Burstedt, M. Wiberg, and R. S. Johansson. Precision grip function after hand replantation and digital nerve injury. *J Plast Reconstr Aesthet Surg*, 59(7):706–16, 2006. URL: https://www.ncbi.nlm.nih.gov/pubmed/16782566, doi:10.1016/j.bjps.2005.12.004.

[22] R. C. Miall, O. Rosenthal, K. Orstavik, J. D. Cole, and F. R. Sarlegna. Loss of haptic feedback impairs control of hand posture: a study in chronically deafferented individuals when grasping and lifting objects. *Exp Brain Res*, 237(9):2167–2184, 2019. URL: https://www.ncbi.nlm.nih.gov/pubmed/31209510, doi:10.1007/s00221-019-05583-2.

[23] J. A. Fishel. *Design and use of a biomimetic tactile microvibration sensor with human-like sensitivity and its application in texture discrimination using Bayesian exploration*. Thesis, University of Southern California, 2012.

[24] L. A. Jones and S. J. Lederman. *Human Hand Function*. Oxford University Press, 2006. URL: https://doi.org/10.1093/acprof:oso/9780195173154.001.0001, doi:10.1093/acprof:oso/9780195173154.001.0001.

[25] V. G. Macefield, C. Hager-Ross, and R. S. Johansson. Control of grip force during restraint of an object held between finger and thumb: responses of cutaneous afferents from the digits. *Exp Brain Res*, 108(1):155–71, 1996. URL: https://www.ncbi.nlm.nih.gov/pubmed/8721164, doi:10.1007/BF00242913.

[26] R. S. Johansson and G. Westling. Signals in tactile afferents from the fingers eliciting adaptive motor responses during precision grip. *Exp Brain Res*, 66(1):141–54, 1987. doi:10.1007/bf00236210.

[27] P. J. Blau. *Friction, History of Research*, In *Encyclopedia of Tribology*, pages 1384–1386. Springer US, Boston, MA, 2013. URL: https://doi.org/10.1007/978-0-387-92897-5_189, doi:10.1007/978-0-387-92897-5_189.

[28] Valentin L. Popov. *Coulomb's Law of Friction*, In *Contact Mechanics and Friction: Physical Principles and Applications*, pages 151–172. Springer Berlin Heidelberg, Berlin, Heidelberg, 2017. URL: https://doi.org/10.1007/978-3-662-53081-8_10, doi:10.1007/978-3-662-53081-8_10.

[29] J. Reinecke, A. Dietrich, F. Schmidt, and M. Chalon. Experimental comparison of slip detection strategies by tactile sensing with the biotac® on the dlr hand arm system. In *2014 IEEE International Conference on Robotics and Automation (ICRA)*, pages 2742–2748, 2014. doi:10.1109/ICRA.2014.6907252.

[30] D. Schlichthärle. *Digital Filters*. Springer, Heidelberg, Germany, 2 edition, 2011. doi:10.1007/978-3-642-14325-0.

[31] D. E. Seborg, T. F. Edgar, and D. A. Mellichamp. *Process Dynamics and Control*. John Wiley & Sons, 2 edition, 2004.

[32] R. Dorf and R. Bishop. *Modern Control Systems : Global Edition*. Pearson Deutschland, 2017.

[33] P. Geethanjali. Myoelectric control of prosthetic hands: state-of-the-art review. *Med Devices (Auckl)*, 9:247–55, 2016. URL: https://www.ncbi.nlm.nih.gov/pubmed/27555799, doi:10.2147/MDER.S91102.

[34] J. M. Hahne, M. A. Schweisfurth, M. Koppe, and D. Farina. Simultaneous control of multiple functions of bionic hand prostheses: Performance and robustness in end users. *Science Robotics*, 3(19):eaat3630, 2018. URL: https://www.science.org/doi/abs/10.1126/scirobotics.aat3630, doi:doi:10.1126/scirobotics.aat3630.

[35] D. Barsakcioglu and D. Farina. A real-time surface emg decomposition system for non-invasive human-machine interfaces, 2018. doi:10.1109/BIOCAS.2018.8584659.

[36] F. Clemente, M. D'Alonzo, M. Controzzi, B. B. Edin, and C. Cipriani. Non-invasive, temporally discrete feedback of object contact and release improves grasp control of closed-loop myoelectric transradial prostheses. *IEEE Trans Neural Syst Rehabil Eng*, 24(12):1314–1322, 2016. URL: https://www.ncbi.nlm.nih.gov/pubmed/26584497, doi:10.1109/TNSRE.2015.2500586.

[37] K. Kim and J. E. Colgate. Haptic feedback enhances grip force control of semg-controlled prosthetic hands in targeted reinnervation amputees. *IEEE Trans Neural Syst Rehabil Eng*, 20(6):798–805, 2012. URL: https://www.ncbi.nlm.nih.gov/pubmed/22855230, doi:10.1109/TNSRE.2012.2206080.

[38] E. D. Engeberg and S. G. Meek. Adaptive sliding mode control for prosthetic hands to simultaneously prevent slip and minimize deformation of grasped objects. *IEEE/ASME Transactions on Mechatronics*, 18(1):376–385, 2013. doi:10.1109/tmech.2011.2179061.

[39] P. Kyberd. Slip detection strategies for automatic grasping in prosthetic hands. *Sensors (Basel)*, 23(9), 2023. URL: https://www.ncbi.nlm.nih.gov/pubmed/37177637, doi:10.3390/s23094433.

[40] N. Thomas, G. Ung, H. Ayaz, and J. D. Brown. Neurophysiological evaluation of haptic feedback for myoelectric prostheses. *IEEE Transactions on Human-Machine Systems*, 51(3):253–264, 2021. doi:10.1109/thms.2021.3066856.

[41] N. Thomas, A. J. Miller, H. Ayaz, and J. D. Brown. Haptic shared control improves neural efficiency during myoelectric prosthesis use. *Sci Rep*, 13(1):484, 2023. URL: https://www.ncbi.nlm.nih.gov/pubmed/36627340, doi:10.1038/s41598-022-26673-2.

[42] N. Sommer and A. Billard. Multi-contact haptic exploration and grasping with tactile sensors. *Robotics and Autonomous Systems*, 85:48–61, 2016. doi:10.1016/j.robot.2016.08.007.

[43] S. Dosen, C. Cipriani, M. Kostic, M. Controzzi, M. C. Carrozza, and D. B. Popovic. Cognitive vision system for control of dexterous prosthetic hands: experimental evaluation. *J Neuroeng Rehabil*, 7:42, 2010. URL: https://www.ncbi.nlm.nih.gov/pubmed/20731834, doi:10.1186/1743-0003-7-42.

[44] C. Gentile, F. Cordella, and L. Zollo. Hierarchical human-inspired control strategies for prosthetic hands. *Sensors (Basel)*, 22(7), 2022. URL: https://www.ncbi.nlm.nih.gov/pubmed/35408135, doi:10.3390/s22072521.

[45] J. M. Nightingale and R. W. Todd. An adaptively-controlled prosthetic hand. *Engineering in Medicine*, 1(1):3–6, 1971. doi:10.1243/emed_jour_1971_001_003_02.

[46] R. D. Codd, J. M. Nightingale, and R. W. Todd. An adaptive multi-functional hand prosthesis. *J Physiol*, 232(2):55P–56P, 1973. URL: https://www.ncbi.nlm.nih.gov/pubmed/4727089.

[47] J. M. Nightingale. Microprocessor control of an artificial arm. *Journal of Microcomputer Applications*, 8(2):167–173, 1985. doi:10.1016/0745-7138(85)90015-6.

[48] P. H. Chappell and P. J. Kyberd. Prehensile control of a hand prosthesis by a microcontroller. *J Biomed Eng*, 13(5):363–9, 1991. URL: https://www.ncbi.nlm.nih.gov/pubmed/1795502, doi:10.1016/0141-5425(91)90015-y.

[49] P. J. Kyberd and P. H. Chappell. The southampton hand: an intelligent myoelectric prosthesis. *Journal of rehabilitation research and development*, 31(4):326–334, 1994.

[50] P. J. Kyberd, N. Mustapha, F. Carnegie, and P. H. Chappell. A clinical experience with a hierarchically controlled myoelectric hand prosthesis with vibro-tactile feedback. *Prosthet*

Orthot Int, 17(1):56–64, 1993. URL: https://www.ncbi.nlm.nih.gov/pubmed/8337101, doi:10.3109/03093649309164355.

[51] D. Gunji, Y. Mizoguchi, S. Teshigawara, A. Ming, A. Namiki, M. Ishikawa, and M. Shimojo. Grasping force control of multi-fingered robot hand based on slip detection using tactile sensor. In *2008 IEEE International Conference on Robotics and Automation*, pages 2605–2610, 2008. doi:10.1109/ROBOT.2008.4543605.

[52] V. Arapi, Y. Zhang, G. Averta, M. G. Catalano, D. Rus, C. D. Santina, and M. Bianchi. To grasp or not to grasp: an end-to-end deep-learning approach for predicting grasping failures in soft hands, 2020. doi:10.1109/RoboSoft48309.2020.9116041.

[53] J. W. James, N. Pestell, and N. F. Lepora. Slip detection with a biomimetic tactile sensor. *IEEE Robotics and Automation Letters*, 3(4):3340–3346, 2018. doi:10.1109/lra.2018.2852797.

[54] R. S. Dahiya, G. Metta, M. Valle, and G. Sandini. Tactile sensing—from humans to humanoids. *IEEE Transactions on Robotics*, 26(1):1–20, 2010. doi:10.1109/tro.2009.2033627.

[55] C. F. Pasluosta, H. Tims, and A. W. L. Chiu. Slippage sensory feedback and nonlinear force control system for a low-cost prosthetic hand. *American Journal of Biomedical Sciences*, pages 295–302, 2009. doi:10.5099/aj090400295.

[56] C. F. Pasluosta and A. W. Chiu. Evaluation of a neural network-based control strategy for a cost-effective externally-powered prosthesis. *Assist Technol*, 24(3):196–208, 2012. URL: https://www.ncbi.nlm.nih.gov/pubmed/23033736, doi:10.1080/10400435.2012.659796.

[57] E. D. Engeberg and S. G. Meek. Adaptive object slip prevention for prosthetic hands through proportional-derivative shear force feedback. In *2008 IEEE/RSJ International Conference on Intelligent Robots and Systems*, pages 1940–1945, 2008. doi:10.1109/IROS.2008.4651067.

[58] C. Gentile, F. Cordella, C. R. Rodrigues, and L. Zollo. Touch-and-slippage detection algorithm for prosthetic hands. *Mechatronics*, 70, 2020. doi:10.1016/j.mechatronics.2020.102402.

[59] N. Wettels, A. R. Parnandi, J. H. Moon, G. E. Loeb, and G. S. Sukhatme. Grip control using biomimetic tactile sensing systems. *IEEE/ASME Transactions on Mechatronics*, 14(6):718–723, 2009. doi:10.1109/TMECH.2009.2032686.

[60] N. Wettels, V. J. Santos, R. S. Johansson, and G. E. Loeb. Biomimetic tactile sensor array. *Advanced Robotics*, 22(8):829–849, 2008. doi:10.1163/156855308x314533.

[61] X. Song, H. Liu, K. Althoefer, T. Nanayakkara, and L. D. Seneviratne. Efficient break-away friction ratio and slip prediction based on haptic surface exploration. *IEEE Transactions on Robotics*, 30(1):203–219, 2014. doi:10.1109/tro.2013.2279630.

[62] J. Kwiatkowski, D. Cockburn, and V. Duchaine. Grasp stability assessment through the fusion of proprioception and tactile signals using convolutional neural networks. In *2017 IEEE/RSJ International Conference on Intelligent Robots and Systems (IROS)*, pages 286–292, 2017. doi:10.1109/IROS.2017.8202170.

[63] S. Funabashi, Y. Kage, H. Oka, Y. Sakamoto, and S. Sugano. Object picking using a two-fingered gripper measuring the deformation and slip detection based on a 3-axis tactile sensing, 2021. doi:10.1109/iros51168.2021.9636354.

[64] Magnetic sensing technologies: Reed switches vs. hall effect switches. URL: https://standexelectronics.com/magnetic-sensing/magnetic-sensing-technologies-reed-switches-vs-hall-effect-switches/.

[65] E. Ramsden. *Hall-effect sensors: theory and application*. Elsevier, 2011.

[66] A. Dwivedi, A. Ramakrishnan, A. Reddy, K. Patel, S. Ozel, and C. D. Onal. Design, modeling, and validation of a soft magnetic 3-d force sensor. *IEEE Sensors Journal*, 18(9):3852–3863, 2018. doi:10.1109/jsen.2018.2814839.

[67] T. S. Castañeda, J. Matos, P. Capsi-Morales, and C. Piazza. Spatial and temporal analysis of normal and shear forces during grasping, manipulation and social activities. In *2023 IEEE International Conference on Rehabilitation Robotics*, 2023. Forthcoming.

[68] Qbsofthand research user manual. URL: https://qbrobotics.com/.

[69] Franka Emika. libfranka. URL: https://frankaemika.github.io.

[70] P. Visconti, F. Gaetani, G. A. Zappatore, and P. Primiceri. Technical features and functionalities of myo armband: An overview on related literature and advanced applications of myoelectric armbands mainly focused on arm prostheses. *International Journal on Smart Sensing and Intelligent Systems*, 11(1):1–25, 2018. doi:10.21307/ijssis-2018-005.

[71] P. Walkington. Pyomyo, 2021. URL: https://github.com/PerlinWarp/pyomyo.

[72] P. Virtanen, R. Gommers, T. E. Oliphant, M. Haberland, T. Reddy, D. Cournapeau, E. Burovski, P. Peterson, W. Weckesser, J. Bright, S. J. van der Walt, M. Brett, J. Wilson, K. J. Millman, N. Mayorov, A. R. J. Nelson, E. Jones, R. Kern, E. Larson, C. J. Carey, I. Polat, Y. Feng, E. W. Moore, J. VanderPlas, D. Laxalde, J. Perktold, R. Cimrman, I. Henriksen, E. A. Quintero, C. R. Harris, A. M. Archibald, A. H. Ribeiro, F. Pedregosa, P. van Mulbregt, and Contributors SciPy. Scipy 1.0: fundamental algorithms for scientific computing in python. *Nat Methods*, 17(3):261–272, 2020. URL: https://www.ncbi.nlm.nih.gov/pubmed/32015543, doi:10.1038/s41592-019-0686-2.

[73] R. Vallat. Pingouin: statistics in python. *Journal of Open Source Software*, 3(31), 2018. doi:10.21105/joss.01026.

[74] S. Teshigawara, T. Tsutsumi, S. Shimizu, Y. Suzuki, A. G. Ming, M. Ishikawa, and M. Shimojo. Highly sensitive sensor for detection of initial slip and its application in a multi-fingered robot hand. *2011 Ieee International Conference on Robotics and Automation (Icra)*, pages 1097–1102, 2011. URL: <GotoISI>://WOS:000324383400041, doi:10.1109/ICRA.2011.5979750.

[75] A. Zangrandi, M. D'Alonzo, C. Cipriani, and G. Di Pino. Neurophysiology of slip sensation and grip reaction: insights for hand prosthesis control of slippage. *J Neurophysiol*, 126(2):477–492, 2021. URL: https://www.ncbi.nlm.nih.gov/pubmed/34232750, doi:10.1152/jn.00087.2021.